IMPROVED MEASUREMENT METHODS FOR IN-PROCESS METROLOGY
ON LARGE-SCALE COMPONENTS

by

Lucas Marcos Valdez

A dissertation submitted to the faculty of
The University of North Carolina at Charlotte
in partial fulfillment of the requirements
for the degree of Doctor of Philosophy in
Mechanical Engineering

Charlotte

2015

Approved by:

_____
Dr. John Ziegert

_____
Dr. Wesley Williams

_____
Dr. Gert Goch

_____
Dr. Jimmie Miller

_____
Dr. Faramarz Farahi

ABSTRACT

LUCAS MARCOS VALDEZ. Improved measurement methods for in-process Metrology on large-scale components. (Under the direction of DR. JOHN ZIEGERT)

Manufacturing processes have inherent errors during machining and in-process metrology is used to determine and correct for these manufacturing errors. In this research, the determination of size (diameter) and form error (surface profile) of large-scale circular features are considered. The objective of the research is to measure, simultaneously, the size and form error of a large-scale circular component through mathematically sound methods with the aid of a novel measuring instrument.

This research is motivated by the influence of current manufacturing processes and their in-process metrology methods. The current methods for the determination of component size is accomplished using mechanical instruments, such as calipers and micrometers. These mechanical indicators have the potential to produce unreliable results because the measuring methodology is tied to a two-point measuring method and is dependent upon the skill of the human operator. The method used in this research to measure the size of the component uses three measurement points and reconstructs the diameter of the component using a geometrical model.

Every machine with a spindle will experience spindle error motions, which describe the variable position and orientation of the spindle axis as a function of the rotating angle. However, with the spindle having off-axis error motions and the component not having a perfect geometry, measurement of the component form error using a single indicator will be a combination of both the components surface non-uniformity and the spindles axis error motions. In this research a multi-probe error separation method is used to accurately isolate the component form error from the spindle error motions.

This research developed a novel measuring instrument able to simultaneously measure both diameter and form error of circular features. The measuring instrument uses three pivoting arms attached to a body, in which is adaptable to a lathe's turret. The three arms are accompanied by three high-resolution angular encoder modules that produce the angular displacement of the arms, coupled with a kinematic model of the system, are used to reconstruct the diameter and form error of the large-scale circular component.

In this research, the results from the measuring instrument, show that it is capable of measuring both diameter and the form error simultaneously. The form error values produce a maximum error of $0.004\ mm$ $(0.00016")$ and the diameter values produce a maximum error of $0.022\ mm$ $(0.00087")$. These error values are determined with a comparison to a Coordinate Measuring Machine (CMM) value of form error and diameter.

Finally, an expanded uncertainty of $0.024\ mm$ $(0.00094")$ is determined for the diameter measurement process of the measuring instrument and an expanded uncertainty of $0.004\ mm$ $(0.00016")$ is determined for the form error measurement process of the measuring instrument.

ACKNOWLEDGEMENTS

TABLE OF CONTENTS

LIST OF FIGURES

LIST OF TABLES

CHAPTER 1: INTRODUCTION

1.1. Large-scale Metrology

Manufacturing is the process of making products by means of manual methods or industrial machinery. Manufacturing processes of components can range drastically, such as the initial step of forging or casting of a steel cylinder to precision grinding the inner diameter bore of the finished ball bearing, with stated tolerances of $\pm 0.0012\ mm$ ($\pm 0.000047"$). Advancements in manufacturing processes have produced exceptional products and the boundaries of these processes continue to be exceeded every day. Manufacturing is still a primary industry in today's technological society and in more recent times the demand for better precision manufactured items has increased. Thus, the metrology methods of manufacturing processes have also been making progress and being developed along the way, albeit at a slower rate.

The definition of metrology comes from the International Vocabulary of Metrology (VIM) [61]. It states, "Metrology is the science of measurement and its applications". This definition also states that metrology includes all theoretical and practical aspects of measurements, whatever the measurement uncertainty and field of application. Metrology can range from measuring the length of a gage block with a set of calipers to measuring the involute of a medium-sized spur gear with a coordinate measuring machine (CMM) to measuring a cargo ships propeller with laser trackers [52]. FIGURE 1 shows a typical large-scale metrology application of measuring a wind turbine blade with a laser tracker.

FIGURE 1: Large-scale metrology application (source: M7tek.com)

The scale of the component to be measured has a direct influence on what system(s) need to be used for making measurements. The larger the component of interest, the more restrictive the system that can be used to take measurements. Another issue with component scale increase, is how precise and accurate the measurements must be and what is the stated uncertainty within the measurement. These issues are of major concern for manufacturing processes because the component will more than likely be a component of an assembly and assemblies inherit all errors in each manufactured component.

In most manufacturing processes, especially of large-scale components, the metrology is done with in-process measurements. As the component is being machined, the dimensions and form (shape) of the features being created must be checked for compliance with stated tolerances. For very large components, it is impractical to dismount them from the machine tool and measure them with, say with a gantry type CMM. This would be expensive for both production time and money. Thus in-process measurement tools are a necessity. Standard practice for this type of in-process measurements is to use simple mechanical measuring technologies, which can be traced back to early days of manufacturing. FIGURE 2 shows typical in-process measurement equipment.

FIGURE 2: Large micrometer and dial indicator (source: micrometer – Fowler Precision and dial indicator – Mitutoyo)

The large-micrometer can be used for measuring the diameter of a circular component, however, one drawback is that multiple micrometers are needed to span different size diameters. A bigger issue with this measurement is that a micrometer is a two-point measuring method, a distance measurement, and thus will not pick-up odd lobing spatial frequencies in the machined component surface profile, if present. It takes a minimum of three, non-collinear, points to fully define a circle (diameter).

The component surface profile, or form error, is measured with a dial indicator. However, as a single-point measurement system, measuring a turned component has the potential to produce one-for-one errors [33] since any error motions of the spindle are included in the measurement. Furthermore, since the form errors of the component are not synchronous with the spindle motion errors, the placement of the indicator will cause the results to vary. As an example, if an indicator replaces the tool on the lathe, the profile the indicator traces will be the same path the tool point made, if the spindle errors are zero, on the component, and therefore should show essentially zero reading.

With an assortment of large-scale manufactured products, the metrology methods are not just restricted to hand-instruments and indicators. The advancements of measuring technologies for large-scale products have been on the rise. The laser tracker was first developed by Lau, Hocken and Haight in 1986 and was motivated by the need for high-accuracy measurements of positioning errors of robots [39]. Laser trackers have advanced so greatly that the market now extends from robotics to aerospace, automotive and shipbuilding industries. Another development for large-scale metrology purposes is photogrammetry. Photogrammetry is a metrology method in which the shape, size and position of objects are determined from measurements of two-dimensional images [52]. Photogrammetry is often associated with the production of topographical maps from aerial and satellite images.

The laser tracker and photogrammetry methods are major advancements in large-scale metrology and have been beneficial for their intended purpose. The in-process measurements on machine tools, more specifically lathe operations, have been lagging behind, for large-scale components. The manual methods mentioned earlier were acceptable when first developed and implemented, however with advancements in computers, electronics, data processing algorithms, etc., these in-process measurements are in need of major updates, both through software and hardware. The main motivating factor of this research is to determine and demonstrate, with acceptable measurement results, more efficient and accurate algorithms and hardware for in-process measurements of large-scale axis of rotation manufacturing processes, with an emphasis on turning operations. The next few sections will provide an overview of the how the axis of rotation affects both the machining and in-process measurements of turning operations and the objective and scope of what the research intends to demonstrate.

1.2. Axis of Rotation Overview

Historically, machine tool spindles have been considered to be very good compared to the axis motions and other structures on the machine [18]. However, as machine tool structures continue to improve their capability and precision, the demand for better component geometry and surface finishes have become more critical and spindles errors have become a larger percentage of the total error.

In order to achieve the best component profile and surface finish, the performance of the spindle must be characterized to the lowest errors possible. In 1985, the American National Standards Institute (ANSI) and the American Society of Mechanical Engineers (ASME) published *ANSI/ASME B89.3.4M* Axes of Rotation: Methods for Specifying and Testing [58]. As recently as of 2010, the new version of the standard has been published [18]. This standard characterizes vocabulary and testing procedures for axis of rotations and some important concepts from the standard are outlined and introduced in this research.

1.2.1. Axis of Rotation

With the ever evolving field of precision engineering, state-of-the-art machines were beginning to take shape. The diamond turning machines developed could machine complex geometries to accuracies better than $25\ nm$ ($1\ \mu in$), with optically flat surfaces of less then $5\ nm\ R_a$ ($0.2\ \mu in\ R_a$) [53]. The most important component of a diamond turning machine is the spindle axis, because it provides a very accurate rotation of a component or tool in the machining process. If the spindle performance is poor, meaning lots of error motion, dynamics and temperature effects, then the actual component surface profile and surface finish will be of poor quality. Spindle performance is a major concern for metrology equipment such as roundness testers, which require an accurate reference axis; thus any deviation from theoretically pure rotation can be a direct influence to the error of the measurements. Review of the literature confirms that spindles are a major component in the overall accuracy of a machine tool or metrology instrument/machine. The following sections describe what major influences affect axis of rotation metrology.

1.2.2. Error Motions

The axis of rotation standard defines vocabulary associated with the measurement of the motions of an axis of rotation. A spindle is a physical structure of a machine or metrology tool. It is a combination of a stator, non-rotating component of the structure, and a rotor, the rotating component of the structure. There are either mechanical or fluid bearings in the rotor, to allow the rotor to rotate with respect to the stator. The desired motion of a spindle is pure rotation, with no motion in the other degrees of freedom. Since there can be no pure rotational motion, motions in the other degrees of freedom are called error motions. Normally on spindles, the z axis is through the axis of rotation or center line. If the reference axis of the rotor is aligned with the z axis of the stator, any linear (x, y, z) or angular (θ_x, θ_y) motion, is an error motion. FIGURE 3 shows the different measurements of the spindle error motions.
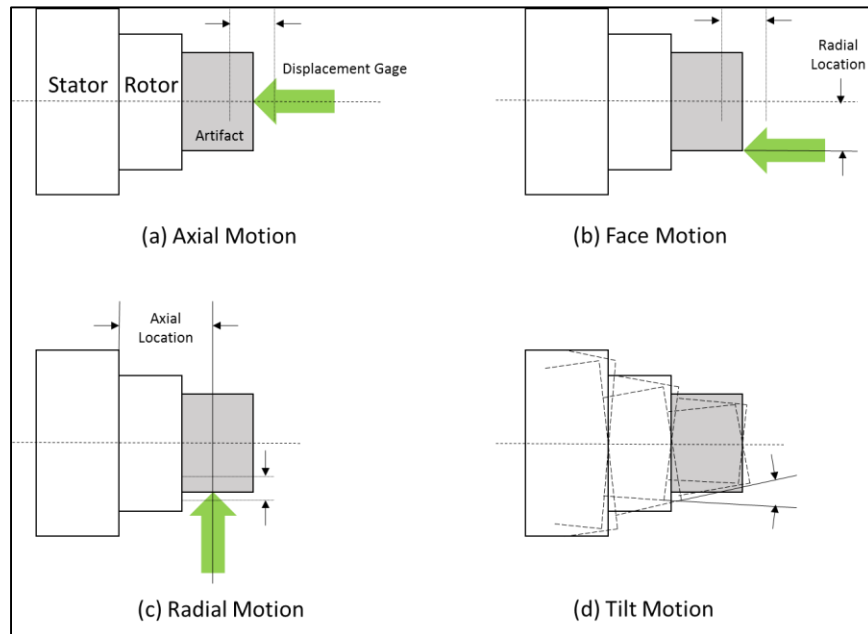
FIGURE 3: Different error motions of the axis of rotation B89.3.4m [18]

In the standard, all measurements of the errors are made with a displacement indicator. The axial error motion is measured when the displacement indicator is aligned along the axis, as can be seen in FIGURE 3a. The radial error motions are measured perpendicular to the axis of rotation, as can be seen in FIGURE 3c. The axial location is the distance from a reference line, usually on the stator, to the displacement indicator. It is important to know this distance because the tilt error motion can affect the measurement. The face motion is measured in the axial direction, but the displacement indicator is set at a known distance from the axis of rotation, as can be seen in FIGURE 3b. The tilt motion can be measured in two ways. It can be derived from two radial motion measurements, with the distance known between the displacement indicators. It can also be measured with two face motion measurements, with the distance known between the two displacement indicators

Normally all the error motions of the spindle are made with the displacement indicator targeting a precision artifact that is mounted in the spindle. Using a low-form error artifact, $25\ nm$ ($1\ \mu in$), is normal in the testing of precision air-bearing spindles, however, the testing done in this research is on a synchronous two revolution per minute (RPM) rotary table, with un-calibrated large-scale components. While all other error motions are important, this research is only concerned with the radial error motion of the spindle, which leads to the form error measurement of the components as of most interest, as well as its diameter. However, the introduction of the axis of rotation standard is a necessary step to justifying the research.

1.2.3. Centering Error

Before taking any type of measurement on a component, the component should be aligned to the axis of rotation. No component is ever truly perfectly aligned and thus there is a misalignment of the component's axis of symmetry to the spindle axis of rotation [18]. The following example for the misalignment of a circular component is taken from Gredja [19] and Cappa, *et al* [4], with the example considering the radial error motion. FIGURE 4 shows a view of a misaligned circular component and the axis of rotation. The circular component's radius is defined as R, where it's center is R_o, and is not aligned with the axis of rotation center, O. This misalignment is called the eccentricity and is represented by e.
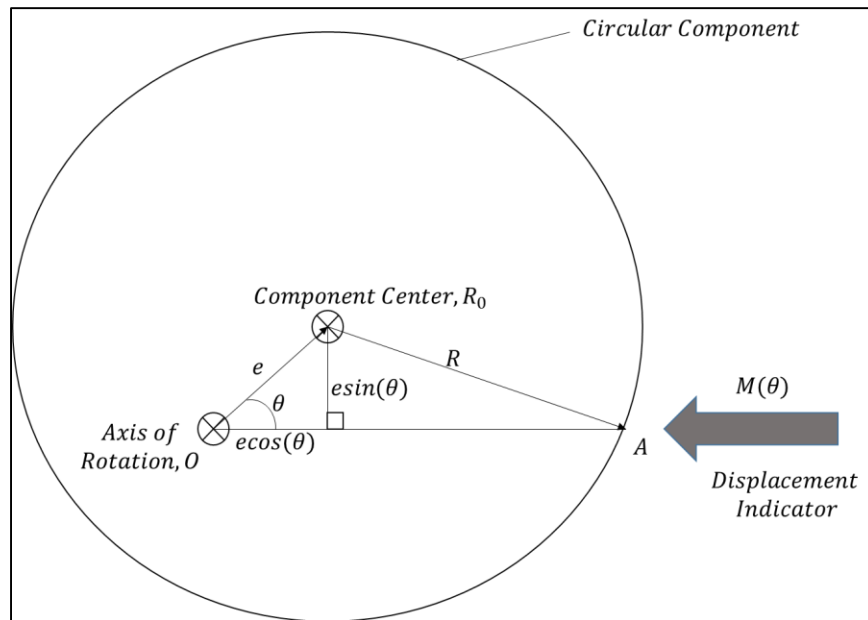
FIGURE 4: Sketch of eccentricity of component to axis of rotation [9] [10]

If the axis of rotation is perfect, the displacement indicator will measure the change in length of the line segment $\overline{OA}$, which lies between the indicator measuring point A and the axis of rotation O. The length of $\overline{OA}$ can be written in terms of eccentricity, e, and the radius of the circular component, R, stated in Eq. (1).

$$\overline{OA} = e\cos(\theta) + \sqrt{R^2 + e^2 \sin^2(\theta)} \qquad (1)$$

When the amount of eccentricity is small compared to the radius of the component, the second term in Eq. (1) can be simplified with a first-order approximation expansion of $\sin^2(\theta)$, which results in Eq. (2).

$$\overline{OA} = e\cos(\theta) + R + \frac{e^2}{2R}\sin^2(\theta) \qquad (2)$$

Simplifying the $\sin^2(\theta)$ term with trigonometric identities, Eq. (3) represents a simplified version of Eq. (2).

$$\overline{OA} = e\cos(\theta) + R + \frac{e^2}{4R}(1 - \cos(2\theta)) \qquad (3)$$

The first two terms in Eq. (3) are the polar form of a limacon. A limacon is a convex curve generated by a point lying on a line at a fixed distance from the intersection of the line with a fixed circle, the line rotating about a point on the circumference of the circle. In most radial error applications, the eccentricity is removed mathematically with a best-fit circle. The eccentricity is not an error motion in radial error motion measurements and is considered the fundamental error. Any frequency after the fundamental is considered an error motion.

All radial error motions measurements, as well as CMM measurements of the components, made in this research have the eccentricity removed with a best-fit circle. The best-fit circle equation used to remove eccentricity is from the *ASME B89.3.4M* standard [18]. Eq. (4), Eq. (5) and Eq. (6) represent the equations used to calculate the best-fit.

$$a = \frac{2}{n} \sum_{i=1}^{n} R_i cos(\theta_i) \tag{4}$$

$$b = \frac{2}{n} \sum_{i=1}^{n} R_i sin(\theta_i) \tag{5}$$

$$R = \frac{\sum R_i}{n} \tag{6}$$

Where a and b are the x and y center points of the best-fit circle, respectively and R is the radius of the best-fit circle. Thus the best-fit circle is calculated by Eq. (7)

$$R_{BF} = R + acos(\theta_i) + bsin(\theta_i) \tag{7}$$

Now with the best-fit circle defined, the actual radial error motions can be calculated by subtracting out the best-fit circle, Eq. (7), from the radial measurement, M_{radial}.

$$EM = M_{radial} - R_{BF} \tag{8}$$

To re-iterate, in this research, only radial error measurements are determined, thus it is important to understand that this eccentricity is removed because it is not considered an error motion, but is just a rigid body translation of the artifact relative to the spindle.

1.2.4. Synchronous vs. Asynchronous

If the component which the displacement indicator is measuring is perfectly round, the indicator will measure the total error motion of the spindle. The total error motion of the spindle measurements has two types of error motions: synchronous error motion and asynchronous error motion [18]. The synchronous error motion, also known as average error motion, is the error motion that repeats, at integer values, from revolution-to-revolution. It is calculated by taking the average of the revolution-to-revolution data, at the integer values. The asynchronous error motion is the error motion that does not repeat at integer values from revolution-to-revolution. The asynchronous error motion is calculated by subtracting out the synchronous error motion from the total raw error motion.

Normally the synchronous and asynchronous error motions are displayed in polar plots. The synchronous error motion plot can be demonstrated with plotting out the total error motion and then plotting the average of that total error motion overlaid. FIGURE 5 shows synchronous error motions for 10 revolutions of data with 500 samples per revolution.
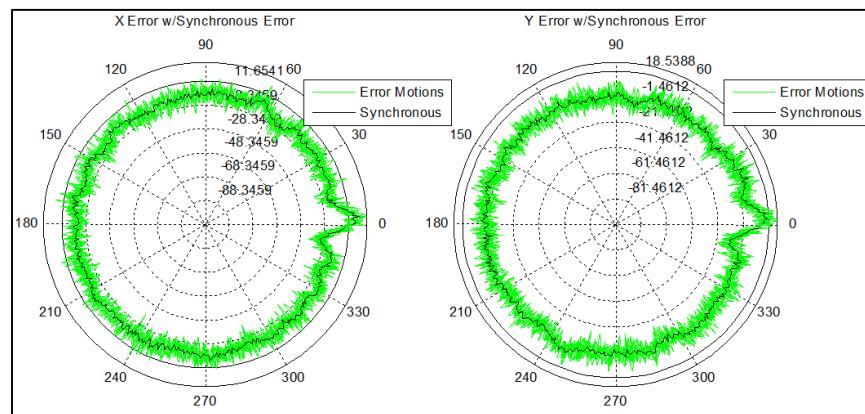
FIGURE 5: X and Y error motion with synchronous error motion

FIGURE 6 shows the asynchronous error from FIGURE 5 error motions, which is the synchronous error motion subtracted from the total error motion.
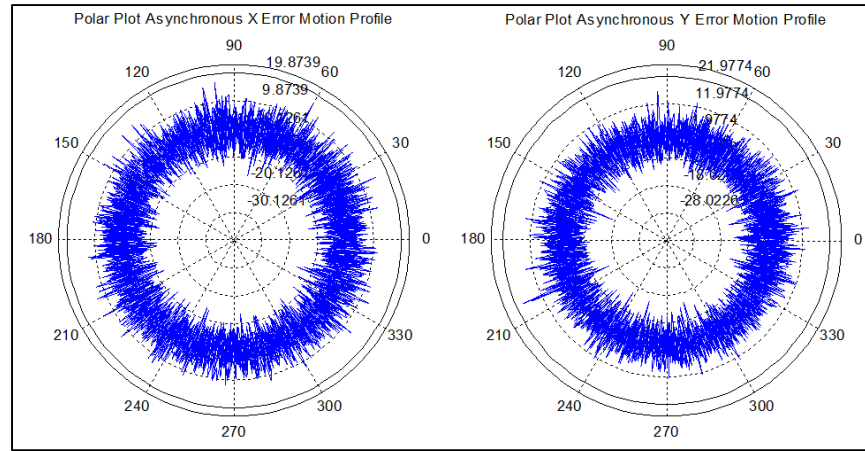
FIGURE 6: X and Y asynchronous error motion

The synchronous error value is the peak-to-valley range of the measurement and the asynchronous error value is the maximum scaled width of the asynchronous error band [1] [18]. The asynchronous value is normally much larger than the synchronous value, in magnitude. The synchronous error motion data is used to determine all component form errors, in this research. The asynchronous error motion is of more concern for spindle error motions of ultra-precision machine tools since it can lead directly to undesirable surface finish. The asynchronous error motion is not considered in this research.

1.3. Reversals and Error Separation Methods

With the axis of rotation, synchronous and asynchronous error motions and eccentricity defined, the subject of measurement reversals and error separations can be discussed. This section will describe classical reversal and error separation methods with general overviews of the methods and detailed schematics for graphical means. The only error separation method that will not be described in this section is the multi-probe method, which is a major basis in this research. It will be fully detailed in a later section and will be employed in the measuring instrument developed and used for the in-process metrology methods.

Reversal and error separation methods are one of the fundamental concepts for rotational metrology [1] [18] [20]. Reversal methods are very simplistic, but very powerful methods that yield a complete separation of the form errors of the component and the spindle's error motions [20]. The reversal methods thus can be used on artifacts, components and instruments without needing a comparison with a master artifact, which is traceable to a national standards laboratory, such as the National Institute of Standards and Technology (NIST). The error separation methods however are not true reversals, in the sense of the definition, and also are not capable of a complete separation of the spindle error and component form error [20]. Evans, Hocken and Estler published a broad survey of the reversal and error separation methods, which include measurements utilizing straightedges, optical flats, master ball artifacts and interferometry instruments [20]. The next sections give brief overviews of rotational reversals and spindle error separation methods.

1.3.1. Reversal Methods

The reversal methods described are different than error separation methods because they provide a complete separation of spindle error motions and form error of the component [18] [20] [21]. Reversals require two measurements to compute a single component of spindle error (i.e. radial). Both the component and displacement indicator must be moved between measurements. A reversal is theoretically better than other methods, but it requires very stiff hardware to achieve nanometer-level repeatability.

Bryan's initial work on spindle and machine tool metrology showed the need for separating the error of a master ball from the error motions of the spindle [57]. For all measurements in a spindle application, the displacement indicator used for measurements will detect a combination of the spindle error motions and component form error. When the errors of the spindle motions and component form are of the same magnitude, there is a need to separate the two [1]. Donaldson extended the simple straightedge reversal to spindles tested with a master ball to separate the errors [21]. FIGURE 7 illustrates the Donaldson reversal method.
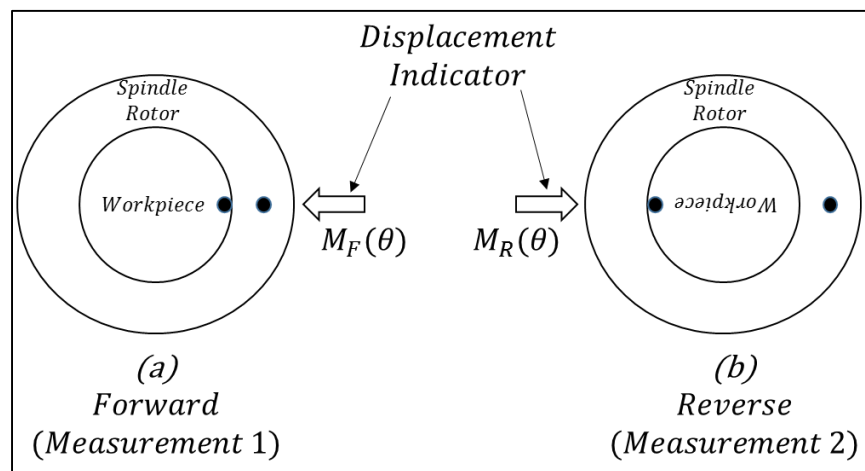
FIGURE 7: Donaldson reversal method

With the first setup of the Donaldson reversal, the angular displacement of the rotor, component and displacement indicator are aligned with a fiducial, seen in FIGURE 7a. For the reverse measurement, the displacement indicator and component are rotated 180° with respect to the rotor, as seen in FIGURE 7b. The component form error and spindle radial error motion can be determined completely from the two measurements. Eq. (9) and Eq. (10) show the form error and spindle radial error for the Donaldson reversal.

$$R(\theta) = \frac{M_F(\theta) + M_R(\theta)}{2} \tag{9}$$

$$S(\theta) = \frac{M_F(\theta) - M_R(\theta)}{2} \tag{10}$$

Where $R(\theta)$ is the component form error and $S(\theta)$ is the spindle radial error. This reversal method is typically used for radial error motions, but can be used for tilt error motion with the use of a cylindrical component. This reversal method laid the ground work for the other reversal methods in spindle metrology. Estler used the Donaldson reversal for face error motion reversals [1] [18]. In essence the measurements are the same, however, the measurements are now taken on the face of a circular component.

Grejda enhanced both Donaldson reversal and Estler's face error motion reversal. Grejda introduced a precision rotary table which could rotate the spindle stator 180° with respect to the displacement indicator, which is never moved [47]. To solve the eccentricity issue with the setup, a special reversal chuck with a lapped spherical pilot and precision-ground holes sized for slip fit, will index the component with an alignment pin. This method eliminated the need for multiple indicators and repositioning indicators, which changed the accuracy of the measurements to nanometer-level. FIGURE 8 shows a schematic view of the Grejda reversal.
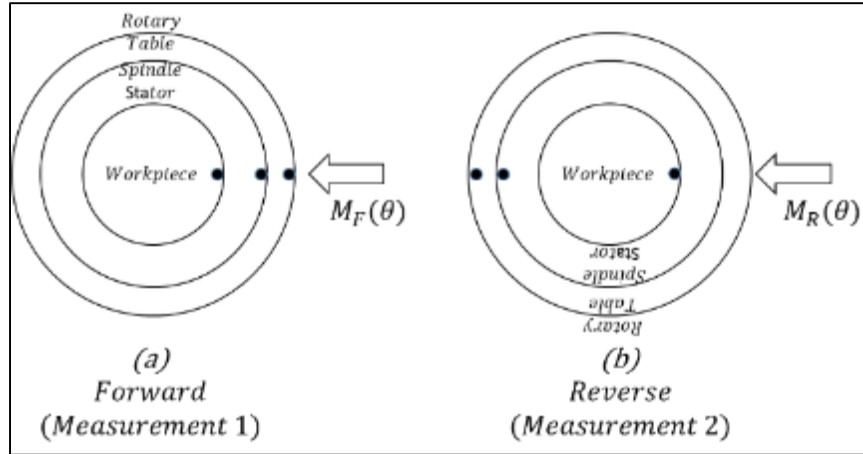
FIGURE 8: Schematic of Grejda reversal

The benefit from the Grejda reversal is it not only reduces measurement uncertainty, but also in general, it simplifies the reversal method. It works just as well for the Estler face error motion reversal and can actually be used for multi-position error separation, if necessary [47].

There is a generalized reversal formulation that measures form error of a spherical component at an arbitrary latitude [1] [18]. In theory it is possible to separate the spindle errors from the component form errors at an inclined plane with respect to the axis of rotation, if the radial and face errors are independently measured using a reversal. FIGURE 9 shows a schematic of the generalized reversal method.
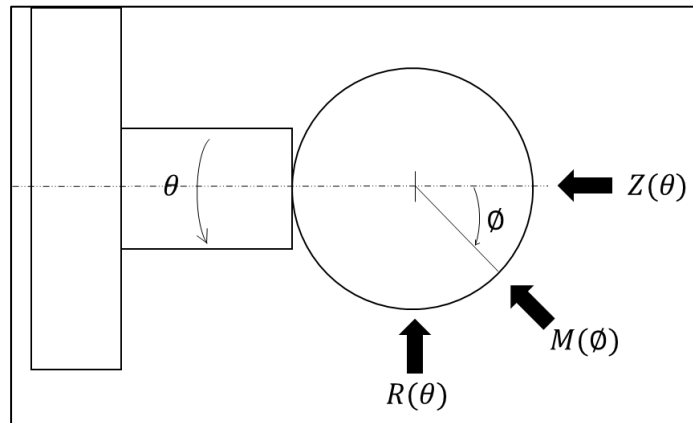
FIGURE 9: Generalized reversal formulation method

From the figure above, the displacement indicator locations are at the axial position $Z(\theta)$ and radial measurement $R(\theta)$ and the general measurement is taken at an arbitrary latitude $M(\emptyset)$. Eq. (11) shows the generalized measurement from the arbitrary latitude including the form error of the component, $P(\emptyset)$.

$$M(\emptyset) = R(\theta)\,sin(\emptyset) + Z(\theta)\,cos(\emptyset) + P(\emptyset) \qquad (11)$$

Once the radial and axial error motions are known, the spindle and component form error can be separated from the spindle at any arbitrary latitude without any additional reversals.

These methods are good for calibrations and laboratory setting, however in a shop-floor environment, these methods would be much more complex to implement because of all the extrinsic effects. In this research, the measuring instrument must be adaptable to shop-floor usage, so any type of reversal method is not favorable and would take a great deal of effort to implement in the hardware. However, error separation methods are much more adaptable and produce almost equivalent spindle error motion and form error results as reversal methods [1].

1.3.2. Error Separation Methods

Evans, *et al* [20] describe error separation methods as model-based because they incorporate "assumptions about the component form error in the measurement". Both the multi-position and multi-probe methods use Fourier series to represent the spindle error motion or the component form error. The multi-step method uses Fourier series for the spindle error motions while the multi-probe method uses Fourier series for representing the component form error [1].

The multi-step error separation uses a series of measurements in which the component is indexed around, in equal angular spacing [1] [6] [18] [19] [20] [35] [47]. The standard method for implementing the multi-step methods requires data with the component oriented in n different equally-spaced angular increments around its circumference. When enough data is sampled around the circumference of the component, it is then possible to separate the component form error, which moves with every step, from the spindle error, which remains static. FIGURE 10 shows a schematic of the multi-step error separation method.
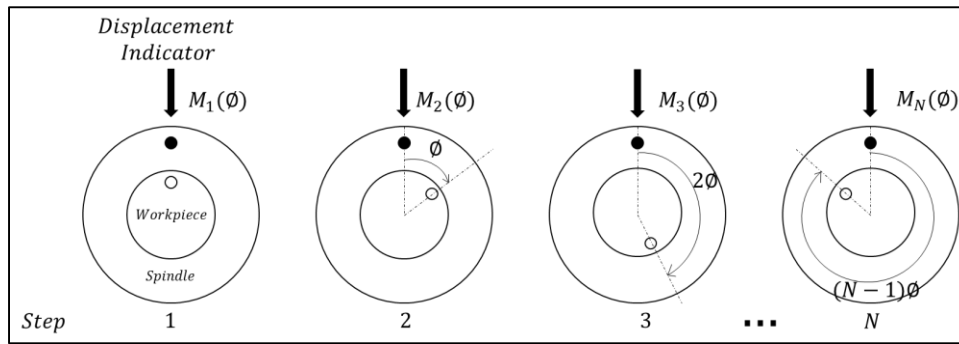
FIGURE 10: Multi-step error separation method from *B89.3.4m* [18]

From the above picture, with a single displacement indicator, the component is indexed and each measurement has a combination of the spindle error and component form error. Each measurement can be expressed in the following equation containing the above mentioned errors, where the form error, $R(\theta)$, is phase shifted with each indexed point.

$$M_n(\theta) = S(\theta) + R(\theta + \emptyset(n-1)) \tag{12}$$

Where $1 \leq n \leq N$. Summing the measurements for N, and solving for the radial

spindle error motion, $S(\theta)$, leads to Eq. (13).

$$S(\theta) = \frac{1}{N}\sum_{n=1}^{N} M_n + \frac{1}{N}\sum_{n=1}^{N} R(\theta + \emptyset(n-1))$$

$$= \frac{1}{N}\sum_{n=1}^{N} M_n + \frac{1}{N}\sum_{k=1}^{N-1} R(\theta + k\emptyset) \tag{13}$$

The component form error can be presented as a Fourier series.

$$R(\theta) = \sum_{p=1}^{\infty} A_p \cos(p\theta) + B_p \sin(p\theta) \tag{14}$$

After using Eq. (13) and Eq. (14), and simplifying, the estimated spindle radial error

and component form error can be determined from Eq. (15) and Eq. (16).

$$S(\theta) \approx \frac{1}{N}\sum_{n=1}^{N} M_n \tag{15}$$

$$R(\theta + n\emptyset) = M_n(\theta) - S(\theta) \tag{16}$$

The multi-step error separation method is not a very well suited approach to in-process

measurements, thus it will not be discussed any further.

1.4.   Diameter Measurements in Manufacturing

In-process diameter measurements are normally done using a mechanical instrument, such as a caliper or micrometer, depending on the size and accuracy needed for a measurement. A CMM could also be used for diameter measurements; however, it is not feasible for in-process measurements. The type of measurement instrument could also depend on if the measurement is an inner or outer diameter. Some researchers have used very complex, non-contact double-edged laser-scanning combined with grating displacement measurements [2] to calculate in-process diameter measurements. However, this measurement system is very expensive, has only been described theoretically and not been verified correctly through experimentation. Another method for measuring outer diameters in manufacturing is using a friction-roller wheel supported by a spring structure of fixed equipment and is closely contacted with the surface of the rotator [2] [51]. When the rotator rotates, encoder pulses and a Hall switch, control the counting valves. When the magnet goes through the Hall switch, the valve will open. Simultaneously, a computer sums up the pulses. One rotation of the magnet goes though the Hall switch and the valve closes and the total number of pulses from the encoder is used to calculate the diameter. This method is not very accurate because of environmental factors and isn't used very often, if at all.

The caliper is a translation of the linear form of a component, which is accomplished by referencing the calipers jaws to a measurement scale by mechanical means [42]. As useful as calipers are for simple measurements, they have the tendency to not produce very accurate measurements. Calipers are can be classified as two-point measurements or a distance measurement. These two-points cannot precisely represent a diameter if the component shape is odd-lobed. Another fault is the caliper suffers from a cosine error and abbe offset.

The micrometer, which is a specialized version of a caliper, is purely a screw turning in a nut with the point or end of the screw advancing toward or receding from the opposite anvil of a C-frame [42]. Another issue with the calipers and micrometers is that these instruments can only measure a certain range of sizes. This issue then leads to having multiple instruments of various sizes as well as reference artifacts to check the distance from end to end. As the size of the component goes up, the measurement errors increase.

With the issues of the mechanical instrument measurements, there is a need to develop a measuring instrument using a more precise method for in-process diameter measurements. This research describes such a measuring instrument, which has the means to measures both diameter and form error, with three contact points on the surface of the circular component. The method used to reconstruct the diameter of the component is based on a geometrical model, which uses the area and semi-perimeter of a triangle to produce a circumcircle, which is an estimate of the circular components diameter.

1.5. In-process Metrology Method Improvement

The objective of this research is to improve in-process measurements of diameter and form error measurements, simultaneously, for large-scale components, by developing software through mathematically sound algorithms and demonstrated with the development of a novel measuring instrument, designed to use the multi-probe error separation method to determine the circular component form error, as well as measure the diameter of the component by using a geometrical model with three points. With the diameter measurement, the center position of the component can also be determined, in the measuring instrument's coordinate system. This is a byproduct of the design and will only be used for determining the direction cosines later in the research. Testing results from the measuring instrument are compared to a CMM.

The measuring instrument is designed with three pivoting arms, attached to a monolithic steel body that has milled pockets to fit encoder modules. The measuring instrument can interface with a $25.4\ mm\ x\ 25.4\ mm$ ($1''\ x\ 1''$) tool-post turret. The arms are attached to the body of the measuring instrument via a clamp ring with a locking screw. The clamp ring is connected to a lock ring and then finally connected to a bore adapter. The bore adapter is positioned on the body. Each arm assembly is connected to the high-precision encoder module, which is located inside the body. Each arm is attached, at the opposite end of the pivot, with a low-form error steel sphere used to make contact with the surface of the component. The arm is spring loaded with a beam spring that is attached to the lock ring. The clamp ring with the locking screw is used to ensure the correct spring force is on each arm to ensure contact with the component. The sensing system in the measuring instrument is a high-resolution absolute encoder, with an integrated high-precision bearing, which determines the arm's absolute position relative to a reference mark on the scale of the encoder. The encoder module data, as well as the measuring instrument's kinematic model, is used to produce all metrology results in this research.

The final objective of this research is the verification of the multi-probe error separation and diameter with the measuring instrument along with an uncertainty budget for each measuring process.

The research is structured as follows. Chapter 2 discusses the multi-probe error separation method in full detail, as well as how the planar angle locations for the multi-probe method are determined through the measuring instrument design. Chapter 3 discusses the geometrical model used for determining the diameter measurement, as well as the center position used for the direction cosines. Chapter 4 fully describes and details the measuring instrument used to incorporate all forms of metrology discussed in this research. Chapter 5 discusses the experimental setup, preliminary tests and results from the diameter and form error tests using the measuring instrument. Chapter 6 discusses uncertainty sources affecting both the form error and diameter measurements and combines all uncertainty values in a budget to quantify the measuring process. Chapter 7 discusses the conclusions from the research and future work.

CHAPTER 2: COMPONENT FORM METROLOGY

2.1. Multi-probe Error Separation Method

Whitehouse is one of the first researchers to demonstrate the multi-probe error separation method, with the use of capacitance indicators that target an artifact, collecting data to separate the component form errors from the spindle errors [6] [7]. The multi-probe error separation method normally uses three displacement probes (e.g. capacitance indicators) [1] [35] [36], however, in this research, the measuring instrument used for testing, uses high-resolution angular encoder modules. Normally the capacitance indicators are arranged around the circumference of the component; however, the angular encoders are attached at pivot points/joints on the measuring instruments body, as mentioned in Chapter 1, and each arm is attached to the body of the measuring instrument at pivot points and a low-form error steel sphere is attached at opposite end of each arm. Each arm sphere is in contact with the component surface and represents the measurement point needed for the multi-probe method. In chapter 4, the details of integrating the angular encoder modules into the measuring instrument are discussed.

The measurement points are labeled as $M_A(\theta)$, $M_B(\theta)$ and $M_C(\theta)$, where $M_A(\theta)$, $M_B(\theta)$ and $M_C(\theta)$ are separated in the xy plane from the positive x axis by planar angles α, β and γ. FIGURE 11 shows a general schematic of the multi-probe method.
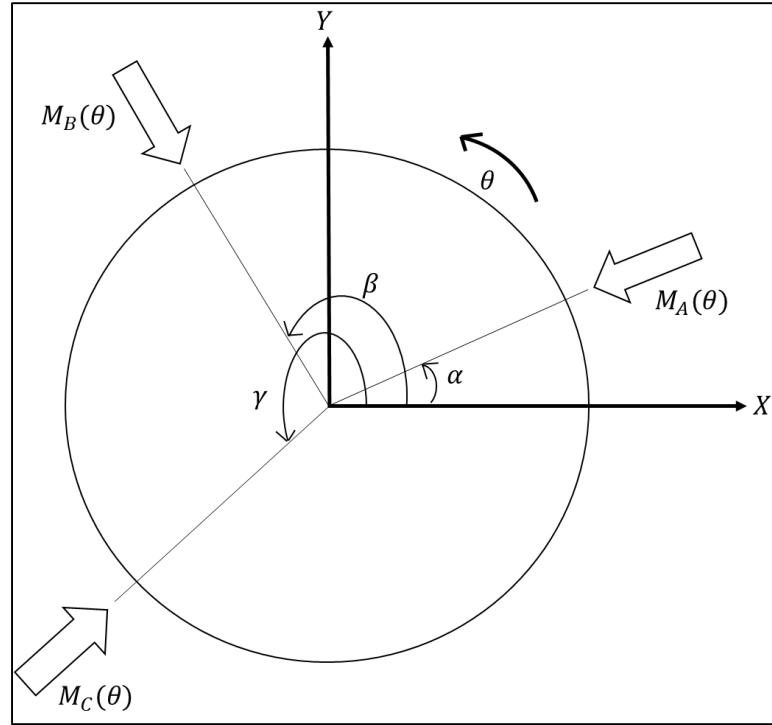
FIGURE 11: Three-point error separation method for component form error and spindle error motion

The equations for the measurements are a combination of the component form error, $P(\theta)$, including the phase shift of the measurement point locations, and the $x(\theta)$ and $y(\theta)$ coordinates of the spindle error motions.

$$M_A(\theta) = P(\theta - \alpha) + x(\theta)\cos(\alpha) + y(\theta)\sin(\alpha) \tag{17}$$

$$M_B(\theta) = P(\theta - \beta) + x(\theta)\cos(\beta) + y(\theta)\sin(\beta) \tag{18}$$

$$M_C(\theta) = P(\theta - \gamma) + x(\theta)\cos(\gamma) + y(\theta)\sin(\gamma) \tag{19}$$

In most published research, the angle α is used as the reference or initial angle for the multi-probe method. Thus $\alpha = 0°$ is used, so Eq. (17), simplifies to $M_A(\theta) = P(\theta) + x(\theta)$. This simplified version of Eq. (17) is used throughout the research, for simulation and real data.

With the simplified equation, the multi-probe approach then combines these three measurements through a linear combination of a weighted measurement, $M(\theta)$, using coefficients a and b.

$$M(\theta) = M_A(\theta) + aM_B(\theta) + bM_C(\theta) \tag{20}$$

Where a and b coefficients are found from solving Eq. (21) and Eq. (22) simultaneously.

$$a\cos(\beta) + b\cos(\gamma) + 1 = 0 \tag{21}$$

$$a\sin(\beta) - b\sin(\gamma) = 0 \tag{22}$$

Thus the coefficients are:

$$a = -\frac{\sin(\beta)}{\sin(\beta - \gamma)} \qquad b = \frac{\sin(\gamma)}{\sin(\beta - \gamma)} \tag{23}$$

The form error of the component can be modeled as a Fourier series of periodic motion, with Fourier coefficients represented by A_k and B_k. The form error equation is:

$$P(\theta) = \sum_{k=2}^{\infty} A_k\cos(k\theta) + B_k\sin(k\theta) \tag{24}$$

Where $k,$ is the series count, but for the multi-probe method, it is the number of undulations per revolution (UPR). Eq. (25) shows the results when Eq. (17), Eq. (18), Eq. (19) and Eq. (24) are substituted in Eq. (20), using trigonometric angle identities for the cos and sin terms, and grouping common terms; $M(\theta)$ can be represented as:

$$M_A(\theta) + aM_B(\theta) + bM_C(\theta)$$

$$= \sum_{k=1}^{\infty} A_k cos(k\theta)\,(1 + acos(k\beta) + bcos(k\gamma))$$

$$+ \sum_{k=1}^{\infty} A_k\,sin(k\theta)(asin(k\gamma) - bsin(k\beta)) \tag{25}$$

$$+ \sum_{k=1}^{\infty} B_k\,sin(k\theta)\,(1 + acos(k\beta) + bcos(k\gamma))$$

$$+ \sum_{k=1}^{\infty} B_k\,cos(k\theta)(bsin(k\gamma) - asin(k\beta))$$

Notice that the parentheses in Eq. (25) are similar to Eq. (21) and Eq. (22) and setting those parentheses values in Eq. (25) to $\delta_k = 1 + acos(k\beta) + bcos(k\gamma)$ and $\varepsilon_k = bsin(k\gamma) - asin(k\beta)$, Eq. (25) can be simplified to Eq. (26).

$$M(\theta) = \sum_{k=2}^{\infty} (A_k\delta_k + B_k\varepsilon_k)cos(k\theta) + \sum_{k=2}^{\infty}(B_k\delta_k - A_k\varepsilon_k)sin(k\theta) \tag{26}$$

The coefficients of $cosk\theta$ and $sink\theta$ are the Fourier coefficients of the summed measurement, so A_k and B_k can be found by solving the matrix in Eq. (28). F_k and G_k are the Fourier coefficients of $M(\theta)$, and found by Discrete Fourier Transform.

$$M(\theta) = \sum_{k=2}^{\infty} F_k cos(k\theta) + G_k sin(k\theta) \tag{27}$$

$$\begin{bmatrix} \delta_k & \varepsilon_k \\ -\varepsilon_k & \delta_k \end{bmatrix} \begin{Bmatrix} A_k \\ B_k \end{Bmatrix} = \begin{Bmatrix} F_k \\ G_k \end{Bmatrix} \tag{28}$$

Notice that Eq. (26) and Eq. (27), have the series starting at $k = 2$. This is done to exclude the fundamental error component, which is the eccentricity of the component setup. Thus the centering error described in section 1.2.3 is not included in the graphics displayed later in the research. Also to note, when $k = 1$, Eq. (25) is zero, as defined by Eq. (21) and Eq. (22).

With A_k and B_k now known, the component form error, $P(\theta)$, is determined by Eq. (24).

For completeness of the multi-probe error separation method, the form error is now used to determine the spindle error motion of the in the x and y directions. To determine the spindle error motions, Eq. (18) and Eq. (19) are solved simultaneously to determine the spindle error motions. The $y(\theta)$ direction is found by subtracting Eq. (18) from Eq. (19), to eliminate the $x(\theta)$, thus $y(\theta)$ is expressed as:

$$y(\theta) = \frac{[-M_b(\theta) + P(\theta - \beta)] cos(\gamma) + [M_c(\theta) + P(\theta - \gamma)]cos(\beta)}{sin(\gamma - \beta)} \tag{29}$$

Now that the y direction is expressed, to solve for the x direction, Eq. (18) or Eq. (19) is used, with substituting Eq. (29). The x direction can be expressed as Eq. (30). Eq. (19) is used to determine the x direction spindle error.

$$x(\theta) = \frac{[M_c(\theta) - P(\theta - \gamma)] - y(\theta)sin(\gamma)}{cos(\gamma)} \tag{30}$$

Eq. (29) and Eq. (30) are expressed in terms of the angles β and γ because the measuring instrument will not have a measuring point aligned with either the x or y axis, so the angles of the measuring points need to be determined beforehand and then the form error and spindle errors can be determined for the x and y directions.

The above formulas will be the basis of the software for determining the form error of the component under test. To prove the multi-probe method is capable of reconstructing the component profile, synthetic data is created, with and without noise, and the above algorithms are used to simulate the component profile and then reconstruct the profile with the multi-probe method. The reconstructed profile will be compared to the simulated profile.

2.2.1. Simulation of Multi-probe Technique

Synthetic data is created using Eq. (17), Eq. (18) and Eq. (19), with and without noise. The noise levels of the signals are approximately $0.005\ mm$ (0.0002"), with a random uniform distribution. This noise level is chosen to represent a shop-floor test. The planar angle locations used for the synthetic data and reconstructing the component profile, are $0^{\circ}, 99.84375^{\circ}, 202.5^{\circ}$ (α, β, γ), which have proven to have low harmonic suppression [1] [19] [35] [36]. It is common practice to use zero as the first angle, or reference angular location, in the multi-probe method, because it simplifies Eq. (17) and is easier to determine $x(\theta)$ [1] [19]. FIGURE 12 and FIGURE 13 show the synthetic data without noise, and profile reconstructed as well as compared to the simulated profile. There are 25 UPR included in the simulated profile of the component and 10 UPR included in the simulated spindle errors. All 25 UPR are extracted from the simulated weighted measurement, which are used to truncate the approximate component profile.
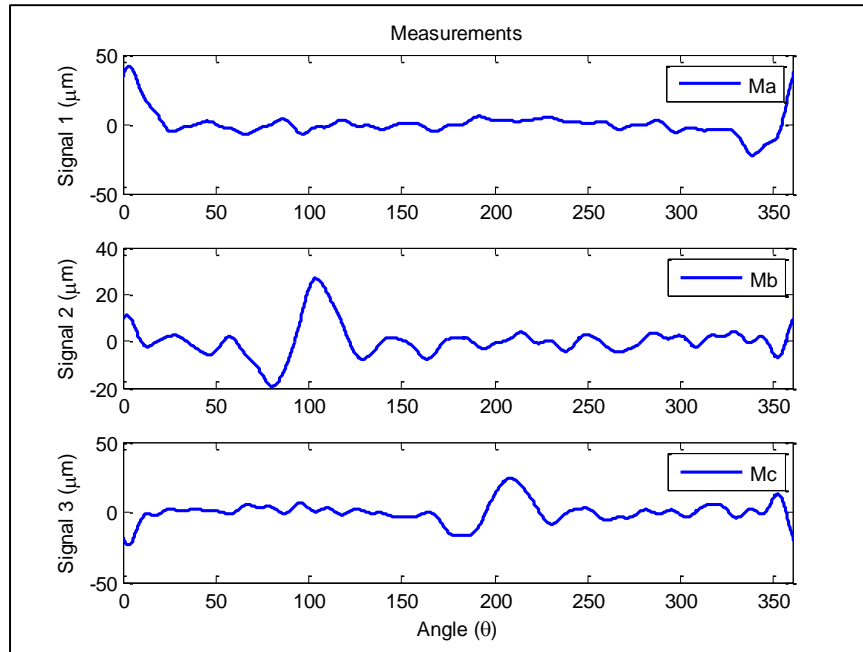
FIGURE 12: Synthetic data without noise.
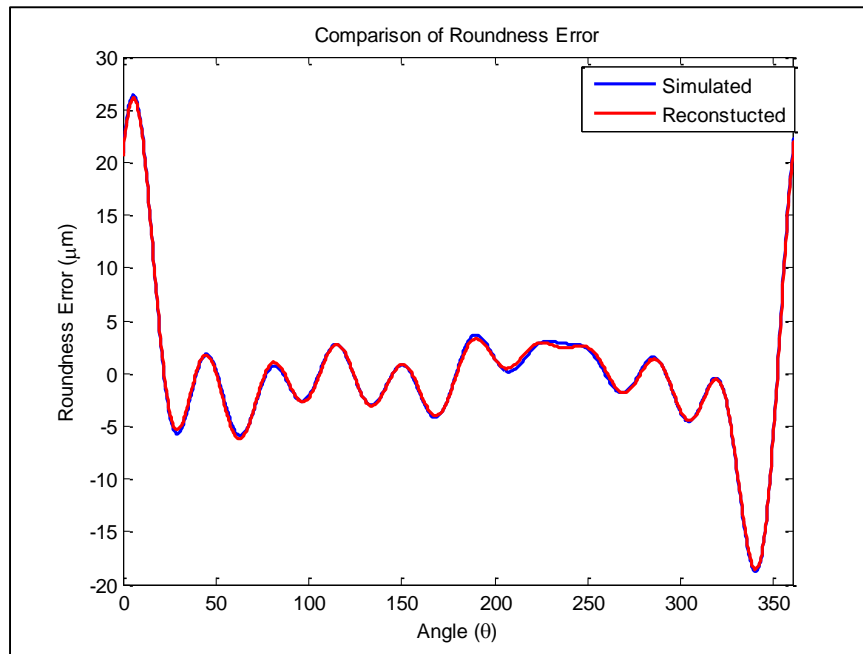
FIGURE 13: Reconstructed component profile and simulated component profile (w/out noise)

From FIGURE 13, it can be seen that the reconstructed profile does not 100% completely match the simulated profile. This can be attributed to the fact that the multi-probe error separation technique has assumption about the form error [18] [20] [21]. Even with published planar angles, harmonic suppression in the frequency domain is still included, even on a small scale [31] [32]. FIGURE 14 shows the point-to-point difference in the reconstructed to the simulated component profile. It has an approximate $\pm0.0004\ mm$ ($\pm0.000016"$) error band.
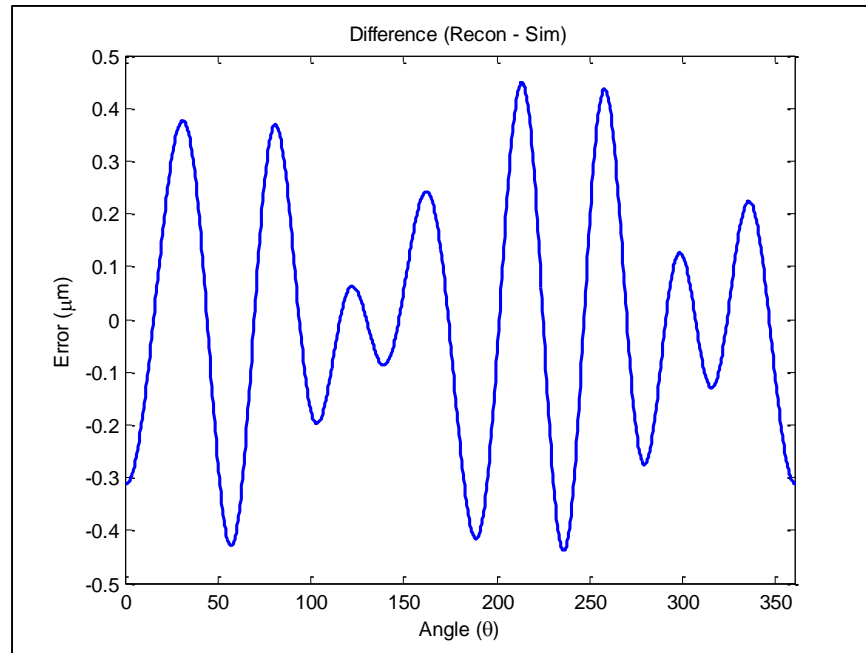
FIGURE 14: Point-to-point difference between simulated and reconstructed component profile (w/out noise)

FIGURE 15 and FIGURE 16 show the synthetic data now corrupted with noise and the approximate reconstruction of the component profile compared to the simulated profile.
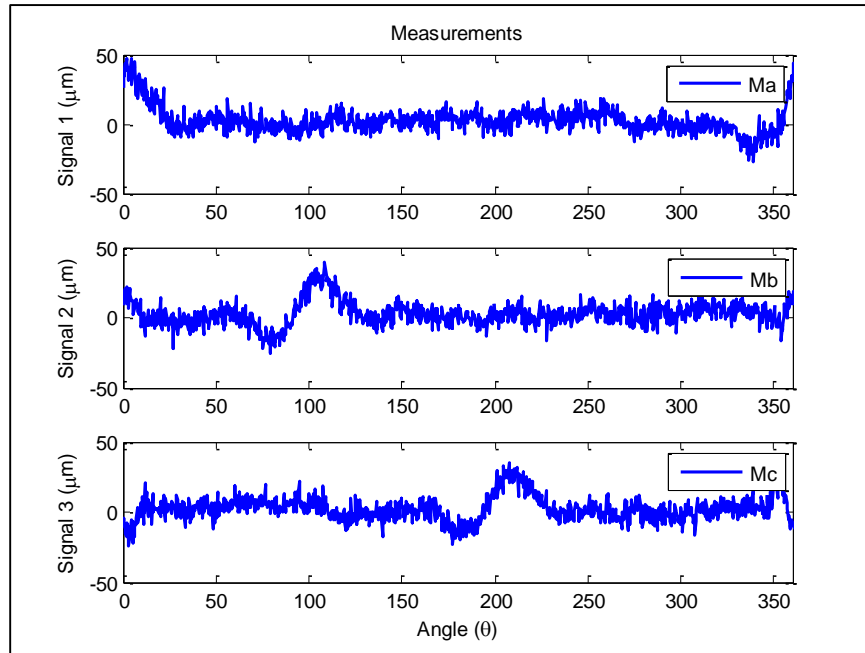
FIGURE 15: Synthetic data with noise ($0.005 \; mm \; (0.0002")$).
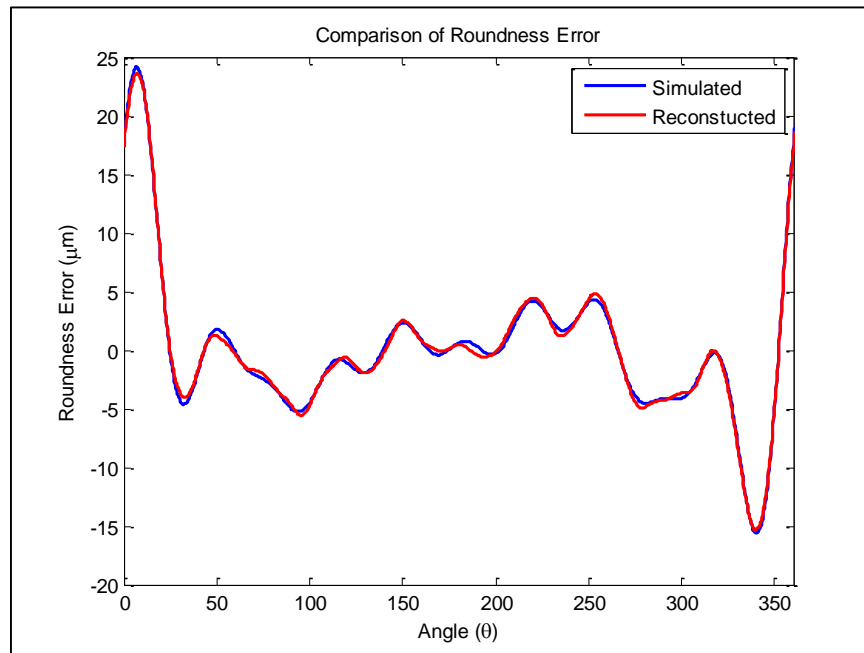
FIGURE 16: Reconstructed component profile and simulated component profile (w/noise)

From FIGURE 16, it can be seen that the reconstructed profile does not completely match the simulated profile, as was apparent in the simulation without noise. FIGURE 17 shows the point-to-point difference in the reconstructed to the simulated component profile. It has an approximate $\pm 0.0007\ mm$ ($\pm 0.000028''$) error band.
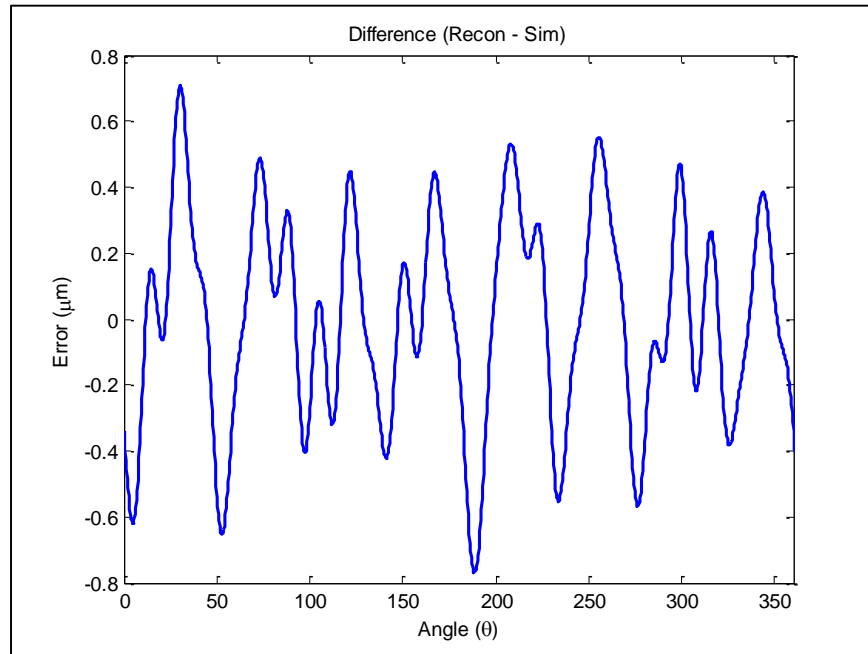
FIGURE 17: Point-to-point difference between simulated and reconstructed component profile (w/noise)

As can be seen from the simulations, the component profile can be reconstructed pretty accurately with the multi-probe error separation method with a reasonable amount of noise. Again, in published literature, there cannot be a complete separation and thus a complete reconstruction of the component profile error.

2.2. Planar Angle Orientation Determination

In the multi-probe error separation method, the performance of the method is dependent upon accurate knowledge of the location of planar angles α, β and γ [1]. Normally the multi-probe method is done using displacement indicators (i.e. capacitance indicators) and with the indicators precisely aligned in the same plane and sensitivity of all indicators matched, the accuracy of the method will be best [1]. Much work has been done on investigating the effects of the planar angular locations, normally predetermined, of the indicators, which control the accuracy of the separation of the harmonic content [1] [4] [5] [7] [9] [10] [11] [19] [34] [35] [36]. For the measuring instrument developed in this research the planar angles change with different component diameters and with the distance of the measuring instrument incremented from the component being measured. With the new measuring instrument concept, the planar angles can be calculated from both the measuring instrument coordinate system and spindle coordinate system, if the absolute arm angles are known. Since the measuring instrument uses absolute angular encoders, the absolute position of the arms can be determined, and this method can be used to determine the planar angles. FIGURE 18 shows a schematic of the measuring instrument in contact with the component.
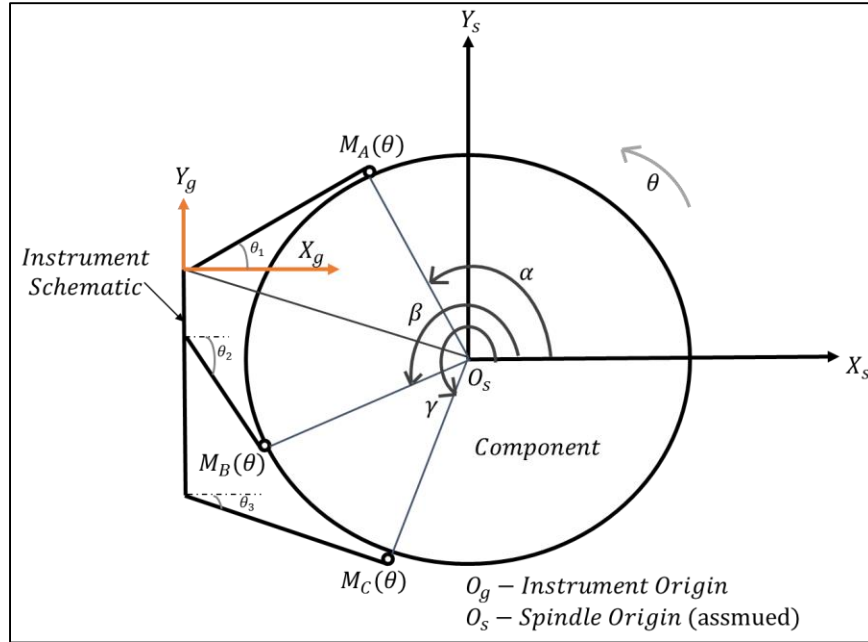
FIGURE 18: Measuring instrument in contact with component for planar angle determination

The measuring instrument coordinate system is treated as the global coordinate system because the measurements for the diameter and form error will be calculated from these coordinates. The planar angles are to be determined relative to the spindle coordinate system and measured from the positive x axis of the spindle. FIGURE 19 shows the relationship between the measuring instrument coordinate system and spindle coordinate system for each of the points of contact.
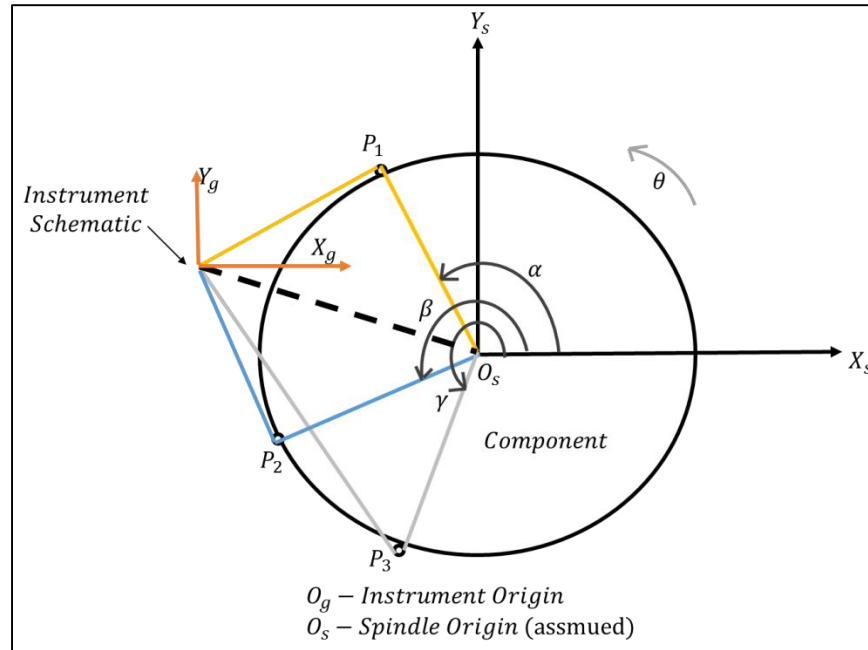
FIGURE 19: Relationship between measuring instrument and spindle coordinate systems

To determine the angles of the contact points, the direction cosines can be used to determine the angle locations, relative to the x axis of the spindle. FIGURE 19 shows the direction cosines vectors of each point, which consist of the component center coordinates and the surface contact point coordinates, in measuring instrument coordinates. From FIGURE 19, the direction cosines for each measurement point can be determined, in two-dimensions, as:

$$cos(\alpha) = \frac{a_1}{\sqrt{a_1^2 + b_1^2}} \tag{31}$$

$$cos(\beta) = \frac{a_2}{\sqrt{a_2^2 + b_2^2}} \tag{32}$$

$$cos(\gamma) = \frac{a_3}{\sqrt{a_3^2 + b_3^2}} \tag{33}$$

Where α, β and γ are the direction angles of the vectors with positive x and y axes, respectively. Point one's, p_1, coordinate points are (x_a, y_a), point two's, p_2, coordinate points are (x_b, y_b), point three's, p_3, coordinate points are (x_c, y_c) and the center coordinates of the component are (X_{cent}, Y_{cent}). $a_1 = <x_a - X_{cent}>$ and $b_1 = <y_a - Y_{cent}>$, are x and y vectors, respectively, from the spindle center to the surface contact point of point one. $a_2 = <x_b - X_{cent}>$ and $b_2 = <y_b - Y_{cent}>$, are x and y vectors, respectively, from the spindle center to the surface contact point of point two. $a_3 = <x_c - X_{cent}>$ and $b_3 = <y_c - Y_{cent}>$, are x and y vectors, respectively, from the spindle center to the surface contact point of point three. Using the defined a and b vectors, the direction cosines can be determined, by taking the inverse cosine, and the planar angle location, from the x axis of the spindle, can be determined for each of the measurement contact points.

The x and y coordinates for the surface contact points, as well as the component center coordinates, can be determined, in measuring instrument coordinates, by the arms angles and the kinematic model of the measuring instrument. The measuring instruments' physical design and kinematic model is detailed in a later chapter and in this later chapter, the necessary equations for determining the needed coordinate points are also detailed.

With the α, β and γ now defined, for simplification of the multi-probe method, α will be assumed to be the zero angle, or reference angular location, like in the simulation and literature [1]. The actual β value used in the research will be the planar angular location of arm two contact point, referenced from arm one, α, and the actual γ value used in the research will be the planar angular location of arm three contact, referenced from arm one, α, as well. Using β and γ, as well as measurement signals two and three, the form error of the component can be determined and when the component form error is determined, the spindle error motions can be determined for both the x and y directions.

From the measuring instrument design, described in detail in a later section, the planar angle locations, at the measuring instruments arm end, may not move in a purely radial direction relative to the component as it rotates. This is important because the multi-probe method needs the angular displacement from the measuring instrument, to be converted to linear displacement at the arm end. This can be done with the arc-length formula, however, the actual motion the arm end moves, may not be radial and needs to be projected into the radial direction. This will be described in more detail in a later section.

CHAPTER 3: SIZE METROLOGY

3.1. Diameter Determination

As mentioned earlier, simple mechanical tools are often used to take in-process diameters measurements. As an example, a caliper provides a two-point measurement of a nominally circular shape as a distance which represents the diameter of the circular shape. However, if the component is odd-lobed shaped, then the two-point measurement system could potentially measure a high-high, low-low or high-low spot, which will produce three different measurement results. In this research, the circle is defined using three, non-collinear, points which geometrically uniquely defines a circle. While the issue of varying measurement results due to component non-circularity will still exist, the method developed here is capable of nearly automated operation over a wide range of diameters without the need for a calibrated artifact to master the measuring instrument, and with reduced reliance on operator skill.

Given three unique points on a circle, the diameter of the circle in question can be determined with a geometrical model. The three points on the circle create a unique triangle and the geometrical model states that if the area of the triangle, its semi-perimeter and side lengths, are known, a circumcircle is created and the diameter of the circumcircle can be computed by the given parameters [12]. FIGURE 20 shows a circle with three unique points, which is used to determine the area of the triangle, semi-perimeter, side lengths and thus its diameter.
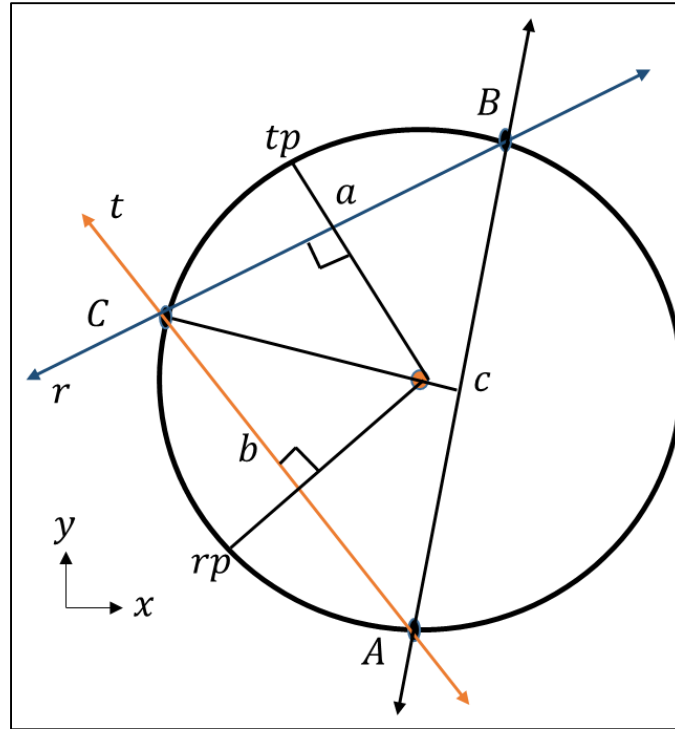
FIGURE 20: Circle used for diameter and angle determinations of circular component

To determine the above parameters, an algebraic proof using Pythagoreans theorem is used [12]. Using the triangle portion from FIGURE 20 and drawing a line from point C and cutting the base into two sections, Pythagoreans theorem can now be used for determining the parameters of area, semi-perimeter, side lengths and diameter. FIGURE 21 shows the triangle portion from FIGURE 20 with additional variables d and h. The triangle is rotated for clarity.
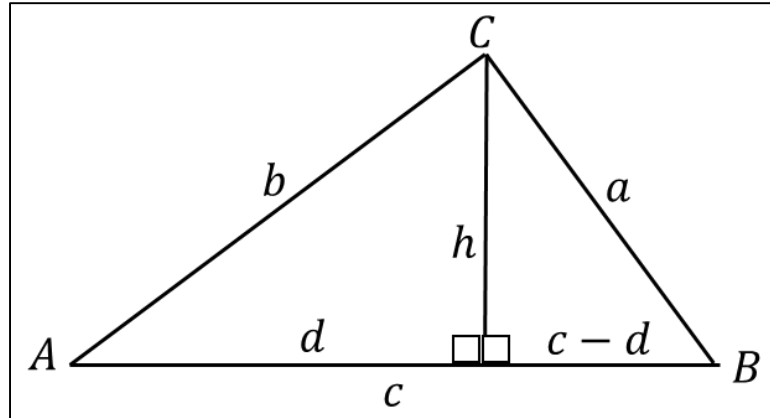
FIGURE 21: Triangle with sides A, B, C and sections for Pythagoreans Theorem

From FIGURE 21, using Pythagoreans theorem for both triangles created by the bisection of h, the area of the triangle can be determined as follows:

$$b^2 = h^2 + d^2 \tag{34}$$

$$a^2 = h^2 + (c-d)^2 \tag{35}$$

Now subtracting a^2 from b^2 , to eliminate h, produces:

$$a^2 - b^2 = c^2 - 2cd \tag{36}$$

Solving for d

$$d = \frac{-a^2 + b^2 + c^2}{2c} \tag{37}$$

Now with d expressed and using Eq. (34) to solve for h, the height of the triangle can be found. Some algebraic steps are not included to reduce clutter.

$$h^2 = b^2 - d^2 = \left(\frac{2bc}{2c}\right)^2 - \left(\frac{-a^2+b^2+c^2}{2c}\right)^2$$

$$= \frac{(2bc - a^2 + b^2 + c^2)(2bc + a^2 - b^2 - c^2)}{4c^2}$$

$$= \frac{(b + c - a)(b + c + a)(a + b - c)(a - b +)}{4c^2} \tag{38}$$

$$= \frac{4s(s - a)(s - b)(s - c)}{c^2}$$

$$h = \sqrt{\frac{4s(s - a)(s - b)(s - c)}{c^2}}$$

Where $s = \frac{(a+b+c)}{2}$, is the semi-perimeter of the triangle, and now applying the formula for the area of a triangle, which uses the height of the triangle, h, and c for its base:

$$A = \frac{ch}{2}$$

$$= \sqrt{\frac{c^2}{4} \cdot \frac{4s(s - a)(s - b)(s - c)}{c^2}} \tag{39}$$

$$= \sqrt{s(s - a)(s - b)(s - c)}$$

Since all triangles are cyclic in nature and are classified as polygons, a circumscribed circle can be fitted to the triangle points, more specifically a unique minimum bounding circle. With the area of the triangle expressed, the diameter from the triangle can be determined with the following equation.

$$Diameter = \frac{(abc)}{2A} \tag{40}$$

To determine the side lengths of the triangle, the x and y, coordinates of the points $A(x_1, y_1)$, $B(x_2, y_2)$ and $C(x_3, y_3)$ from FIGURE 20, are needed. These x and y coordinates will be determined from the measuring instrument's kinematic model, which will described in Chapter 4. The side lengths of the triangle are as follows:

$$a = \sqrt{(x_3 - x_1)^2 + (y_3 - y_1)^2} \tag{41}$$

$$b = \sqrt{(x_2 - x_1)^2 + (y_2 - y_1)^2} \tag{42}$$

$$c = \sqrt{(x_2 - x_3)^2 + (y_2 - y_3)^2} \tag{43}$$

Where $a = \overline{AC}$, $b = \overline{AB}$ and $c = \overline{CB}$.

The above formulas will be the basis of the software for determining the diameter of the component under test. To prove that the diameter measurement method is capable of reconstructing the diameter, simulations with synthetic encoder data (w/noise) is done.

3.1.2. Simulation of Diameter Measurement Method

A diameter of 457.2 mm (18″) is chosen to simulate. This diameter is chosen because it is typical diameter size in a large-scale manufacturing setting. When the measuring instrument engages with the component, the measuring instrument's absolute encoders, produce the angular position for each arm, relative to a reference index on the encoders scale. These angular displacements, as well as their angular offsets from the measuring instrument's global coordinates system relative to the reference index on the scale, are then used to calculate the x and y coordinates, of each arm's contact point on the surface of the component. From the x and y coordinates, Eq. (41), Eq. (42) and Eq. (43) are then used to determine the sides of the triangle and thus the semi-perimeter of the triangle, s. With the sides of the triangle and semi-perimeter found, the area of the triangle can be determined using Eq. (39). With the area and semi-perimeter found, the diameter of the component can be estimated using Eq. (40).

The noise level in the data is assumed to be approximately 2.5 $arc - \sec$ (0.00069°), which is the stated bi-directional accuracy of the encoder modules in the measuring instrument. Results for the simulation can be seen in TABLE 1.

TABLE 1: Simulation results for diameter measurements.

Noise = 2.5 Arc-Sec	inch	mm
Simulated	18	457.2
Reconstructed	18.00018	457.2048
Difference	0.00018	0.0048

A typical diameter this size, could have tolerances in the range of $\pm 0.0508 \, mm$ ($\pm 0.002''$), so from TABLE 1, this method has good potential for reconstructing diameter measurements using the previously described method.

3.2. Center Position Determination

In order to determine the center position of the component, in the measuring instrument coordinates, the x and y coordinates from the three contact point must be expressed, which will be determined from the measuring instruments kinematic model. From FIGURE 20, the three points are labeled as $A(x_1, y_1), B(x_2, y_2)$ and $C(x_3, y_3)$ and also shows lines t and r, which connect points B and C and points A and B, respectively. The center of the circle, in measuring instrument coordinates, lies at the intersection of the perpendicular bisector of these lines, the orange dot. The slope for lines t and r can be expressed as:

$$m_r = \frac{y_3 - y_2}{x_3 - x_2} = \frac{y_r - y_2}{x - x_2} \tag{44}$$

$$m_t = \frac{y_3 - y_1}{x_3 - x_1} = \frac{y_t - y_1}{x - x_1} \tag{45}$$

Where m_r is the slope of line r and m_t is the slope of line t. Now with the slopes expressed, the equations of each line can be determined.

$$y_r - y_2 = m_r(x - x_2)$$
$$y_r = m_r(x - x_2) + y_2 \tag{46}$$

$$y_t - y_1 = m_t(x - x_1)$$
$$y_t = m_t(x - x_1) + y_1 \tag{47}$$

Geometrically, the center of the circle lies on the lines that pass through the mid points of chords $\overline{CB}$ and $\overline{AC}$ and are perpendicular to each chord. Lines that are perpendicular have negative reciprocal slopes. These new line can be called rp and tp to indicate their perpendicular connections to lines r and t, respectively. The midpoint equations are:

$$on\ line\ r, segment\ \overline{CB},\ midpoint$$

$$\left(\frac{x_3 + x_2}{2}, \frac{y_3 + y_2}{2}\right) \tag{48}$$

$$on\ line\ t, segment\ \overline{AC},\ midpoint$$

$$\left(\frac{x_3 + x_1}{2}, \frac{y_3 + y_1}{2}\right) \tag{49}$$

Now Eq. (46) and Eq. (47) of the lines are expressed as:

$$y_{rp} - \frac{y_3 + y_2}{2} = -\frac{1}{m_r}\left(x - \frac{x_3 + x_2}{2}\right)$$

$$(50)$$

$$y_{rp} = -\frac{1}{m_r}\left(x - \frac{x_3 + x_2}{2}\right) + \frac{y_3 + y_2}{2}$$

$$y_{tp} - \frac{y_3 + y_1}{2} = -\frac{1}{m_t}\left(x - \frac{x_3 + x_1}{2}\right)$$

$$(51)$$

$$y_{tp} = -\frac{1}{m_t}\left(x - \frac{x_3 + x_1}{2}\right) + \frac{y_3 + y_1}{2}$$

These two line intersect at the center of the circle, $(y_{rp} = y_{tp})$. Setting Eq. (50) and Eq. (51) equal, and solving for x, will produce x center point, in measuring instrument coordinates. This is shown below.

$$-\frac{1}{m_r}\left(x - \frac{x_3 + x_2}{2}\right) + \frac{y_3 + y_2}{2} = -\frac{1}{m_t}\left(x - \frac{x_3 + x_1}{2}\right) + \frac{y_3 + y_1}{2} \qquad (52)$$

$$X_{center} = \frac{m_r m_t(y_3 - y_2) + m_r(x_3 + x_1) - m_t(x_3 + x_2)}{2(m_r - m_t)} \qquad (53)$$

Where X_{center} is equal to x in Eq. (52). Thus when X_{center} is determined, and substituted into Eq. (50), Y_{center} is then determined.

$$Y_{center} = -\frac{1}{m_r}\left(X_{center} - \frac{x_3 + x_2}{2}\right) + \frac{y_3 + y_2}{2} \qquad (54)$$

Eq. (54) will not be reduced further. These equations are used for the direction cosines described in section 2.2 and the scale projections in section 5.4.1.

For both the diameter and center position algorithms, the actual x_1, x_2, x_3 and y_1, y_2, y_3 coordinate points are found from the kinematic model for the measuring instrument. The measuring instrument concept and design will be detailed in chapter 4 of the research.

CHAPTER 4: COORDINATE MEASUREMENT SYSTEM DESIGN

4.1. Measuring Instrument Concept

Typical in-process measurements for circular component diameter and form error is done with very basic methods such as friction-rollers, caliper-type instruments and dial indicators [2] [28] [51]. These methods inherently have error and have the potential to produce erroneous results. Another issue, is that these processes are all individualized with setup, fixturing and data collection. This increases time in the entire manufacturing process. The in-process measuring instrument developed in this research will incorporate both form and size measurements into a single device, which will be interfaced with a lathe's turret.

The measuring of the circular component is done by three pivoting arms attached to the measuring instrument's body, which uses high-resolution angular encoders to read the angular displacement of the arms. These encoder angular displacements are used for calculating the circular component's diameter and form error. Section 4.2 gives full detail of the entire measuring instrument design.

The measuring instrument has gone through two full designs for prototyping. The first measuring instrument will be described, but not in full detail, just the major points of the design. The second version of the measuring instrument improved all the short comings of the first design. The second version of the measuring instrument will be described in full detail since it is the system that produced all the results in this research.

4.2. Measurement Instrument Design

The measuring instrument developed in this research utilizes three high-resolution angular encoder modules with integrated high-precision bearings to measure the angular displacement of the three arms that contact the circular component being measured. The angular displacements are converted into coordinates of the contact points by using the physical dimensions of the measuring instrument, via a kinematic model. The kinematic model contains unknown parameters that are defined by the actual dimensions of the as-built measuring instrument. Once the measuring instrument is constructed, the as-built values of these parameters must be measured on a high-precision CMM. From the CMM measured kinematic model, these measured values are used in the software to calculate the diameter and the form error of the components under test.

4.2.1. Kinematic Parameters

Kinematics is the study of classical mechanics which describes the motion of points, bodies (objects) and systems of bodies without considering the causes of motion. It is also referred to as the study of the geometry of motion [13]. FIGURE 22 shows the kinematic parameters of the measuring instrument.
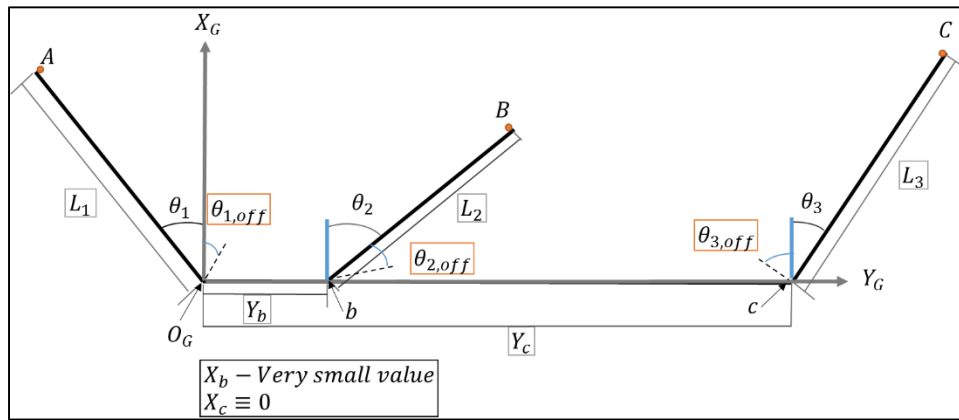
FIGURE 22: Kinematic parameters of the measuring instrument

For the measuring instrument, there will be nine kinematic parameters. Six of the parameters will have the unit of length and three will be units of angle. The length parameters are the lengths of each arm and the x and y coordinates of arm pivot points b and c relative to the measuring instrument origin, O_G, at the pivot point of arm one. X_c is defined as zero because the y axis of the measuring instrument is defined to pass through the pivot points of arms one and three. X_b is nominally zero but is expected to have a very small offset from the y axis in the as-built measuring instrument. The three other parameters are the offsets of the encoder module scales reference point, relative to the measuring instruments x axis. The angular encoder modules absolute position reference point is set in the electronics of the module. The angular offsets are from the mounting position of the angular encoder modules in the measuring instrument's body. Thus the offset from the angular encoder modules reference scale and the measuring instruments coordinate's x axis is needed to convert encoder module readings into absolute arm angles relative to the measuring instrument's coordinate system origin.

L_1, L_2, L_3 are defined as the arm lengths of the measuring instrument, Y_b, Y_c, X_b are defined as the x and y coordinates of arms' two and three pivot points from the origin of the measuring instrument, $\Delta\theta_1, \Delta\theta_2, \Delta\theta_3$ are the angular displacements from the reference of the encoder modules and $\theta_{1,off}, \theta_{2,off}, \theta_{3,off}$ are the offsets from mounting of the encoder modules to the measuring instrument origin. Absolute angular displacement is defined as $\theta_i = \Delta\theta_i + \theta_{i,off}$, where the actual data from the encoders is $\Delta\theta_i$'s, which are angular displacements from the reference mark on the angular encoder modules scale. These nine parameters will be measured on a CMM for calculating the diameter and form error of the components.

4.2.2. Kinematic Parameters Coordinates

For the size and center position of the circular component be measured, the x and y coordinates of the contact points, A, B and C on FIGURE 22, need to be determined from the kinematic parameters or model. The encoders read angular displacement data, so the unit of length must be introduced from the kinematic parameters. It was first intended to use an identification process or routine, to determine the kinematic parameters of the measuring instrument. However, the previous version of the measuring instrument did not produce correct approximations of the kinematic parameters. This was due to poor kinematic coupling between a reference standard and the arms themselves. So in this section, only the coordinate points for each arm, from the kinematic model will be derived and these equations will be used for calculating the diameter and center position values.

When the kinematic parameters are measured on the CMM, the x and y coordinates of point A, B and C, can be determined relative to the measuring instrument coordinate system using the angular encoder modules position. The coordinate points from the kinematic model are expressed below.

$$x_{A,INST} = L_{1,CMM} cos(\Delta\theta_1 + \theta_{1off,CMM}) \tag{55}$$

$$y_{A,INST} = L_{1,CMM} sin(\Delta\theta_1 + \theta_{1off,CMM}) \tag{56}$$

$$x_{B,INST} = X_b + L_{2,CMM} cos(\Delta\theta_2 + \theta_{2off,CMM}) \tag{57}$$

$$y_{B,INST} = Y_b + L_{2,CMM} sin(\Delta\theta_2 + \theta_{2off,CMM}) \tag{58}$$

$$x_{C,INST} = X_c + L_{3,CMM} cos(\Delta\theta_3 + \theta_{3off,CMM}) \tag{59}$$

$$y_{C,INST} = Y_C + L_{3,CMM} sin(\Delta\theta_3 + \theta_{3off,CMM}) \tag{60}$$

These coordinates are the x and y values used for calculating the diameter and center position of the component, as described in sections 3.1 and 3.2.

4.2.3. Values of Kinematic Parameters of Measuring Instrument

The optimal values of the kinematic parameters or model were determined though an optimization routine using a constrained minimization technique. This process was created by a simulation of the measuring process to create synthetic measurement data. This was followed by a Monte Carlo simulation where the synthetic data is corrupted by random noise to produce statistics of expected variations in the measurement result. Finally, a constrained minimization optimization routine was created with the Monte Carlo simulation to select the physical dimensions of the instrument that would lead to the best overall measurement performance. This optimization produced a vector of possible solutions for the optimal kinematic parameters of the measuring instrument. However, it was found that the physical dimensions (kinematic parameters) could vary significantly without dramatically affecting the measurement uncertainty, allowing the design to be tailored to enable measurement of a wide range of component diameters.

The nominal values for the final design were chosen to enhance its ability to measure a significant variety of diameters ranging from $101.6\ mm\ -\ 1778\ mm$ (4" - 70"). The values also were chosen so that the measuring system would not become bulky and cause ergonomic issues.

TABLE 2 shows the kinematic parameters chosen as the nominal values for the second version of the measuring instrument. All chosen kinematic parameters values are of the unit length. The angular offset kinematic parameters are not design values, but depend on the physical construction of the encoder units and their orientation when installed in the measuring instrument.

TABLE 2: Kinematic parameter design values for measuring instrument

KP's	in	mm
L_1	14.4125	366.0775
L_2	11.6925	296.9895
L_3	14.4375	366.7125
X_B	0.0000	0.0000
Y_B	5.0000	127.0000
X_C	0.0000	0.0000
Y_C	21.7000	551.1800

Now that all the kinematic parameters dimensions have been determined, an actual physical prototype of the measuring instrument can be designed and built. The measuring instrument design will be fully detailed in section 4.2.4. The first version of the measuring instrument will be briefly discussed along with its shortcomings. Then the second measuring instrument will be discussed with the different modifications.

4.2.4.   First Physical Design of Measuring Instrument

The prototype measuring instrument went through two different designs. The first design of the measuring instrument was designed using optimized kinematic parameters, which were determined through an optimization routine of both the measuring process of the measuring instrument and an identification routine that was intended to identify the kinematic parameters of the measuring instrument during use in an actual manufacturing process.

The first design can be seen in FIGURE 23 as a CAD model that went through numerous iterations in design for the measuring instrument's body, arms, inner assemblies of each arm, etc.
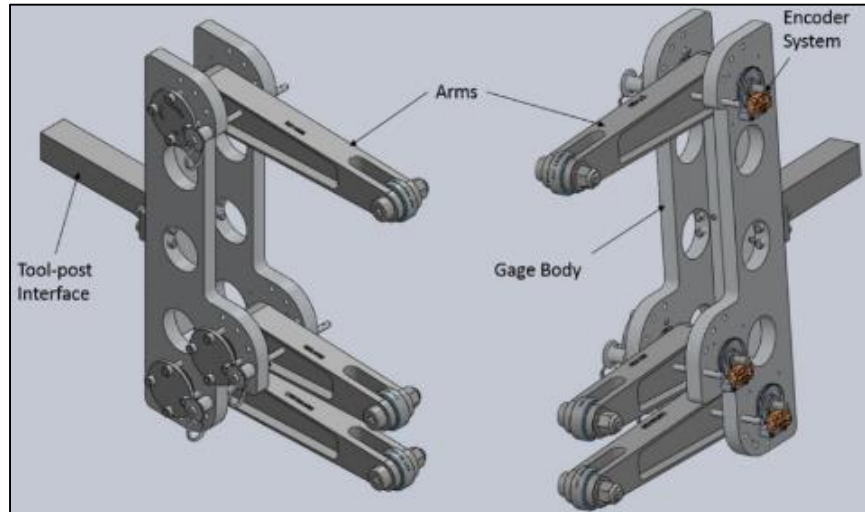
FIGURE 23: CAD model of first design of measuring instrument.

FIGURE 24 is the exploded view of the first design of the measuring instruments' sub-assemblies.
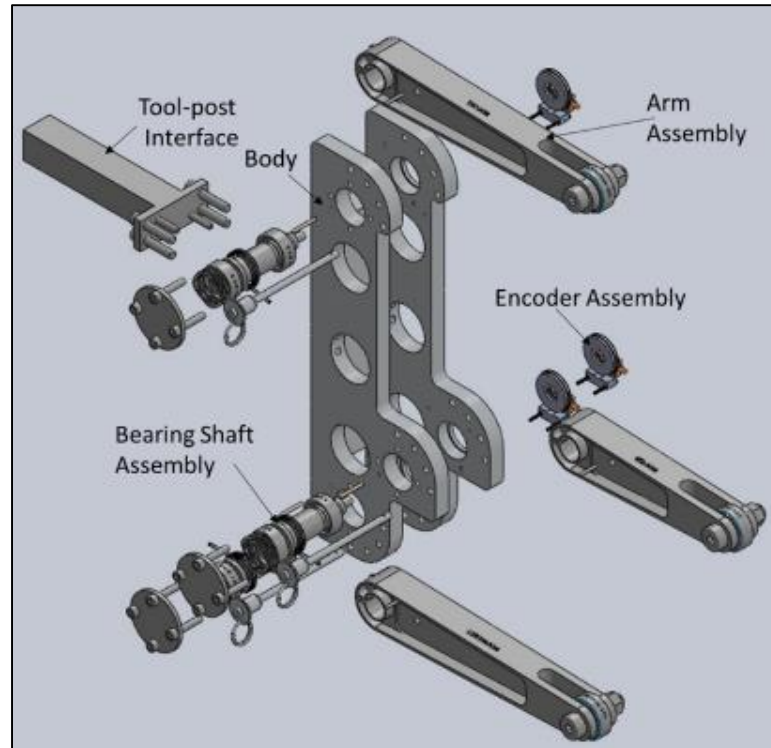
FIGURE 24: First design measuring instrument sub-assemblies

The first design of the measuring instruments body is a monolithic piece of aluminum, designed to ensure concentricity of the holes for the bearing shaft assemblies. The body cross-section, from the top view is U-shaped to decrease the weight and to allow all arms to have a larger range of motion. The three larger holes in the middle of the body are for the purpose of reducing weight.

This first design of the measuring instrument has kinematic parameters for X_B, Y_B and X_C that are located from the measuring instruments' origin to their respective positions based on optimized values. FIGURE 25 points out some details of the body design.
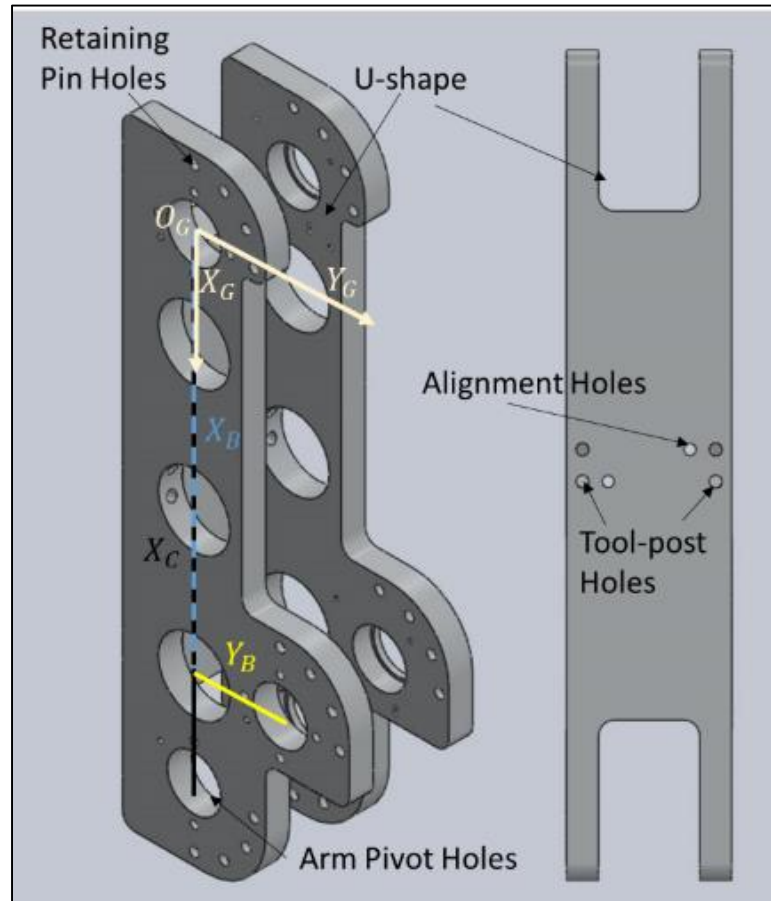
FIGURE 25: First design of measuring instrument body (w/ kinematic parameters).

The arms are an I-beam design, to reduce weight but maintain stiffness. FIGURE 26 shows the design for all three arms.
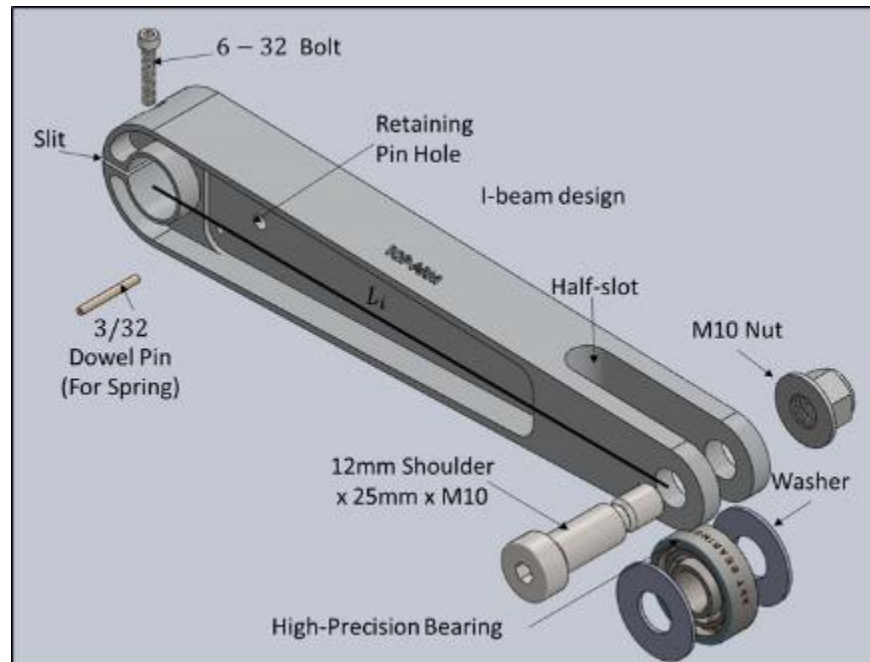
FIGURE 26: Arm design for first design of measuring instrument (w/kinematic parameter)

The pivot point of each arm is designed to have a split clamp on the end, so it can slip onto the shaft it pivots about and is secured with a $6 - 32$ bolt. There is a $3/32$ dowel pin, lightly press-fit into the arm and is where the torsion spring will be attached to the arm. The other end of the torsion spring will be attached to another $3/32$ dowel pin mounted on the measuring instruments body. The torsional springs preload the arms to ensure that the contactor at the end of the arms will be lightly forced against the surface of the circular component to be measured.

Each arm has a hole for a retaining pin to go through, so that the arm can be held in a fixed position. At the end of each arm is a high-precision bearing to contact the circular component that is being measured and is held in place by a precision shoulder screw. The original purpose of these bearings was to act as a roller-follower on the surface of the circular component, however, upon assembly, the slop in the bearing was too high. A change to a sliding contact was made. The bearings are hardened steel, so they should not be subject to a high-wear rate when sliding along the surface of the circular component. FIGURE 26 shows the assembly of each arm.

The bearing shaft assembly for each arm pivot is a combination of a shaft, two high-precision bearings, three custom made washers and a wave spring, used for preloading the bearings. The encoder disk is mounted on the right hand end of the shaft. FIGURE 27 shows the bearing shaft assembly for each arm.
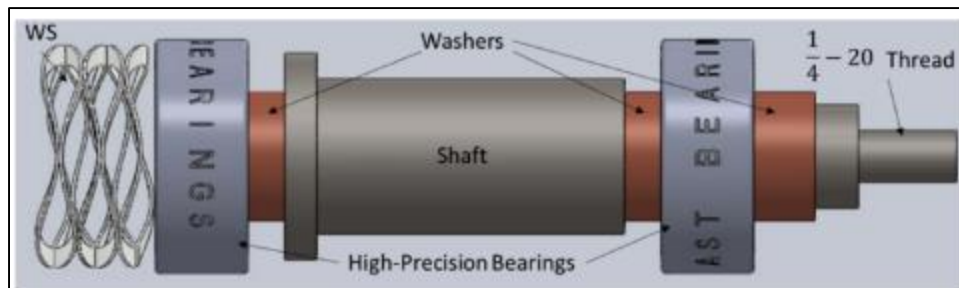
FIGURE 27: Bearing shaft assembly for each arm, first measuring instrument design

FIGURE 28 shows a section view of each arm assembled with the measuring instrument body and the force path of the bearings when preloaded with a plate and bolts.
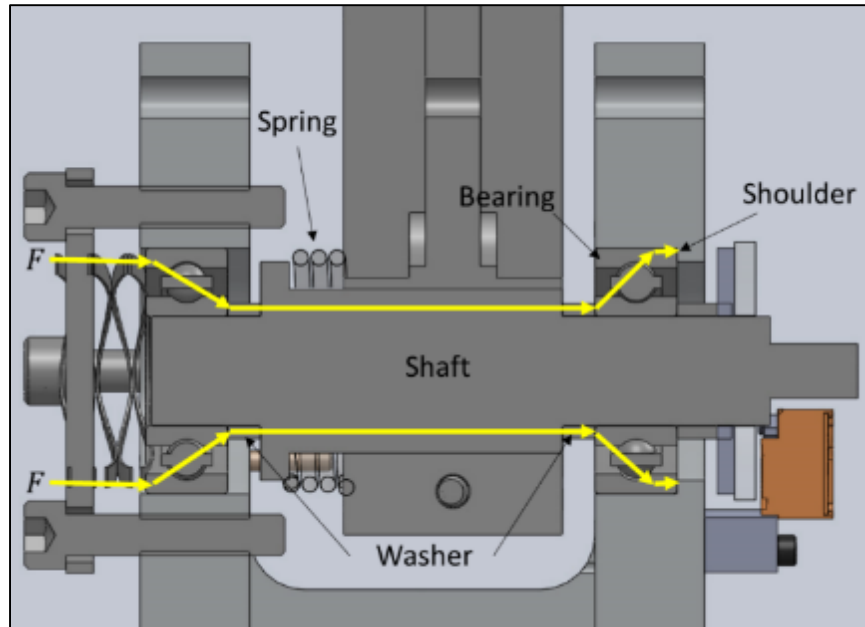
FIGURE 28: Section view of each arm assembly with body and force path for preloading bearing, first measuring instrument design

The encoder system used for the first measuring instrument are Renishaw® ATOM™ miniature angular encoders. The ATOM system is a non-contact optical incremental encoder system that combines a compact encoder size with exceptional metrology performances and high durability for most shop-floor environments.

The encoder systems used for the first design of the measuring instrument are ATOM $0.020\ mm$ (0.00079") pitch read-heads, with a TONIC interface that interpolates up to 4000 times the resolution. The glass scales is of a $30\ mm$ (1.18") diameter, with a single reference (index) mark, with a line count of 4096 per revolution, which converts to an interpolated resolution of approximately 16.4 million counts per revolution, to get more accurate data. The interpolated resolution is thus converted to $2.2x10^{-5}°$ $(0.079\ arc-sec)$. The output of the encoder is a digital signal or an A QUAD B square wave. All specifications are per manufacturer.

The difference between the absolute and incremental encoders is that when the encoder system is powered off, the absolute encoder stores the systems reference or "home" position, while incremental encoders do not. Thus when the system is off and restarted, the incremental encoder must be referenced, to a reference mark, every time. The second design of the measuring instrument uses absolute encoders with integrated high-precision bearings to create a module. These encoder modules will be discussed fully in the next section.

The encoder system assembly for each arm consists of the read-head of the encoder, glass scale, a couple of nylon washers and custom design mounts for the read-head to attach to the measuring instrument body. FIGURE 29 shows the encoder system assembly.
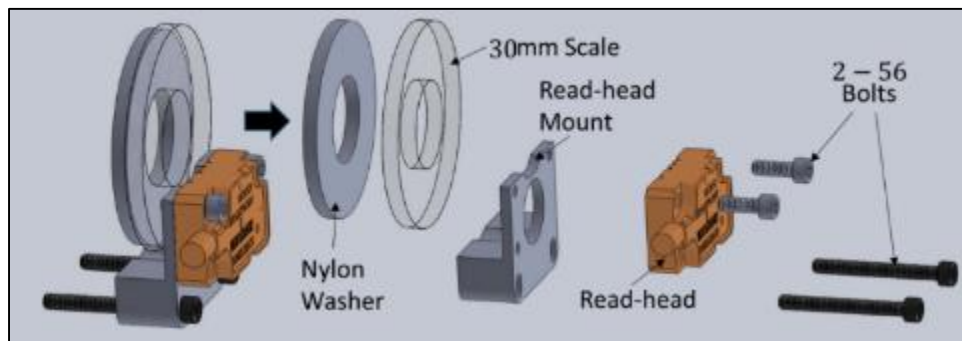
FIGURE 29: Encoder system assembly for first design of measuring instrument

The last subassembly in the first design of the measuring instrument is the tool-post interface with the body. The tool-post adapter is a $25.4\ mm\ x\ 25.4\ mm\ x\ 127\ mm$ (1" x 1" x 5") T-shape part. It is made of steel and connects the measuring instrument to the lathe. The tool-post interface is connected with two 3/32 dowel pins, which are used as locating pins for aligning the tool-post to the measuring instrument's body. Four $¼ - 20$ bolts are used to secure the tool-post adapter to the measuring instrument's body. FIGURE 30 shows the tool-post interface assembly.
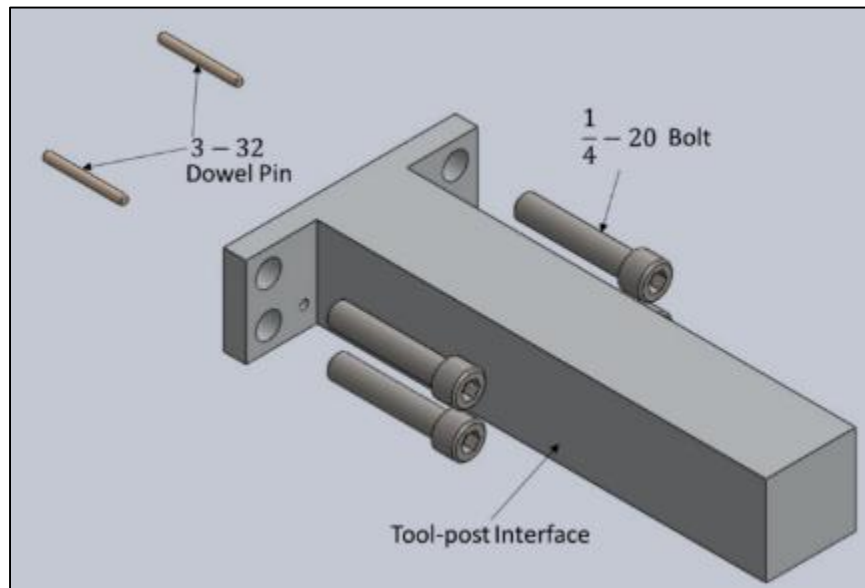
FIGURE 30: Tool-post interface assembly for first design of measuring instrument

From the CAD model of the first design of the measuring instrument, a prototype of the system is fabricated and is shown in FIGURE 31.
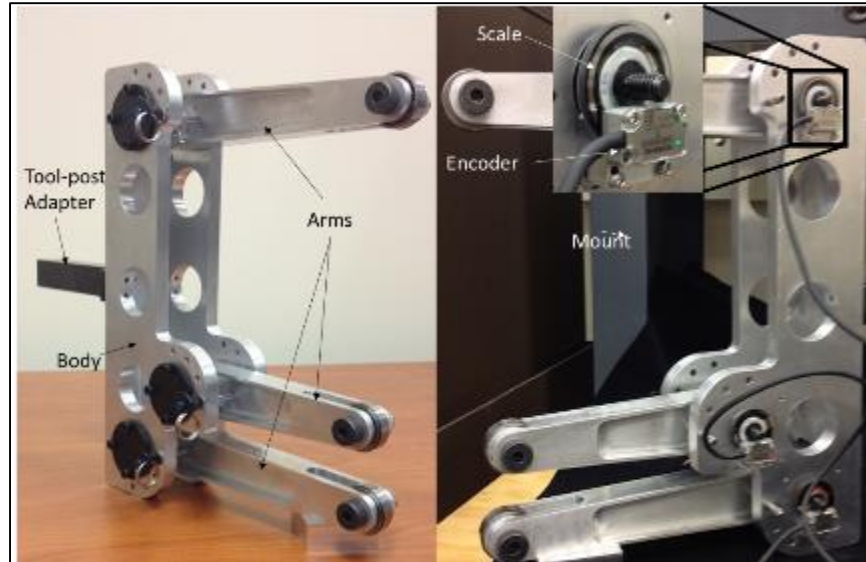
FIGURE 31: First design of measuring instrument prototype

With the first design, it was thought that the system can be initialized with a reference standard to identify the kinematic parameters of the measuring instrument. The reference standards that would be used for the initialization routine are made from a single piece of coated steel, have a V-shape at each end with two 1/4″ steel dowel pins between the V-shapes that contact the surface of the bearings on the arm ends. The dowel pins each sit in a semi-circular groove and the pins are used to kinematically contact the surface of the bearing as the arms are motioned back and forth. To maintain contact with the bearing surface, a magnet is placed at the bottom of the V-shape, seated in a drilled hole. The magnet is held in place with a set screw on the side of the body of the reference standard. FIGURE 32 shows the reference standards.

FIGURE 32: Reference length standards for identification routine, first design of measuring instrument

After assembly of the prototype of the first design of the measuring instrument was done, testing of the instrument could be done. The measuring instrument was first measured on a high-precision CMM to obtain the as-built kinematic parameter values. After measuring the kinematic parameters, it was noticed that the angular offsets for the encoders were not repeating well. This gave an indication that when the incremental encoders were being initialized over the z-index reference point, the reference point was not repeating to the same place. The next test was the identification routine with the reference standards, which showed that the encoder values were not following the same return path when motioned back and forth. FIGURE 33 shows the back and forth motion of arms one and three and the non-repeatability of the four-bar linkage created by the measuring instrument and the reference standards.
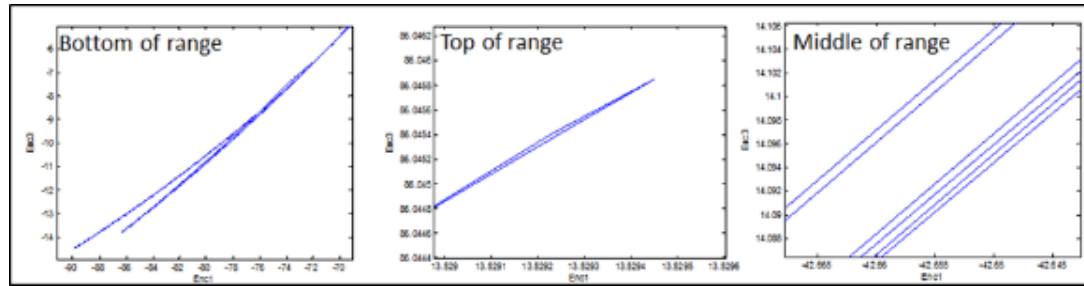
FIGURE 33: Four-bar motion of the first design of measuring instrument (arms one and three)

The reasons for the lack of repeatability are most likely due to improper kinematic contact between the ends of the reference rods and the arm contactor cylinders, but may also be due to reversal errors, too much friction in the bearing shaft assemblies or too much slop from the bearings. This test indicates that the measuring instrument will have too much error in the assembly to provide an accurate result in the diameter. Some initial test of the first design of the measuring instrument on $508\ mm$ ($20"$) component show that, even with the CMM measured kinematic parameters, the measuring instrument measures the diameter of the component by approximately $1\ mm$ ($0.0393"$) difference from the CMM measured diameter of the component. This is unacceptable and indicated that a new design of the measuring instrument is needed.

4.2.5. Second Physical Design of Measuring Instrument

The new design and current prototype of the measuring instrument corrects for all the known short-comings and issues with the first design of the measuring instrument.

The first measuring instrument was designed to using incremental angular encoders. These encoders lose their 'home' or reference position when the system is turned off. So the encoders had to be initialized over a reference point every time the system was initiated. This led to repeatability issues with the reference point, in which the encoders were referenced to a different home position every time the system initiated. This was confirmed when the angular offsets of the first measuring instrument were measured on the CMM and the values did not repeat. The new measuring instrument uses absolute encoders and the reference position is to the same place every time the system is initiated and shut off. Furthermore, the new system's encoders are modules with high-precision bearings integrated into the system, thus eliminating the need to design and construct high-precision rotary joints and making it easier to integrate them into the measuring instrument.

The next issue for correcting was the type of contact the measuring instrument would make on the surface of the component. The first design of the measuring instrument used high-precision cylindrical bearings as arm end contact points; but it was realized that any non-parallelism between the contactor surface and the shaft being measured would lead to improper contact with the surface of the component. This also was an issue for the reference standards created for the first measuring system, since the reference standards had two dowel pins to ride on the contactor, resulting in an over-constrained contact. This was solved in the new design by using spherical contactors to ensure exact kinematic constraint.

A CAD model of the new design can be seen in FIGURE 34.
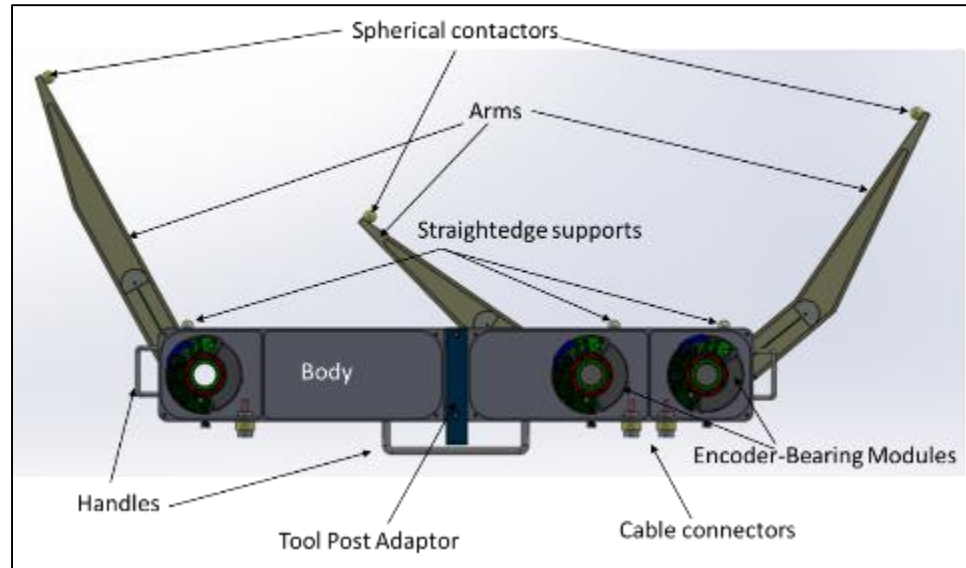
FIGURE 34: CAD model of new measuring instrument design

The new measuring instrument still uses three arms that pivot about the body, and each arm has a spherical contact on the end of the arm to make contact with the component surface to be measured. The body is made of a monolithic piece of steel, which is coated for wear-resistance and a tool-post adaptor is bolted on to interface with a lathe. The body has milled pockets to house the angular encoder modules and covers are bolted onto the back of the body to protect the modules from debris. There are three cable connectors, one for each module, and three handles to carry the measuring instrument.

FIGURE 35 shows the major components of the measuring systems design and assembly.
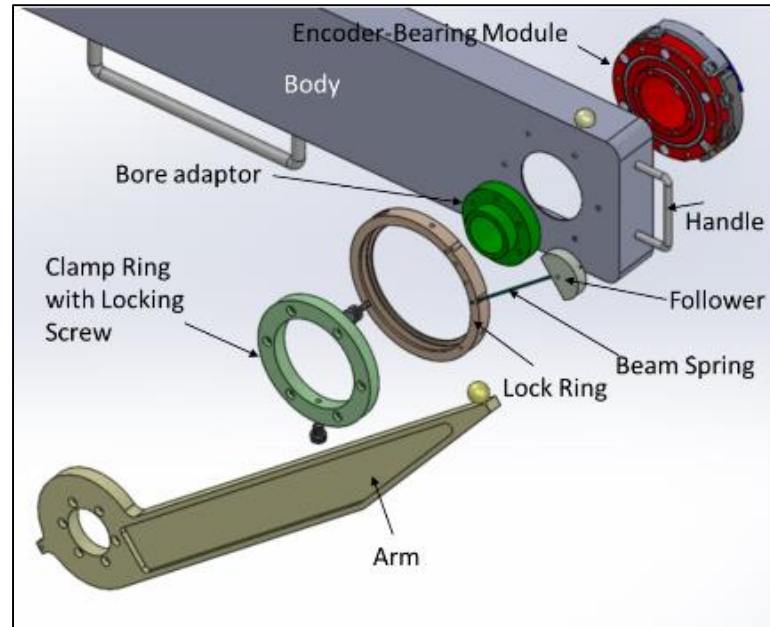
FIGURE 35: Major components of the new measuring system

From FIGURE 35, the new measuring instrument consists of a very different arm assembly than the first measuring instrument design. Each arm assembly consists of an arm with a spherical contact, a clamp ring with a locking screw to lock the arm in place, a lock ring with a beam spring and follower, so the arm can be spring loaded into the component to keep contact, and a bore adapter used to connect the arm, clamp ring and lock ring to the body and encoder module.

Each arm is assembled in the same manner. FIGURE 36 shows step one of assembly.
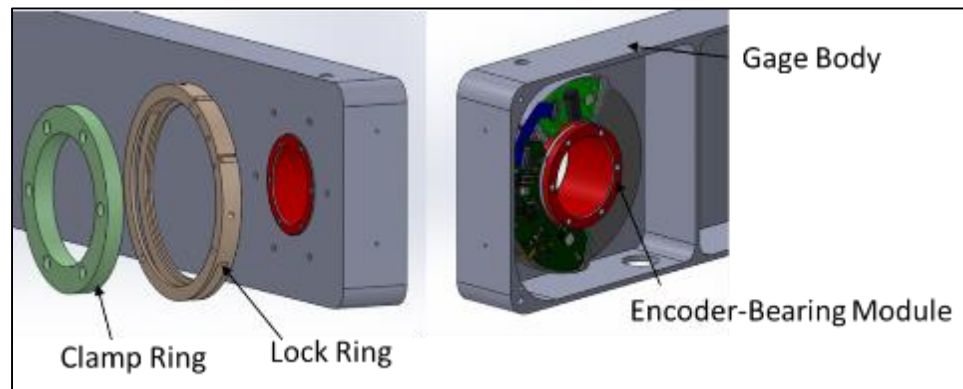
FIGURE 36: Arm assembly step one

From FIGURE 36, the angular encoder module is placed in the inside of the body. On the outside of the body, the lock ring and clamp ring are bolted to the body through a six-hole bolt pattern, which can be seen in FIGURE 36. The clamp ring is placed inside of the lock ring, which is where a clamp screw is set to lock the clamp ring to the lock ring to create tension on the beam spring connected to the lock ring. FIGURE 37 shows how the lock ring and clamp ring work.

Lock Ring – *captured by lip on clamp ring but free to rotate if clamp screw disengaged*

Clamp Ring with clamp screw *Rigidly attached to encoder module and gage body*
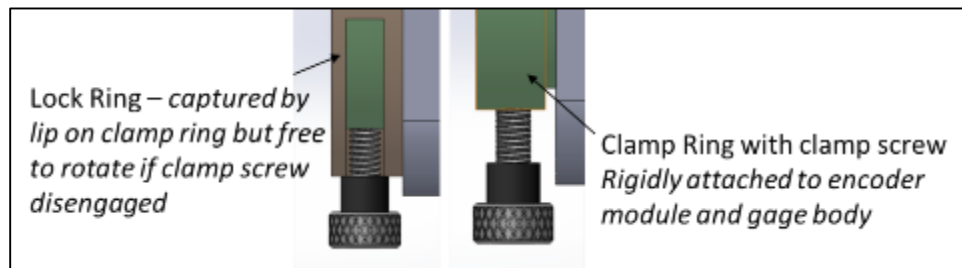
FIGURE 37: Lock ring and clamp ring (w/screw)

FIGURE 38 shows the rest of the arm assembly.

Arm

Adaptor to bearing inner race (Bore)

Spring and follower – *anchored to lock ring*

Spring follower engaged with arm

Lock Ring - *free to rotate with arm if clamp screw disengaged*
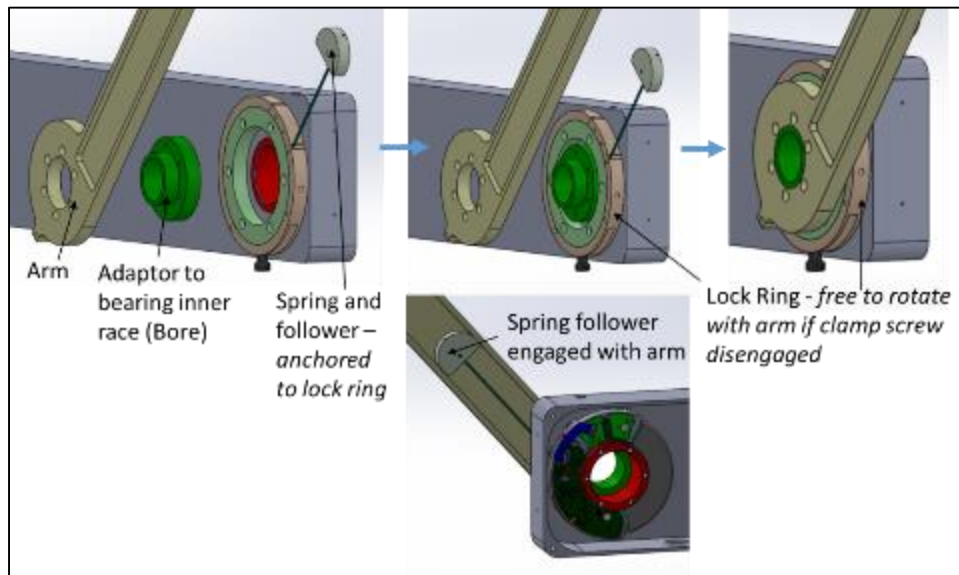
FIGURE 38: Arm assembly step two

Once the clamp ring and lock ring are in place, the bore adapter is bolted in to the angular encoder module through a six-hole bolt pattern. The angular encoder module has a bolt pattern on the inner race. The arm is then bolted onto the bore adapter through its six-hole bolt pattern. The beam spring is connected to the lock ring on one end and then connected to a follower on the other end, which is engaged with the arm, shown in FIGURE 38.

FIGURE 39 shows how each arm assembly operates.
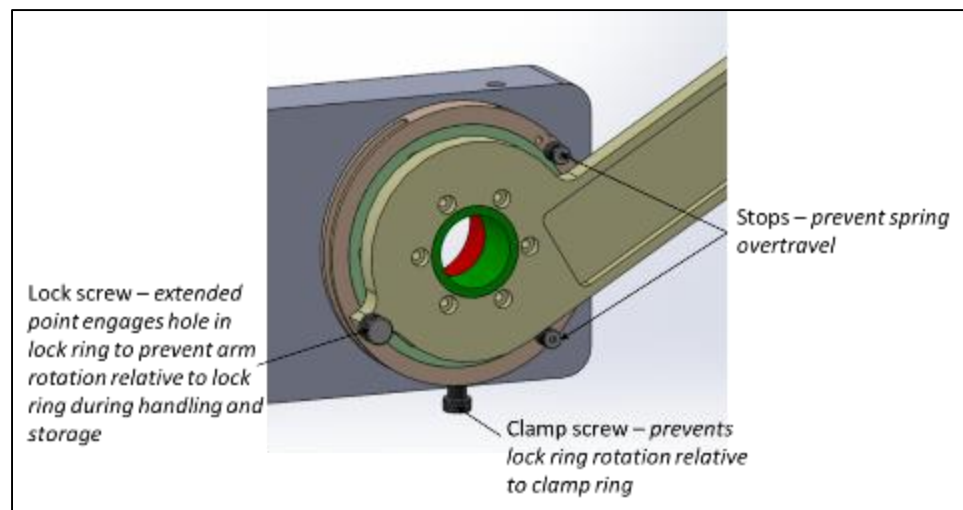
FIGURE 39: Arm operation

From FIGURE 39, when the lock ring is turned, and the arm is in contact with the surface of the component, the beam spring is tensioned and adds a force to the arm, which is locked with the clamp screw, to ensure the arm stays in contact with the surface of the component. There are two mechanical stops located on the lock ring, to prevent the springs from overtravel, which could lead to yielding of the spring. There is also a lock screw, which is threaded through the arm and the lock ring. This lock screw prevents the arm rotating relative to the lock ring, during handling and storage, so that the arms are not damaged.

The encoder modules used in this measuring instrument are Heidenhain MRP 5010 absolute encoder modules. The encoder modules are a combination of an absolute angular encoder and a high-precision bearing that are pre-assembled and adjusted. The modules are characterized by their high degree of measuring accuracy, high-resolution, high-repeatability and a low starting torque which permits a very smooth motion. The rolling bearings are adapted to the requirements of high-precision rotary axes. Per manufacturer specifications, the radial/axial guideways of the bearings have an accuracy of $\pm 0.0003\ mm$ ($\pm 0.000012"$), high-rigidities, and constant continuous torques. The encoders fulfill the requirements for the high-accuracy metrology applications. Their most important features are very high-resolution, $28\ bits$ ($2^{28} \sim 268\ million\ counts/revoultion$), very good system accuracy of: $\pm 2.5\ arc - sec$ ($0.00069°$), a bi-directional repeatability of: $\pm 1.2\ arc - sec$ ($0.00033°$), and excellent signal quality, even when operating at varying temperatures. FIGURE 40 shows the encoder module.
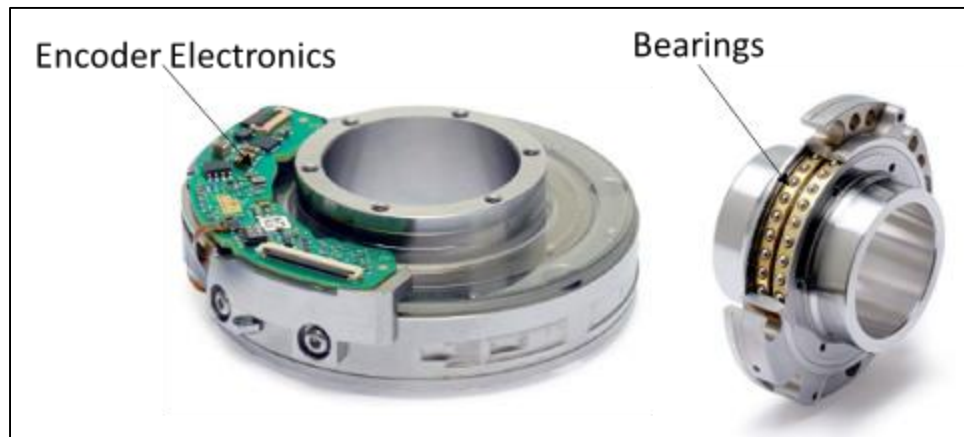
FIGURE 40: Heidenhain angular encoder module MRP 5010 (source: Heidenhain)

The measuring instrument incorporates a module for each arm. The encoders output EnDat2.2 status words for absolute positon. The modules work with an EIB 741 Heidenhain interface box and can be used with provided in-house software or customer specific software, such as LabVIEW for this measuring instrument.

Before the new measuring instrument is fabricated, a couple calculations were done to see if the measuring instrument can handle up to the rigors of a measuring process. The first calculations done were some arm strength and stiffness tests, to see how the arm would hold up to loading. Finite Element Analysis (FEA) of the arm was done in SolidWorks Cosmos package. The arm material is assumed 4041 steel with a yield stress of 655 MPa (95 ksi). The arm is treated as a simple cantilever beam, where the fixed-end is attached to the body. FIGURE 41 shows the setup of the FEA analysis.
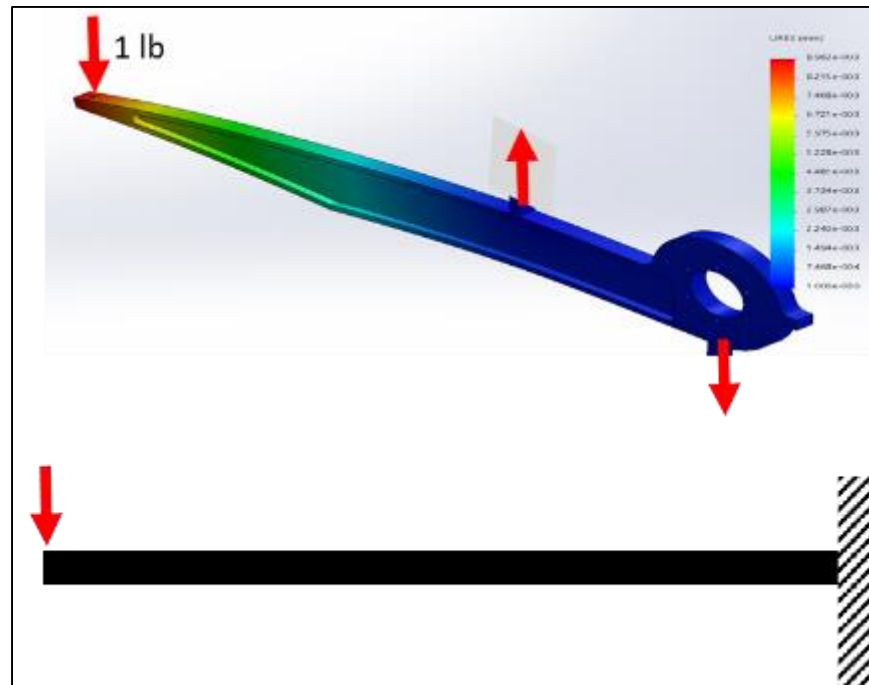
FIGURE 41: Arm strength and stiffness setup for FEA

The arm was constrained to test in-plane loads and out-of-plane loads. For the in-plane loading, with a $4.44\ N$ ($1\ lb_f$) located at the end of the arm, the max displacement of the arm is approximately $0.0089\ mm$ (0.00035"). The estimated max force during measurement is approximately $0.444\ N$ ($0.1\ lb_f$), from the beam spring, so the displacement of the arm end bending should not significantly affect the results of the measurement. The load to cause in-plane yielding of the arm is approximately $2.5\ kN$ ($561\ lb_f$). For the out-of-plane loading, the load to cause yielding is approximately $226\ N$ ($50.86\ lb_f$), indicating that the arms should be safe from improper handling of the instrument.

The spring design for the arm is considered for desired stiffness and range-of-motion at the contact sphere. FIGURE 42 has a detailed view of the arm and spring design.
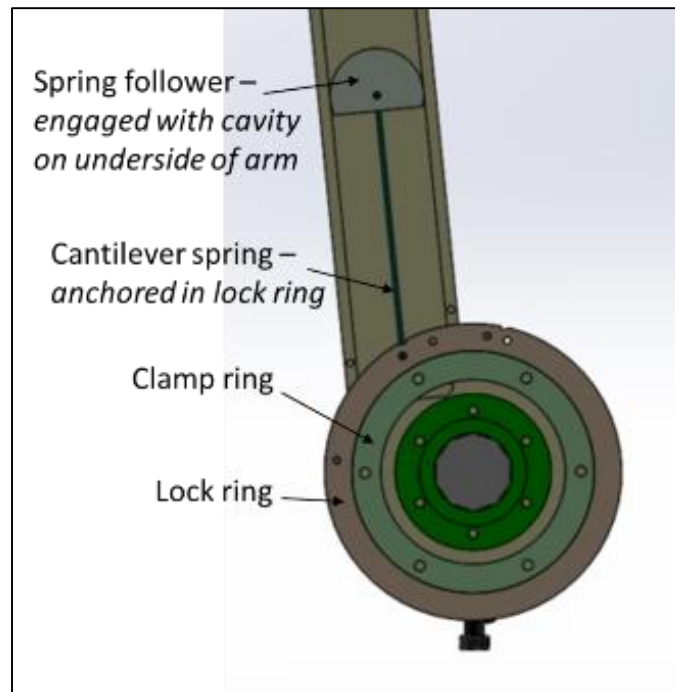
FIGURE 42: Arm spring design

The desired stiffness at the contact point is $K_c = 87.5 \frac{N}{m}$ $(0.5 \frac{lb}{in})$ with a desired range of motion of $\pm 31.75\ mm\ (\pm 1.25")$, which is approximately $5°$ $(18000\ arc - sec)$, of arcing motion. The required stiffness of the spring is $K_s = K_c (\frac{L_{arm}}{L_{spring}})^2 = 809.1 \frac{N}{m}$ $(4.62 \frac{lb}{in})$, where K_s is the required spring stiffness, K_c is the desired contact point stiffness, L_{arm} is the length of the arm and L_{spring} is the length of the spring. The required range-of-motion is $\pm 10.41\ mm\ (\pm 0.41")$. Using a spring made of ASTM A228 music wire, with an effective length of $76.2\ mm$ $(3")$, and with the required spring stiffness, K_s, the max stress of the spring arm design is $1631.8\ MPa\ (236,675\ psi)$, with a yield stress of $1999.5\ MPa\ (290,000\ psi)$. So the spring design will hold up to the necessary forces from the measurement.

FIGURE 43 shows the prototype of the new measuring system.
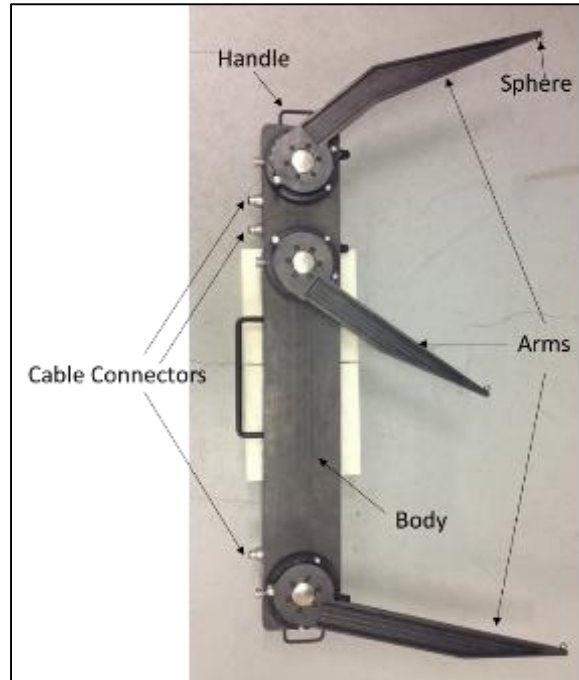
FIGURE 43: Prototype of second measuring instrument

CHAPTER 5: EXPERMENTAL SETUP AND TESTING

5.1. Preliminary Testing

Before testing the measuring instrument in an experiential setup, some preliminary testing is done to ensure that errors from the measuring instrument are a small influence on the measured data. The tests done before testing the measuring instrument are a drift test, hysteresis test and repeatability test.

5.1.1. Drift Test

The drift test is used to see how the measuring instrument will be influenced by temperature over a certain period of time. Thermal effects can have a significant effect on the measuring instrument if it is being used for an extended period of time and can also support the effectiveness of procedural solutions, such as working during the evening versus the day. The test is done by setting up the measuring instrument on a granite table and placing the arms up against angles blocks and locking the arms against the angle blocks with the spring force from the arms. The measuring instrument is constrained to the table with more angle blocks and C-clamps. The setup can be seen in FIGURE 44.
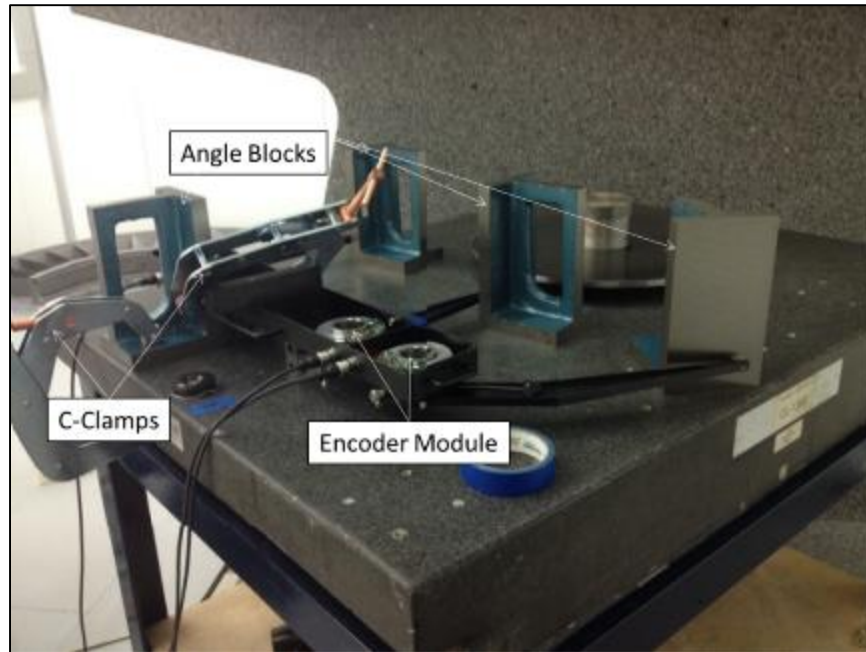
FIGURE 44: Drift test setup.

The environment, in which the drift test is conducted, is in the Siemens Large-scale Manufacturing Solutions Laboratory. The ambient temperature range, from the calibration certificate, is $20°C \pm 0.5°C$. The measuring instrument collects data for approximately 60 minutes. The length of time is chosen because the average measuring time for using the measuring instrument is approximately 20 minutes from start to finish but could last up to an hour. This includes setting up the measuring instrument on the turret, engaging the measuring instrument on the circular component and rotating the circular component, while the measuring instrument is collecting data. FIGURE 45 has the drift test results.
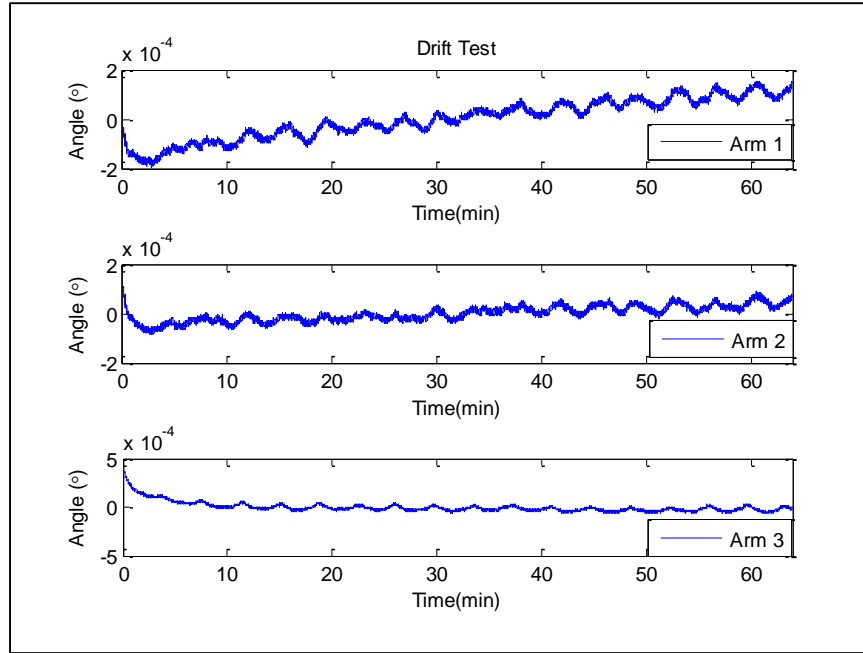
FIGURE 45: Drift test results

After the measuring instrument collected data for an hour, the drift is determined for both the 20 minute and 60 minute time frames. The drift, for both time frames, is determined by calculating the range of the data for the 20 minute time frame and then a 60 minute time frame, respectively. The results can be seen in TABLE 3.

TABLE 3: Drift test result values (20 and 60 minutes)

Drift Results	20 min	60 min
Arm 1	0.0002149°(0.773999 arc-sec)	0.0003500° (1.26000 arc-sec)
Arm 2	0.0001290° (0.464400 arc-sec)	0.0001958° (0.70488 arc-sec)
Arm 3	0.0001270° (0.457200 arc-sec)	0.0004680° (1.6848 arc-sec)

The average drift of 20 minutes is $0.000157°$ $(0.5625\ arc-sec)$ and the 60 minute average is $0.000338°$ $(1.2616\ arc-sec)$. From the results, drift error should not contribute significantly to the measurement result, however the uncertainty from the environmental factors will be included in the uncertainty analysis of the measuring instrument result.

5.1.2. Hysteresis Test

The hysteresis testing is done to see how well each arm reacts to a force applied on the contact sphere and to see if the measurement returns back to its initial readings. This can also tell if an external force is momentarily applied to the sphere contact, how deformation can affect the measuring process.

To test the hysteresis in each arm, the measuring instrument is setup on a very stiff base, and each arm is placed up against another very stiff object, an angle block. Initially, the only force acting on the arm, the normal force from the angle block, is due to the spring force in the arm. After the setup is complete, an external force is applied to the arm through the sphere, force from a finger push, into the angle block and then released after about a second time lapse. This is done approximately 10 times to see how well the system responds and see how much hysteresis error there is in each arm. FIGURE 46 shows the hysteresis test setup.
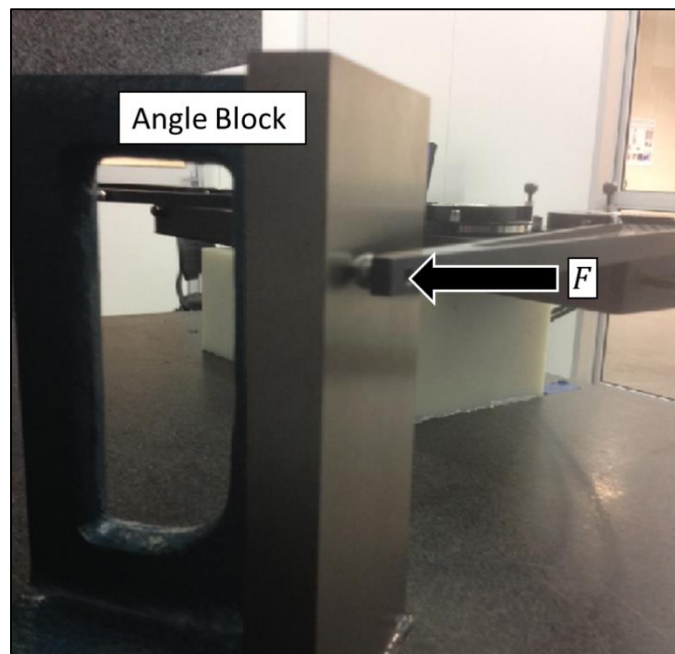
FIGURE 46: Hysteresis test setup

FIGURE 47 shows the results of the hysteresis test.
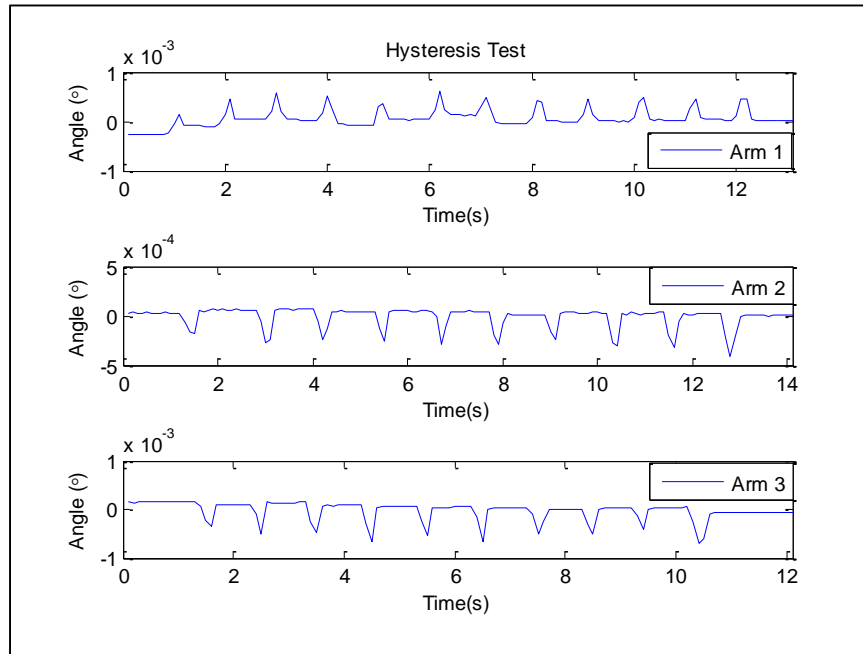
FIGURE 47: Hysteresis test results

FIGURE 48 shows a close up of the hysteresis results.
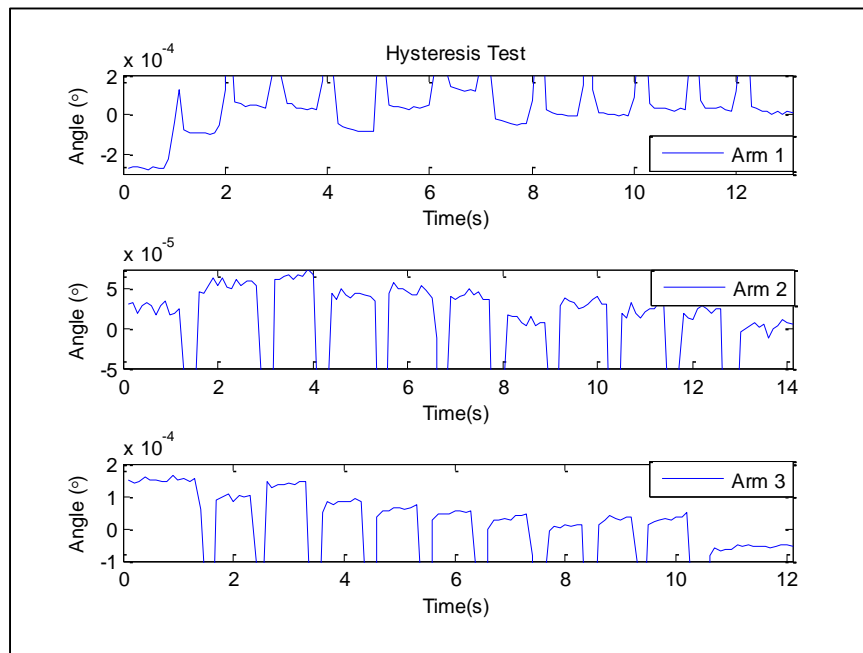
FIGURE 48: Hysteresis results (zoomed)

The hysteresis error for each arm can be seen in TABLE 4.

TABLE 4: Hysteresis test result values

Hysteresis	
Arm 1	0.0002810° (1.01160 arc-sec)
Arm 2	0.0000259° (0.09324 arc-sec)
Arm 3	0.0002050° (0.73800 arc-sec)

The results are determined by taking the absolute difference between the last data value to the first data value. The average hysteresis is $0.00024°$ $(0.6143\ arc-\sec)$. From the results, the hysteresis should not contribute significantly to the measurement result, however the uncertainty from the hysteresis test will be included in the uncertainty analysis of the measuring instrument result.

5.1.3. Arm Repeatability Test

The arm repeatability test is used to see how well each angular encoder module on the measuring instrument will repeat the same measurement under the same conditions. Each arm is tested for uni-directional repeatability by using a glued down angle block and letting each arm end sphere rest up against the angle block, with the force of the spring holding the arm in place. Each arm is then pulled away from the angle block, then eased back into its initial position and the measurement value is recorded. This is done a total of five times to see how well the arm angle repeats. The reason for uni-directional repeatability is because the spring force acts in one direction and the arms can only contact a component surface in one direction. FIGURE 49 shows the arm repeatability setup.

FIGURE 49: Arm repeatability test setup

FIGURE 50 shows the results from the arm repeatability test.
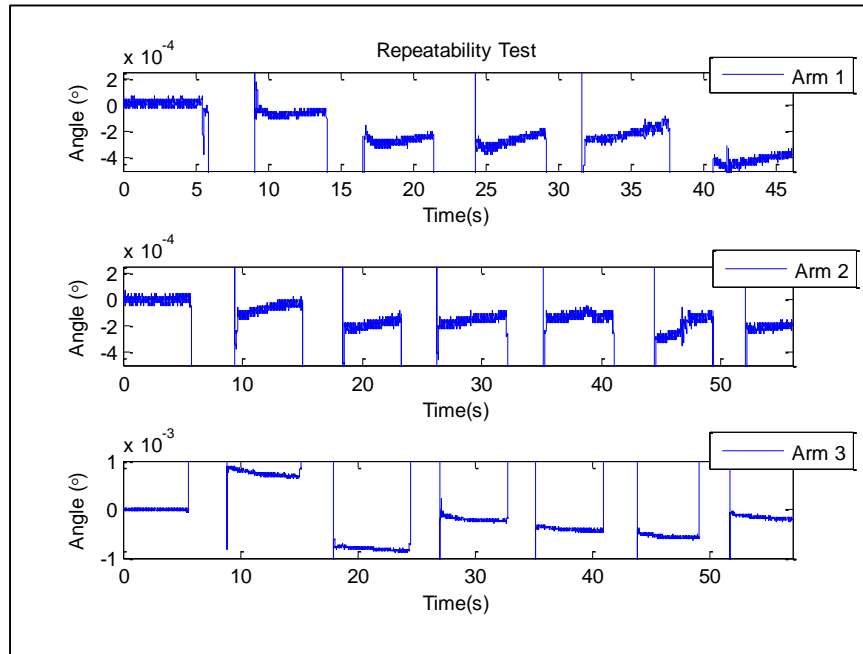
FIGURE 50: Arm repeatability test results

The repeatability of the three arms can be seen in TABLE 5.

TABLE 5. Arm repeatability test result values

Repeatability	
Arm 1	0.000160° (0.577285 arc-sec)
Arm 2	0.000123° (0.444531 arc-sec)
Arm 3	0.000086° (0.312066 arc-sec)

The arm repeatability values are calculated by calculating the averages of the plateaus and then taking the standard deviation of the five averages. From TABLE 5, it can be seen that the measuring instrument has very good arm repeatability. The average arm repeatability is $0.000123°$ ($0.4448\ arc-\sec$).

Further testing of the form error and diameter measurements are conducted to look at the repeatability of the actual measuring process and the uncertainty associated with it. This preliminary test is used as step to look to see if there are any significant errors from assembly.

5.2. Kinematic Parameter Measurements

The kinematic parameters of the measuring instrument are measured on a high-precision CMM and these values are used for the calculation of the components diameter and form error. The measuring instrument is setup in the CMM volume, via a portable granite table. C-clamps are used for holding the measuring instrument to the granite table and to an angle block, and $1 - 2 - 3$ blocks are used to raise the measuring instrument off the granite table. All blocks are glued to the granite table, to ensure the measuring instrument does not move during the CMM measurements. FIGURE 51 has the measuring setup.
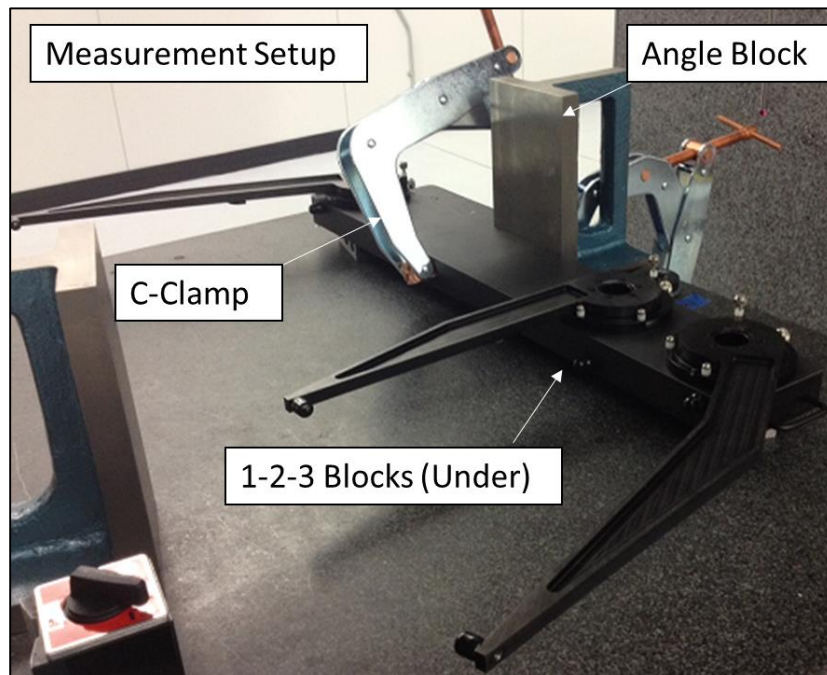
FIGURE 51: Measuring instrument setup on CMM for measuring kinematic parameters

To measure the kinematic parameters on the CMM, each arm is moved in an arcing path to five different locations, during which the contact sphere is measured. The sphere is measured multiple times at each position, to determine the x and y coordinates at each position. FIGURE 52, FIGURE 53 and FIGURE 54 show schematics of measuring the kinematic parameters of each arm, respectively.

FIGURE 52: Schematic of measuring arm one kinematic parameters on CMM

FIGURE 53: Schematic of measuring arm two kinematic parameters on CMM

FIGURE 54: Schematic of measuring arm three kinematic parameters on CMM

During the measurement of the arms, the angle of each arm position is collected from the encoder module. The arm angles can be used to calculate the angular offset of each arm, along with the x and y coordinates of the spheres from the CMM measurement, at the current position. A byproduct of the measurements is the diameters of the spheres. The radius of the spheres are needed, to subtract out from the measured diameter data, to represent that actual diameter measured. If this radius is not subtracted out, the diameter measurement will be off by the radius of the contact spheres.

From FIGURE 52, the kinematic parameters L_1 and $\theta_{1,offset}$, can be determined, from FIGURE 53, the kinematic parameters L_2, Y_b, X_b and $\theta_{2,offset}$, can be determined and from FIGURE 54, the kinematic parameters L_3, Y_c, X_c and $\theta_{3,offset}$ can be determined.

For the length kinematic parameters to be determined, the coordinates from the CMM measurements need to be transformed into the measuring instrument coordinates via a transformation matrix. First the CMM coordinates are fit to a least squares fit, to determine the center position (O_1, O_2, O_3) of each arm pivot and the center-to-center lengths of each arm. All CMM measurements are referenced from the origin of the first arm, as can be seen in the previous figures, thus the length kinematic parameters can be determined, in CMM coordinates, from the least square fit. Once the center positions are determined for each arm, a transformation matrix can be calculated. The transformation matrix is shown in Eq. (61).

$$T_{Inst}^{CMM} = \begin{bmatrix} \dfrac{Y_{center3} - Y_{center1}}{D_{13}} & -\dfrac{X_{center3} - X_{center1}}{D_{13}} & -X_{center1} \\ \dfrac{X_{center3} - X_{center1}}{D_{13}} & \dfrac{Y_{center3} - Y_{center1}}{D_{13}} & -Y_{center1} \\ 0 & 0 & 1 \end{bmatrix} \quad (61)$$

Where $D_{13} = \sqrt{(X_{center3} - X_{center1})^2 + (Y_{center3} - Y_{center1})^2}$, is the distance from arm pivot one to arm pivot three, in CMM coordinates. The (X_{center}, Y_{center}) values are from the least square fit of the CMM coordinates. With the transformation matrix defined and all values known, the transformation matrix can now be used to transform the CMM coordinates to the measuring instrument coordinates. By multiplying the transformation matrix by the original CMM coordinates, a new set of coordinates is determined with reference to the measuring instruments origin, O_1. Using the new coordinates, the same least square fit is used to determine the length kinematic parameters, in the measuring instrument coordinates. TABLE 6 has the length kinematic parameters.

TABLE 6: Length kinematic parameters

KP's	mm	in
L_1	368.77843	14.51884
L_2	298.52935	11.75312
L_3	368.39609	14.50378
X_B	-0.03715	-0.00146
Y_B	127.03384	5.00133
X_C	-1.90E-05	0.00000
Y_C	551.18689	21.70027

The angular offset kinematic parameters, $\theta_{1,off}, \theta_{2,off}, \theta_{3,off}$, are also measured on the CMM. Using FIGURE 52, FIGURE 53 and FIGURE 54, when the CMM measures the different positions of the arms, the angular displacement of the arms is collected from the encoder modules. These angular displacements are referenced to a home position on the scale of the encoder module. The CMM measures the arm positions and determines x and y coordinates, of each position and $atan2$ function is used to determine the absolute angle positions, from the coordinates. However, the CMM angles must be determined from the transformed coordinates, since all measurements are referenced to the measuring instrument, thus $atan2$ is used on the transformed coordinates determined earlier. The CMM measurements are absolute from the positive x axis of the CMM coordinate system, which can been seen in FIGURE 52, FIGURE 53 and FIGURE 54, and the angles for the measuring instrument are to be referenced from its positive x axis, so the difference from the calculated CMM angles and encoder module angles, are the angular offsets. The offsets are an average of the five different positions.

TABLE 7 shows the angle offset kinematic parameters.

TABLE 7: Angular offset kinematic parameters

KP's	$\theta_{1,off}$	$\theta_{2,off}$	$\theta_{3,off}$
deg	167.45108	-1.22949	239.40301

5.3. Experimental Setups

The testing of the measuring instrument is conducted on several different components, a 25.4 mm (1") thick aluminum plate, with an approximate diameter of 508 mm (20"), a 38.1 mm (1.5") thick aluminum ring, with an approximate diameter of 254 mm (10"), and an aluminum stock cylinder, with an approximate diameter of 101.6 mm (4"). All three components will be measured for both the diameter and the form error and compared to the CMM measured value. The component's sizes are chosen to simulate typical diameters that can be seen in a large-scale manufacturing environment. To test a larger range of diameters, 508 mm − 1778 mm (20" − 70"), a testing setup to simulate large "virtual" components is done. It should be noted that the form error of these large "virtual" components is not measured because the setup cannot continuously rotate and there is not constant contact with the component.

The smaller components are shown below in FIGURE 55.
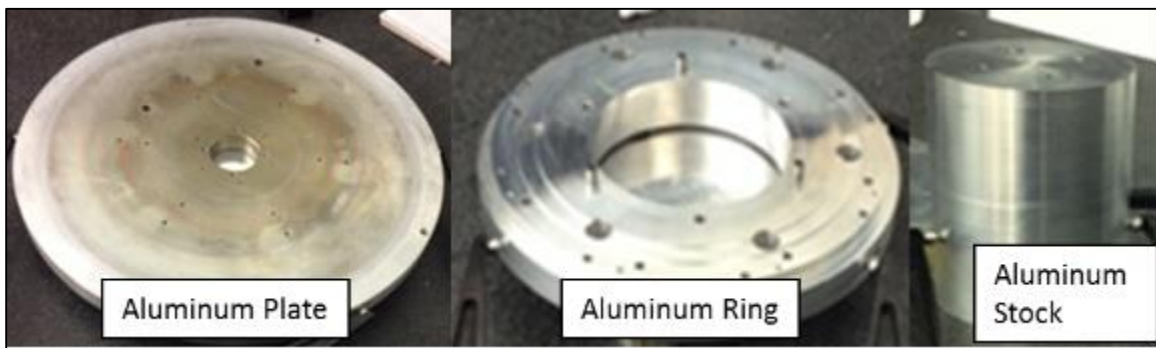
FIGURE 55: Components for testing measuring instrument

To setup the components to measure both the diameter and the form error, a spindle is needed. The new measuring instrument is designed to be fit into a lathe's tool-post, however, the available lathes cannot adapt the new measuring instrument because it is too large to fit vertically for testing. All the components from FIGURE 55 are measured horizontally on a synchronous rotary table that rotates at a constant speed of two RPM. Each component is glued down to the rotary table, to ensure it will not move during measurement. The component's centers are visually aligned with the center of the rotary table. This is done to see how well the measuring instrument can measure components not sufficiently centered. The measuring instrument is also placed on two blocks, to match the height of the components, and is also held in place to the blocks with glue to ensure it doesn't move during measurements. FIGURE 56, FIGURE 57 and FIGURE 58 show the measuring instrument setup for all three components measured on the rotary table setup.
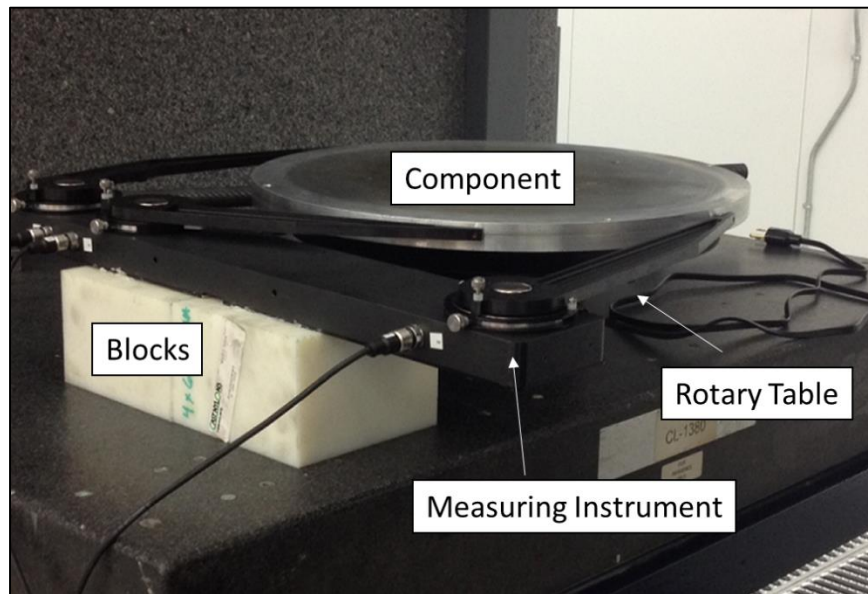
FIGURE 56: Setup for measuring instrument testing (aluminum plate)
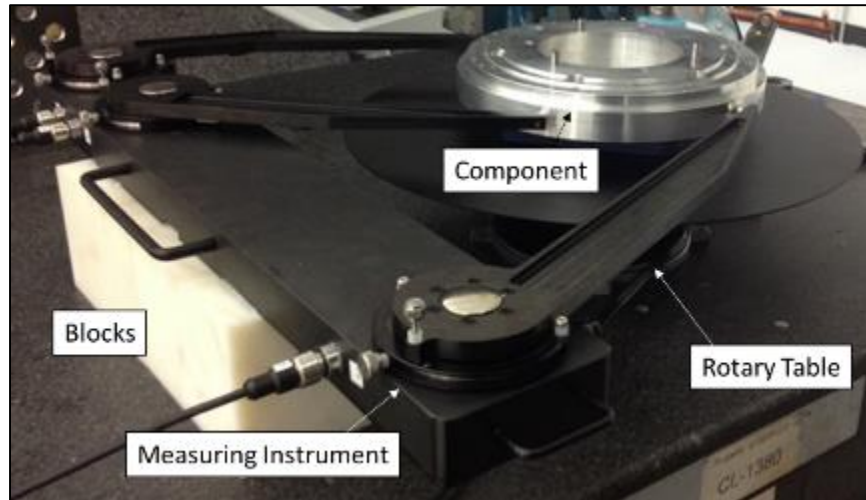
FIGURE 57: Setup for measuring instrument testing (aluminum ring)
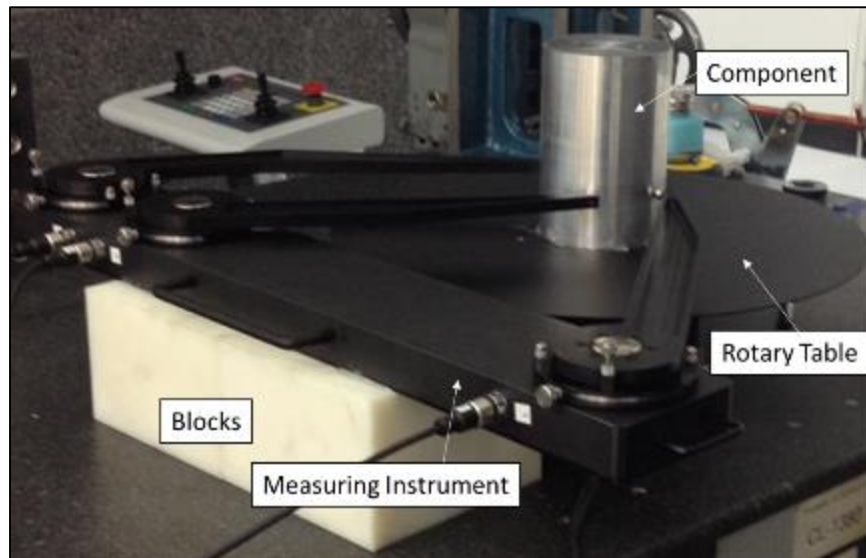
FIGURE 58: Setup for measuring instrument testing (aluminum stock)

As the component rotates, a small piece of tape is placed on the component, which is used to clock the data so that multiple revolutions of data can be superimposed and averaged to obtain the synchronous (average) data of multiple revolutions. Data is collected for at least ten revolutions of data at a sampling rate is $1000 \frac{samples}{sec}$.

For the virtual component setup, a manual rotary table is mounted onto a portable granite table. A piece of aluminum bar stock is clamped along the center of the rotary table, with a bearing ring glued to the end of the bar stock. This bearing ring simulates a low-form error surface and the bar stock simulates a large-scale radius. Different radii can be created by varying the stick-out length of the bar stock.
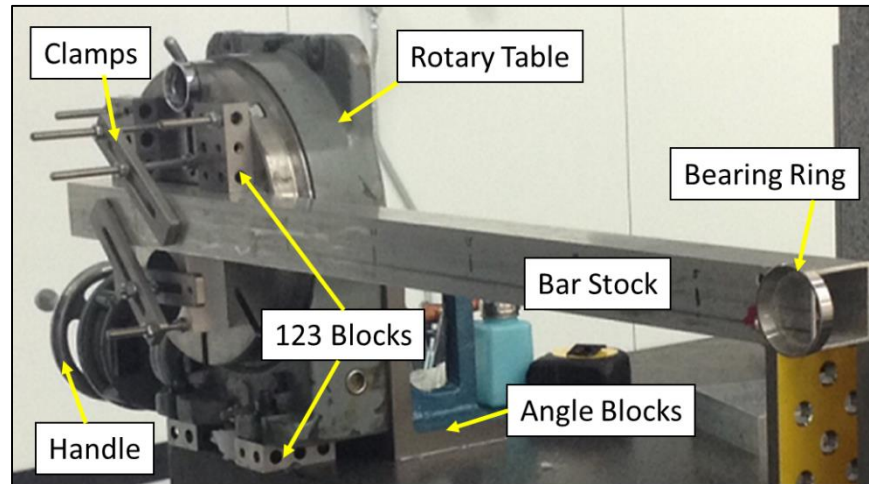
FIGURE 59: Large-scale "virtual" diameter setup

The rotary table is securely attached to the granite surface using angle blocks, C-clamps, and glue.

The measuring instrument is vertically mounted in the same plane as the aluminum bar, so that all the arms can contact the bearing ring during measurements. C-clamps hold the measuring instrument in place during measurements. FIGURE 60 shows the measuring instrument setup for measuring the virtual disks.
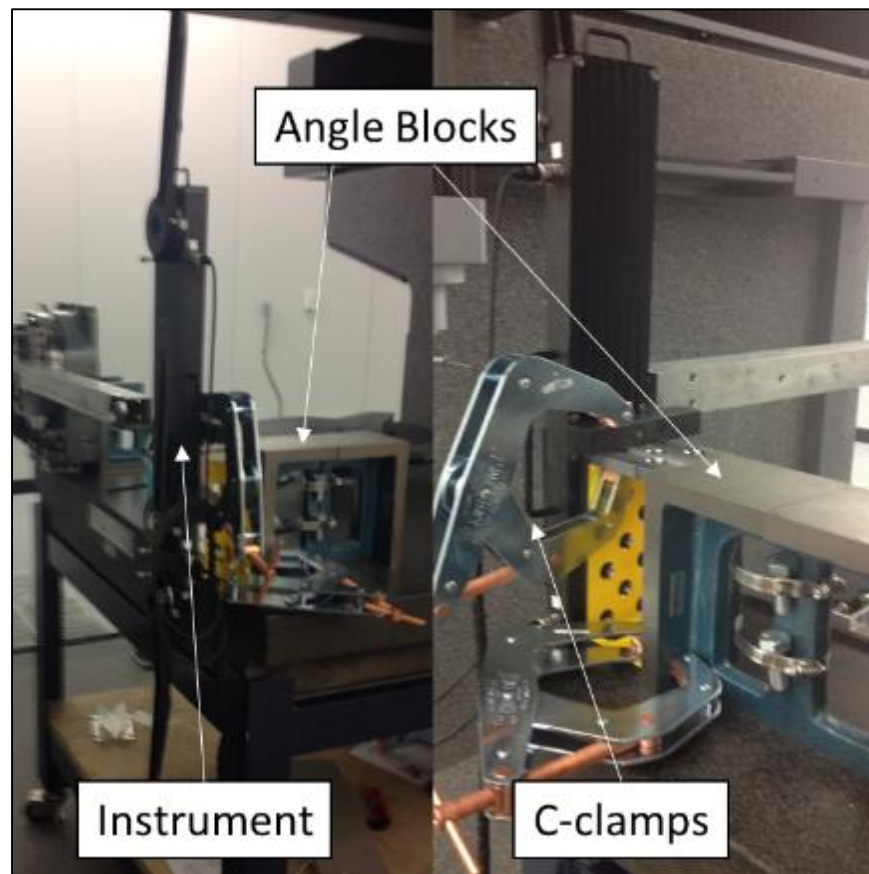
FIGURE 60: Measuring instrument setup for virtual disks

5.4. Measuring Instrument Testing and Results

The actual location of the point of contact between the contact sphere and the component being measured depends on the arm angle. However, the center of each contact sphere is always one sphere radius away from the physical contact point. Therefore, all of the measurement algorithms will find the properties of a circle that passes through the centers of the contact spheres. To obtain the correct circle diameter, the average radius of the contact spheres is subtracted out from the measured data. The radius of each sphere was measured during the kinematic parameter measurements on the CMM. This radius corrected data is used for both the reconstruction of the form error and diameter measurements.

During component rotation, the data is periodic, which is caused by the synchronous component of the form errors, spindle error motions and eccentricity in the component setup. To segment the data into individual revolutions for processing, a physical mark is placed on the actual component under test, which can be a scribe in the component or in the case of this testing a piece of tape. The data from the testing is averaged over a number of revolutions, $10 - 15$, which produces the synchronous motion.

The measuring instrument is capable of measuring diameter and form error with different separation distances from the component. Ideally it should give the same results regardless of separation. This will be tested by repeating measurements of the same object with the measuring instrument moved in its x direction over an approximate $50.8\ mm(2'')$ range, and results will be compared. FIGURE 61 shows a schematic of the measuring instrument incrementing out of the component, from position one to position two.
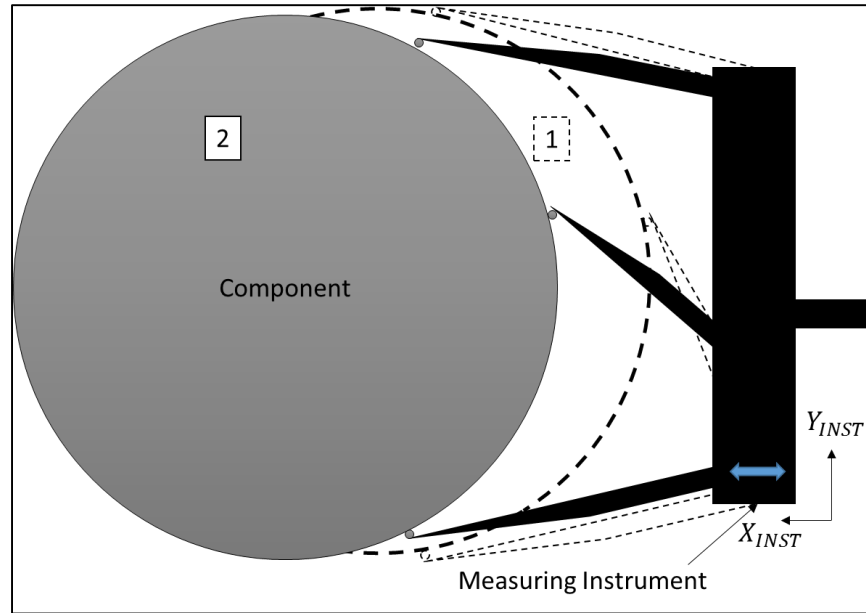
FIGURE 61: Measuring instrument incrementing of component schematic

During the measurement process, the encoder modules read the angular displacement of the arms. The CMM measured angular offsets, TABLE 7, are added to the measuring instrument values, to reference all angles to the absolute position of the positive x axis of the measuring instrument coordinate system. FIGURE 62 shows raw data from the measuring instrument when the component under-test is rotated for several revolutions.
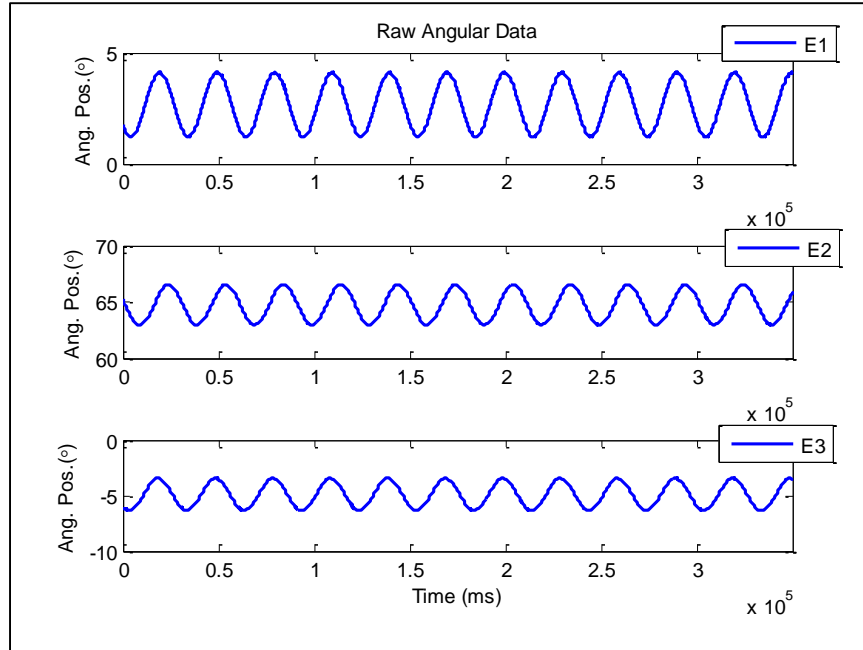
FIGURE 62: Raw angular data, multiple periods (revolutions)

The angular range of the data is large due to the centering errors of the part on the turntable, but this should ideally not affect either the diameter or form error measurement results.

After the data is collected, the data is truncated to include an integer number of revolutions. The number of revolutions of data is determined by finding the number of times the arms go over the physical mark, tape. From FIGURE 62, it can be seen that the range of data is too large to see the peak in the data from the physical mark, however, the software for calculating the diameter and form error, also takes into account finding the peak from the physical mark, to determine the number of revolutions and to calculate the average data. Zooming in on the raw data from FIGURE 63, the peak from the physical mark on the component of measure can be seen in FIGURE 63.
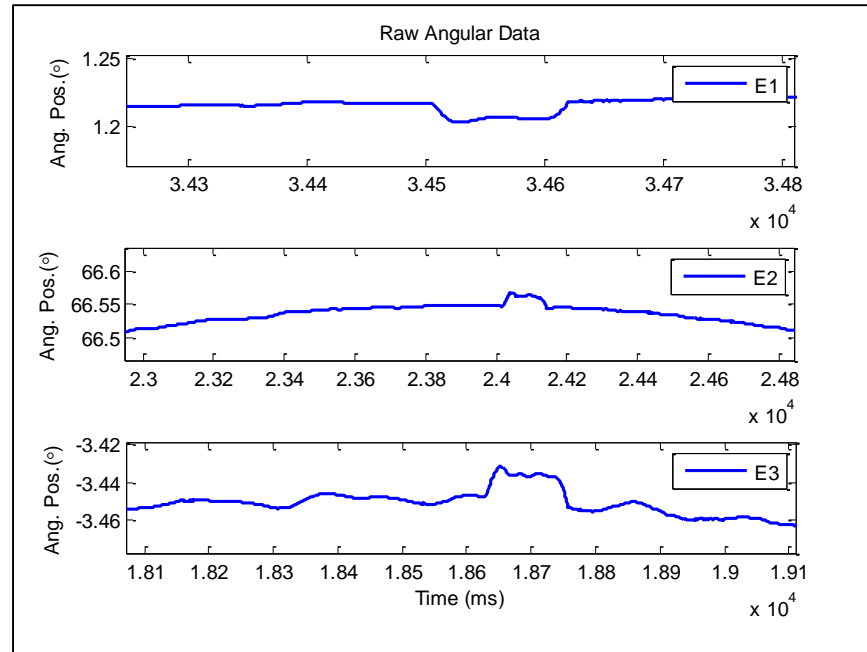
FIGURE 63: Zoomed in raw data, with physical mark peak in data

Using the physical mark peak as the starting point for a period of data, the number of revolutions is now determined by counting the number of peaks in the data. With the data now truncated, the data from each revolution can be placed into a matrix of rows equal to the number of data points per period and columns equal to the number of revolutions in the data set. The time step for the data is also converted to the angular domain, to represent the angular position around the circumference of the component. FIGURE 64 shows the reshaped data.
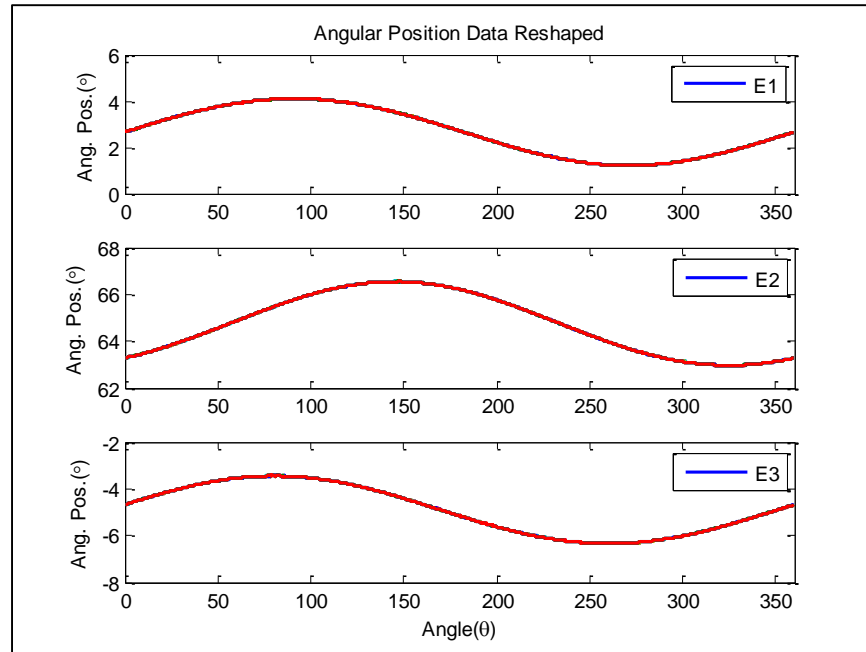
FIGURE 64: Reshaped data from single vector to matrix the length of period by number of revolution

The data from FIGURE 64 is averaged over the number of revolutions and is used for

determining the component's diameter.
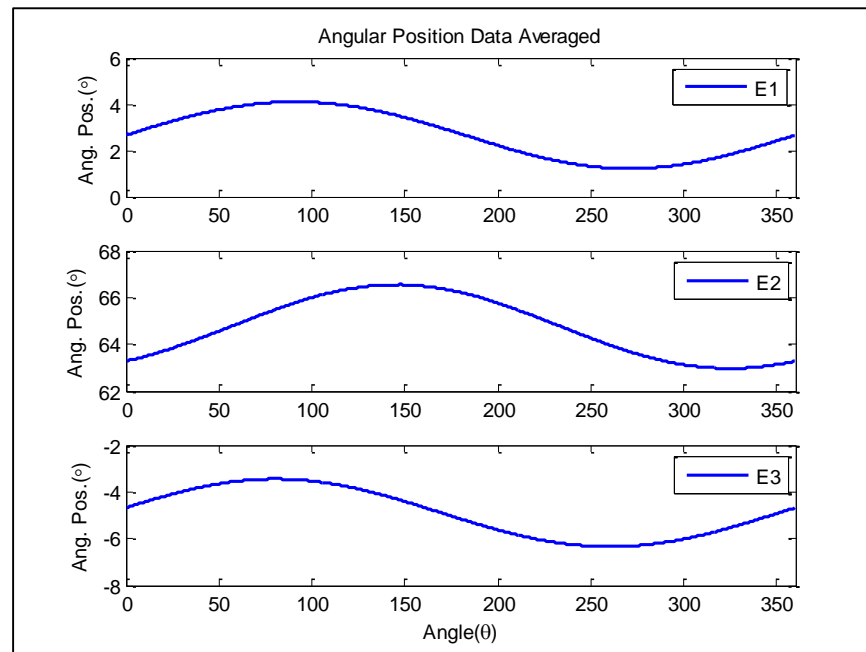
FIGURE 65: Averaged periodic data of component

The multi-probe error separation technique requires radial linear displacements from an average position. To determine the residuals of the averaged data, a best-fit circle is fit to the averaged data using methods described in *ASME B89.3.4M* standard [18]. This method is also used for removing eccentricity from the CMM measurements that will be presented in section 5.4.2. FIGURE 66 shows the average data with the best-fit data.
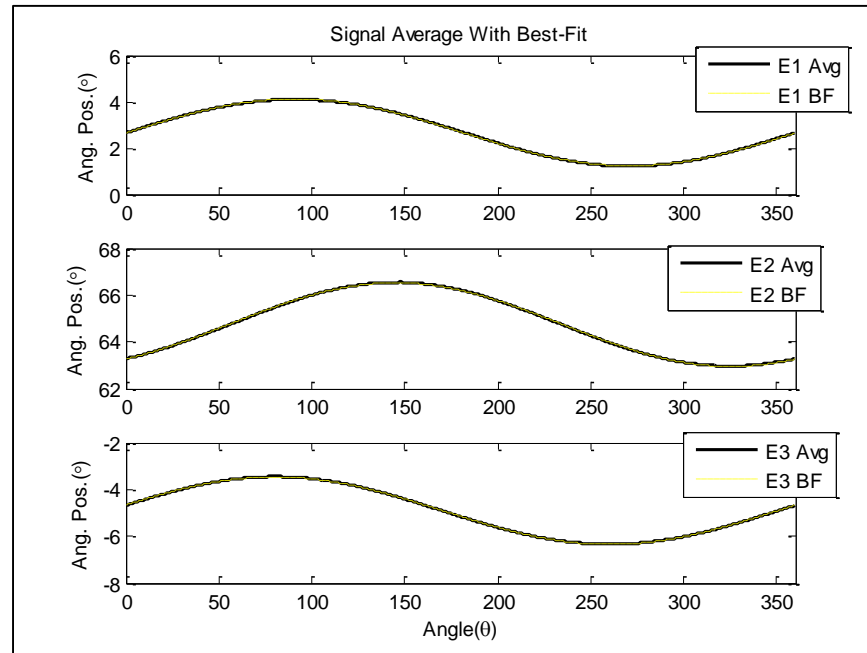
FIGURE 66: Average periodic data with best-fit circle

Now the residuals can be found by subtracting the averaged data from the best-fit data. FIGURE 67 shows the residual data.
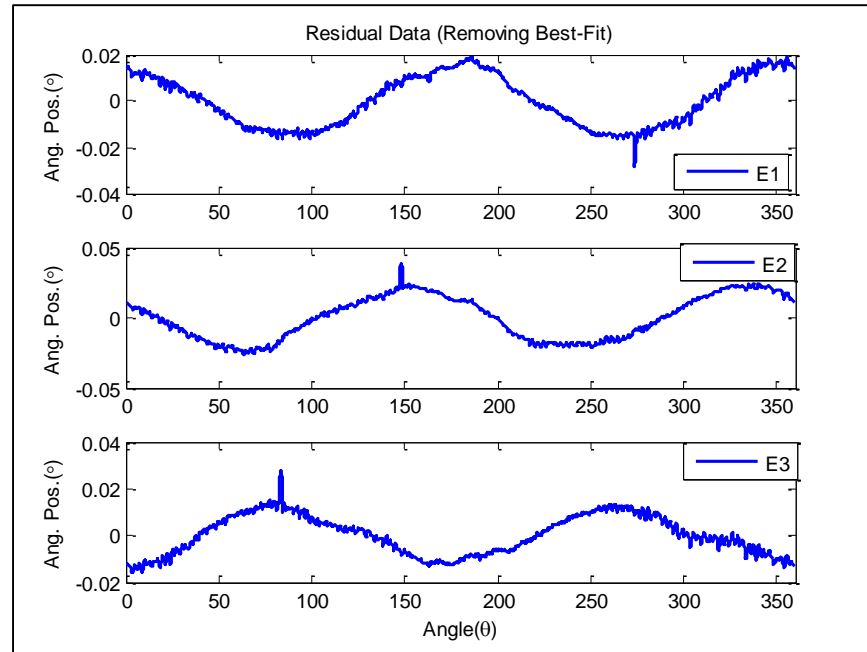
FIGURE 67: Residual data of component

    The noise in the measured data is a combination of rotary table vibration, encoder module electronic noise and other sources attributed to setup. To smooth the data, a simple 11-point moving average low-pass filter is used. The moving average filter is used because it will clean up all the high-frequencies of the data, but leave the low-frequencies intact, so there is still enough data for reconstructing the size and form metrology.
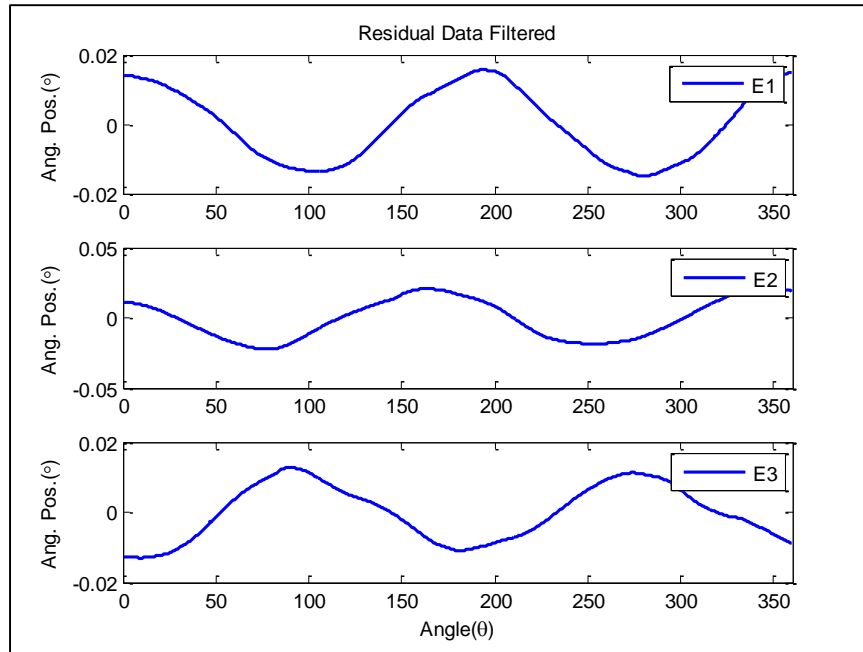
FIGURE 68: Filtered residual data of component

The multi-probe error separation method uses a change in radial linear displacement for measuring the form error of a surface. However, the encoder modules produce angular displacements, from an absolute reference, so a relationship between angular displacement and radial linear displacement is needed.

When a rigid body rotates about a fixed axis, the angular displacement is $\Delta\theta$, which is the angle in degrees through which a point or line has been rotated in a specified sense about a specified axis. FIGURE 69 shows an example of angular displacement.
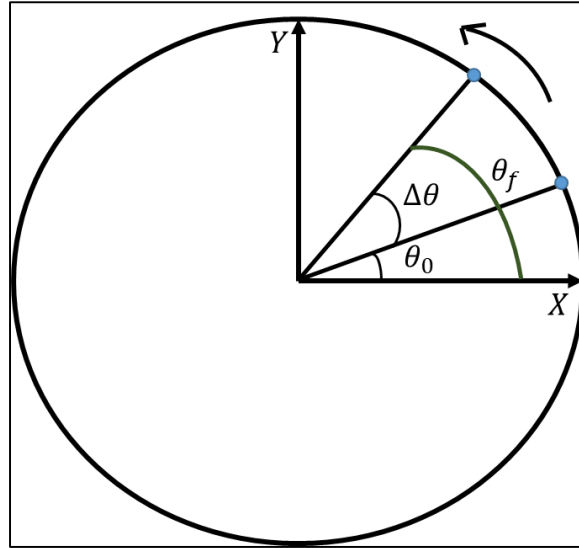
FIGURE 69: Angular displacement from reference point

Thus the angular displacement is calculated by Eq. (62).

$$\Delta\theta = \theta_f - \theta_0 \tag{62}$$

Where θ_f is the measured angle of the encoder module and θ_0 is the offset from the reference point on the encoder module scale. Now that angular displacement is expressed, the relationship between angular and linear displacement can be determined. First the arc-length of the angular displacement can be expressed if the radius of the circle is known. Since the encoder modules read the angular displacement of the arms, each arm length is treated as a radius of a circle, $R_{ARM,i} = R_i$. Where $i = 1,2,3$, for the number of arms. The relationship between angular displacement and linear displacement can be seen in FIGURE 70.
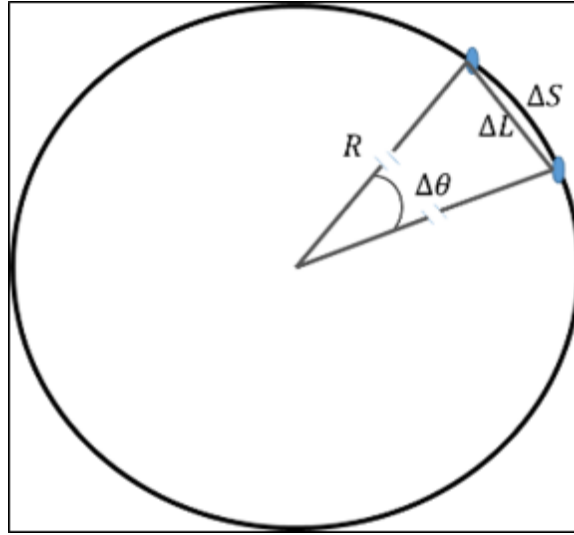
FIGURE 70: Relationship between angular displacement and linear displacement

Where the linear displacement can be derived from the following formula.

$$\Delta\theta_i = \frac{\Delta S_i}{R_{ARM,i}} \Longrightarrow \Delta S_i = \Delta\theta_i R_{ARM,i} \approx \Delta L_i \quad (R_{ARM,i} \gg \Delta\theta_i) \tag{63}$$

Where ΔS is the arc-length, R_{ARM} is the arm length (radius) and $\Delta\theta$ is the angular displacement. When the measuring instrument interfaces with the component and the component is rotated, the encoder modules will collect data streams of the arms at nearly constant angles. The actual angular displacement of the encoders will be very small compared to the arm lengths, $(R_{ARM} \gg \Delta\theta_1, \Delta\theta_2, \Delta\theta_3)$. So when the angular displacements are small relative to the radius, then the assumption of the arc-length representing a linear displacement can be used, $\Delta L_i \approx \Delta S_i$.

The direction of motion of the end of the arm is not necessarily in pure radial motion, unless the arm is perpendicular to the radius of the circular component at the contact point. In this case the linear displacement of the end of the arm needs to be projected into the radial direction. FIGURE 71, shows the linear displacement projected into the radial direction, all arms follow this method.
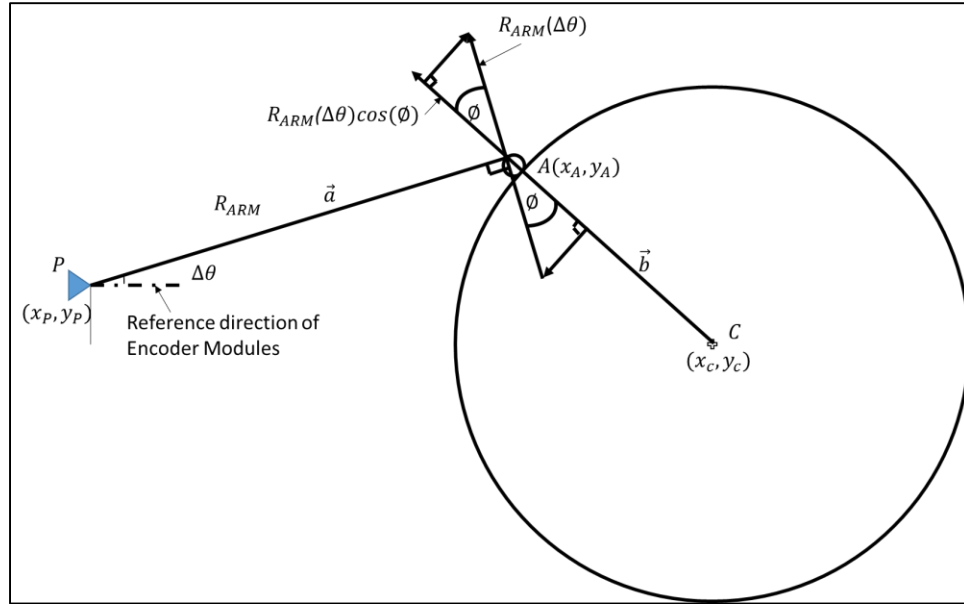
FIGURE 71: Schematic for projecting the linear displacement into the radial direction (exaggerated and not to scale. Arm one example)

   From FIGURE 71, the angle, $\emptyset$, projection angle, is needed for the linear displacement

to be projected into the radial direction. From the figure, the linear displacement is now a

function of the cosine of the projection angle. Eq. (63) is the updated linear displacement.

$$\Delta L_i = R_{ARM}(\Delta\theta)cos(\emptyset) \tag{64}$$

Since the x and y coordinates of the contact point (x_A, y_A), arm pivot point (x_P, y_P) and the center of the component (x_c, y_c), all in measuring instrument coordinates are known, the projection angle, $\emptyset$, can be determined by using the scalar projection of the arm end displacement vector and unit vector from the component center point to the contact point.

$$\emptyset = cos^{-1}(\frac{\vec{a}\cdot\hat{u}}{\|\vec{a}\|}) \tag{65}$$

Where $\vec{a} = <X_A - x_p, Y_A - y_p, >$, is the arm end displacement vector of point A, $\hat{u} = \frac{\vec{b}}{\|\vec{b}\|}$, is the unit vector from the contact point A to the center of the component in measuring instrument coordinates, where $\vec{b} = <X_A - x_c, Y_A - y_c, >$, $\|\vec{a}\|$, is the magnitude of the arm end vector and $\|\vec{b}\|$, is the magnitude of the vector from the contact point to the center of the component in measuring instrument coordinates. Contact points B and C follow the same method for determining the angle of projection. This angle is used for the corrected linear displacement. Eq. (65).

FIGURE 72 show the angular displacement data converted to linear displacement.
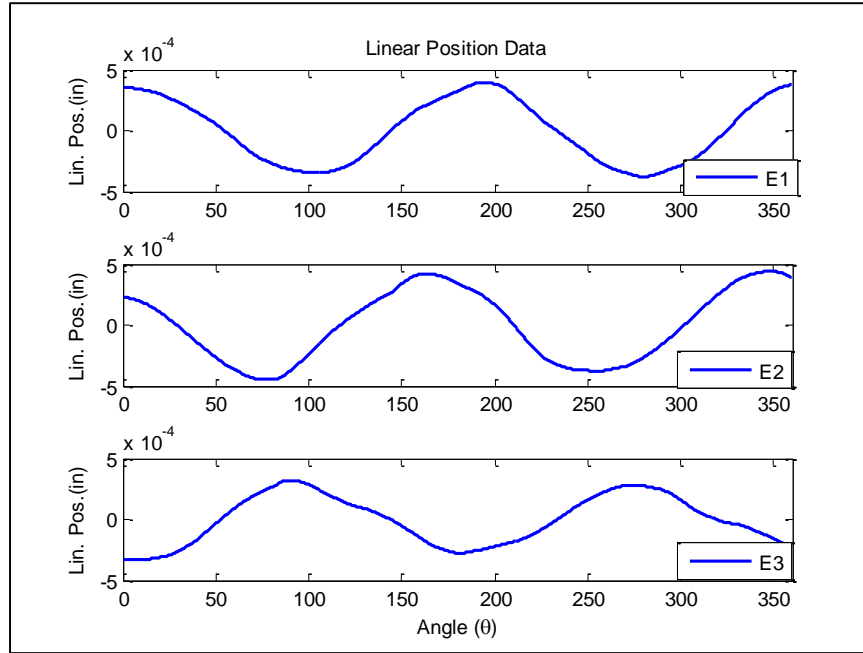
FIGURE 72: Linear displacement data used for the multi-probe method (unit = in.)

All components tested in this research follow the same data processing method for analyzing the form error and the diameter.

5.4.1. Form Error Results

To measure the form error of the component under testing, linear displacement data, like FIGURE 72, along with the algorithms from section 2.1, are needed for reconstructing the form error. The spindle error motions for each of the components measured are also determined and detailed, graphically and quantitatively, in Appendix B. The form error is obtained by using the multi-probe error separation method, by reconstruction of the component surface profile from a truncated Fourier series approximation using the first 25 UPR. Each component is measured twice, with the measurement instrument moved approximately $50.8\ mm$ (2″) in the negative x direction of the measuring instrument coordinate system. The planar angle locations, located from contact point one, $\alpha = 0^{\circ}$, for each of the measurements can be seen on TABLE 8.

TABLE 8: Planar angle locations for each measurement of form error

Component	Beta (β)	Gamma (γ)	Meaurement
Aluminum Plate	125.8638°	196.1335°	1
	113.1614°	175.8258°	2
Aluminum Ring	156.2565°	210.0782°	1
	105.3458°	175.8258°	2
Aluminum Stock	148.0625°	199.6503°	1
	81.2632°	162.6973°	2

All reconstructed component profile form errors are determined through 10 revolutions of data, to produce a good synchronous motion, needed to get the best possible results through averaging. FIGURE 73 and FIGURE 74 show the components profile form error for each of the components, for both measurements one and two.
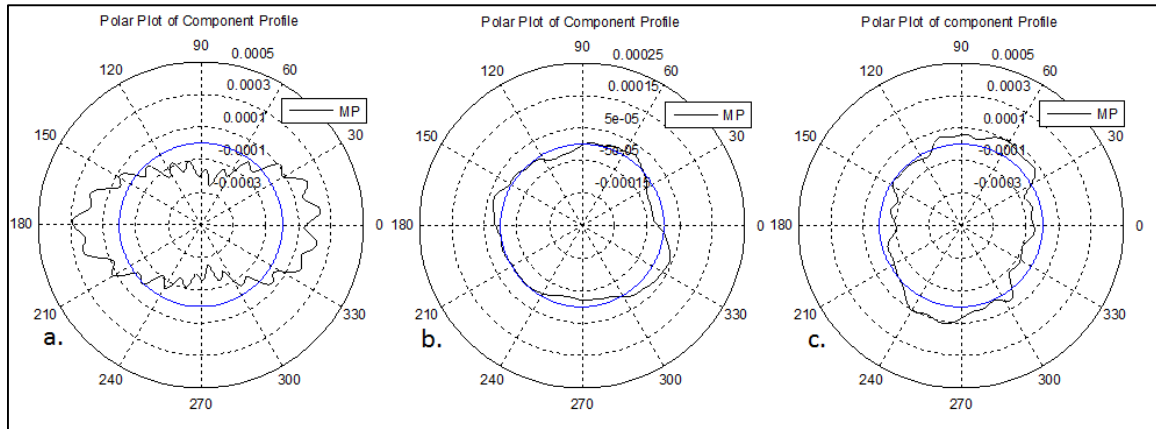
FIGURE 73: Component profile reconstruction, measurement one, a.) aluminum plate, b.) aluminum ring, and c.) aluminum stock
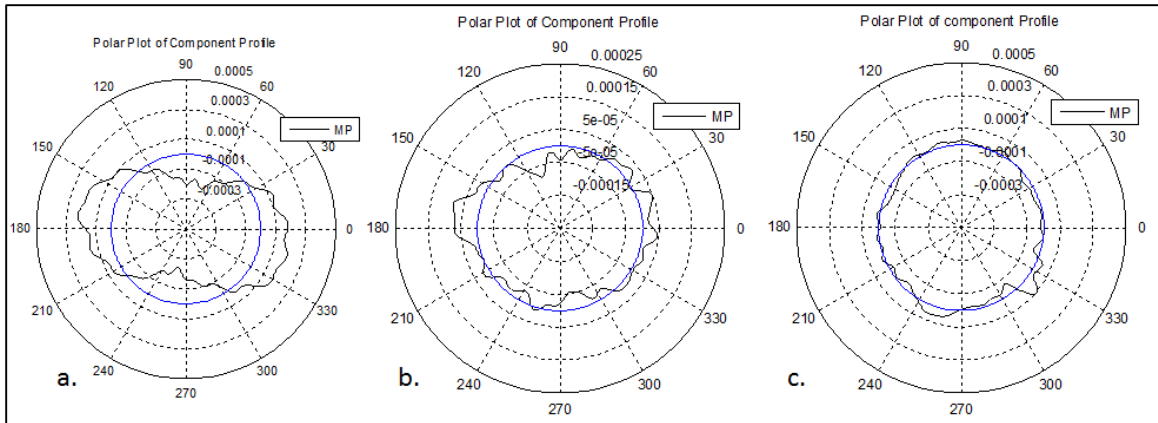
FIGURE 74: Component profile reconstruction, measurement two, a.) aluminum plate, b.) aluminum ring, and c.) aluminum stock

Since each component is measured twice, the two measurements can be compared to see how capable the measuring instrument is at measuring the same component profile, with different planar angles to reconstruct the form error. To see how comparable the measurements are, the two profiles are overlaid on the same plot and the point-to-point difference is determined from the profiles. FIGURE 75 and FIGURE 76 show the two measurement component profiles, overlaid, and the point-to-point difference between the two measurements, respectively.
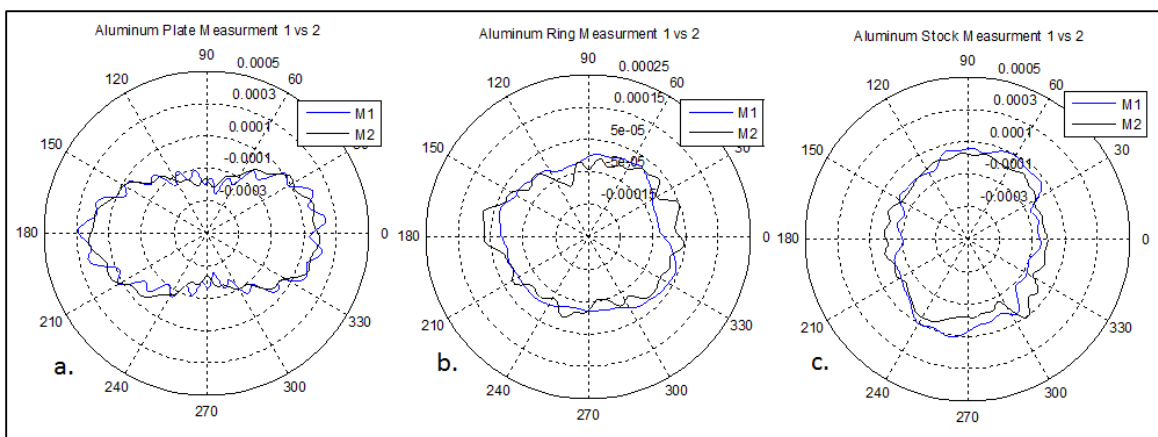
FIGURE 75: Measurements one and two, overlaid, for each component under test, a.) aluminum plate, b.) aluminum ring and c.) aluminum Stock
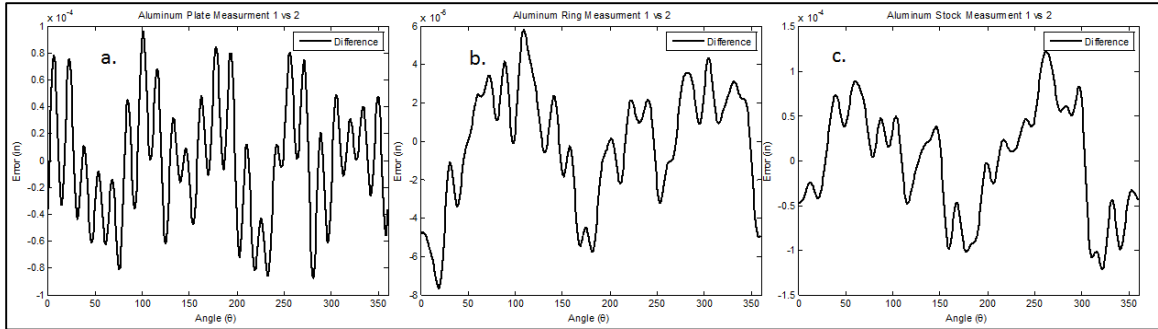
FIGURE 76: Point-to-point difference between reconstructed component profiles, a.) aluminum plate, b.) aluminum ring and c.) aluminum stock

The two measurement for each component measured, produce similar shapes, at the difference planar angle locations. From FIGURE 76, the error bands of the two measurements for each component can be determined. TABLE 9 shows the error bands.

TABLE 9: Error band of difference between the two measured profiles

Component	MAX	MIN
Aluminum Plate	0.0025 mm (0.00010")	-0.0020 mm (-0.00008")
Aluminum Ring	0.0015 mm (0.00006")	-0.0018 mm (-0.00007")
Aluminum Stock	0.0030 mm (0.00012")	-0.0030 mm (-0.00012")

These results show that the measuring instrument is capable of measuring the same component profile, at difference planar angle locations.

Each component is also measured by a CMM, at the same axial plane. The CMM measurements of the components are in x and y coordinates, so the data is post processed and analyzed in MATLAB. The CMM data is converted from Cartesian data to Polar data and the best-fit circle removed, to produce the residual data of the component, which is the surface profile, or form error, of the component. The residual data is then filtered with the same 11-point moving average filter used on the measuring instrument data. The CMM data is resampled to the same length as the measuring instrument data, for each measurement of each component, for a point-to-point comparison. A fiducial mark on the component is used to match up the two data sets, as best as possible. FIGURE 77 and FIGURE 78 shows the measuring instrument measured surface profile compared to the CMM measured surface profile and the point-to-point difference between the two profiles, for the aluminum plate, for each measurement, respectively.
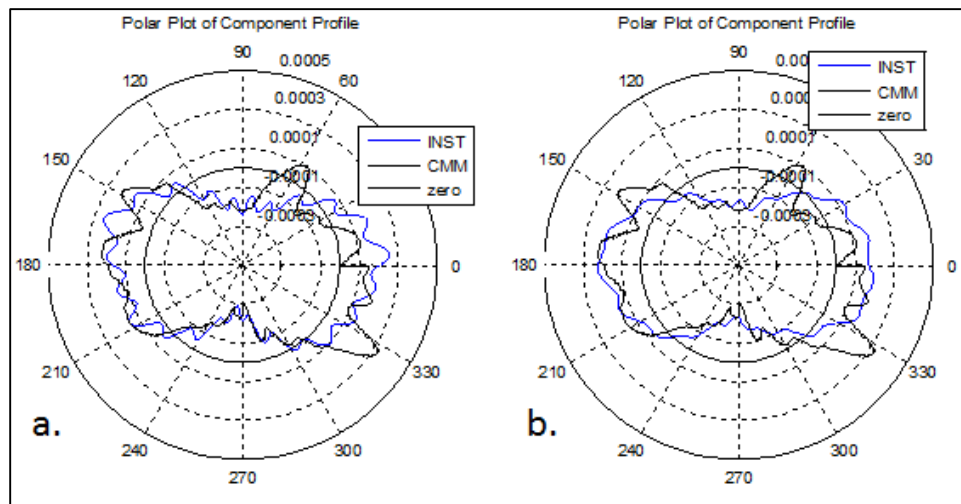
FIGURE 77: CMM and measuring instrument component profile comparison, aluminum plate, a.) measurement one and b.) measurement two
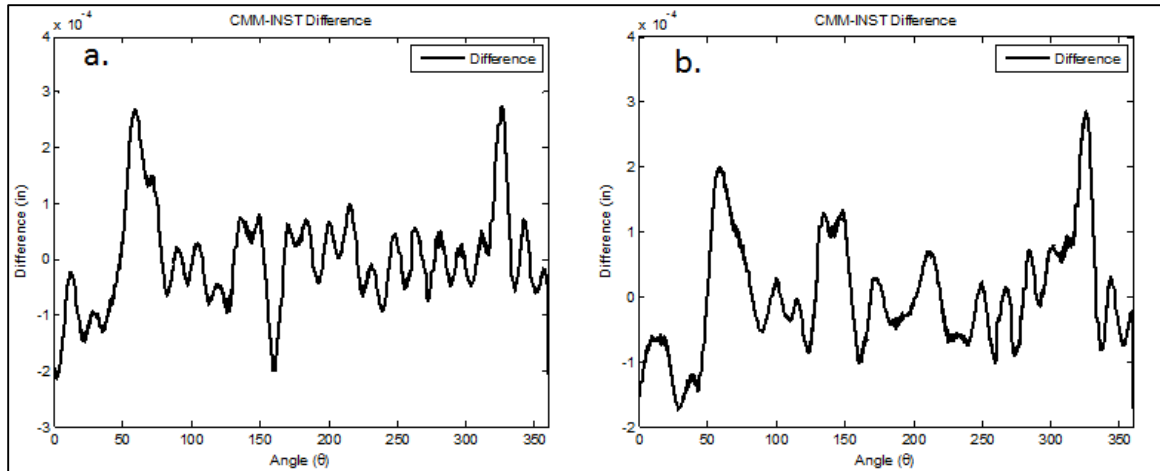
FIGURE 78: Point-to-point difference between CMM and measuring instrument profiles, aluminum plate, a.) measurement one and b.) measurement two

FIGURE 79 and FIGURE 80 shows the measuring instrument measured surface profile compared to the CMM measured surface profile and the point-to-point difference between the two profiles, for the aluminum ring, for each measurement, respectively.
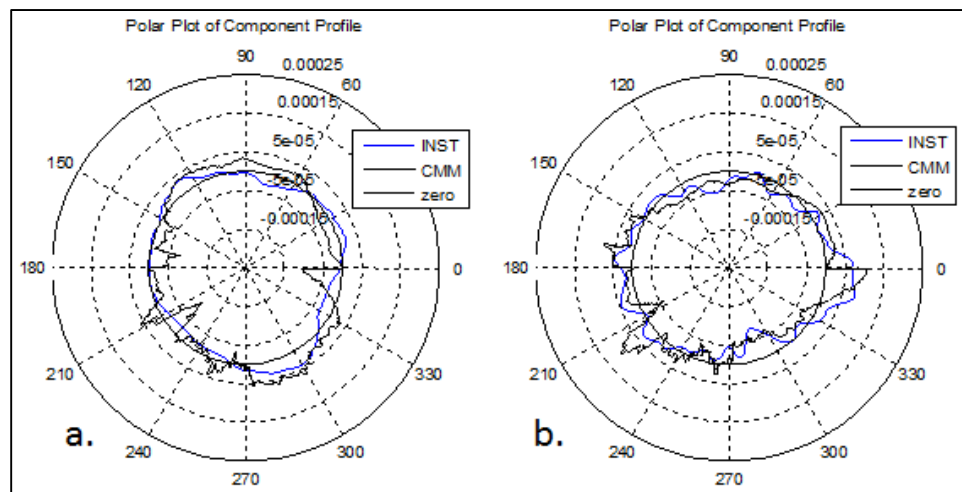
FIGURE 79: CMM and measuring instrument component profile comparison, aluminum ring, a.) measurement one and b.) measurement two
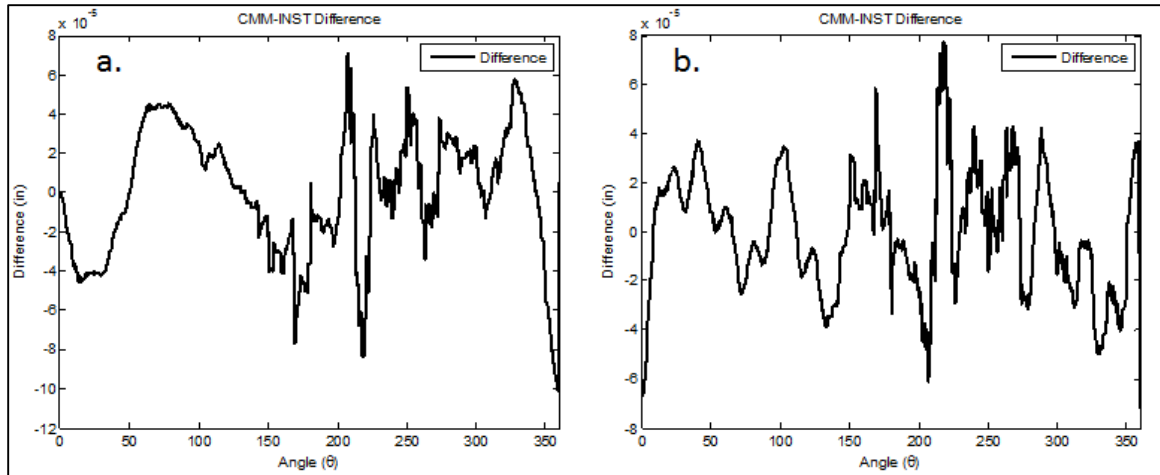
FIGURE 80: Point-to-point difference between CMM and measuring instrument profiles, aluminum stock, a.) measurement one and b.) measurement two

FIGURE 81 and FIGURE 82 shows the measuring instrument measured surface profile compared to the CMM measured surface profile and the point-to-point difference between the two profiles, for the aluminum stock, for each measurement, respectively.
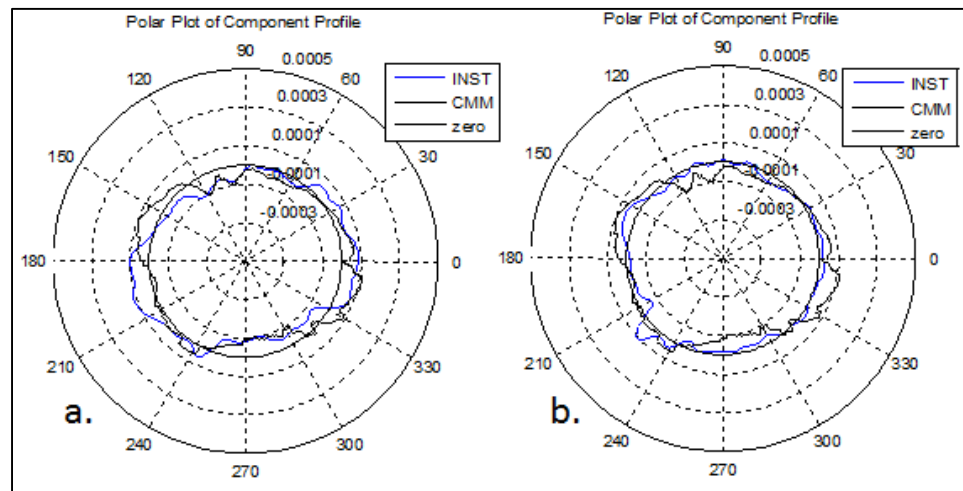
FIGURE 81: CMM and measuring instrument component profile comparison, aluminum stock, a.) measurement one and b.) measurement two
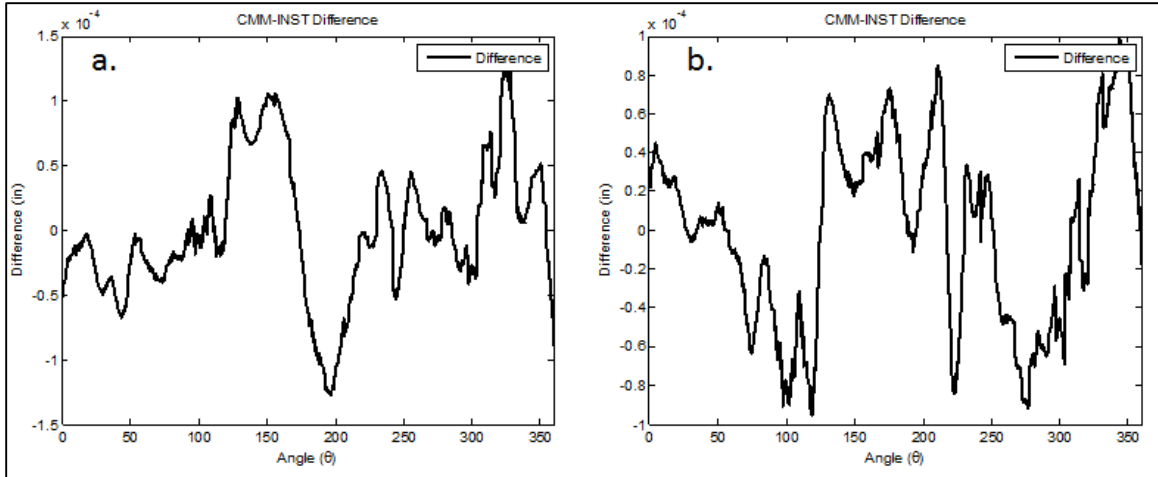
FIGURE 82: Point-to-point difference between CMM and measuring instrument profiles, aluminum stock, a.) measurement one and b.) measurement two

From the previous figures, the CMM and the measuring instrument produce similar shapes, of the same component under test. From FIGURE 78, FIGURE 80 and FIGURE 82, the error bands of the measuring instrument and the CMM measurements for each component can be determined.

TABLE 10: Error band of difference between the CMM and measuring instrument profiles

Component	MAX	MIN	Measurement
Aluminum Plate	0.0063 mm (0.00025")	-0.0051 mm (-0.00020")	1
	0.0063 mm (0.00025")	-0.0043 mm (-0.00017")	2
Aluminum Ring	0.0018 mm (0.00007")	-0.0023 mm (-0.00009")	1
	0.0019 mm (0.00008")	-0.0015 mm (-0.00006")	2
Aluminum Stock	0.0026 mm (0.00014")	-0.0030 mm (-0.00012")	1
	0.0025 mm (0.00010")	-0.0023 mm (-0.00009")	2

These results show that the measuring instrument is capable of measuring a similar component profile as the CMM.

The CMM and measuring instrument do not perfectly match up, and this may be caused by numerous sources. The rotary table used in testing can add in some error, since it is not designed as stiff as a machine tool spindle. Only 25 UPR are used in the Fourier series for approximating the form error results, but this is done because high UPR numbers would include more of the inherent errors in the machining process in the result and that result would be better suited for spindle error motions. The main concern in this research is the component form error, and diameter, so the low number of UPR is acceptable for the testing.

The possible error source that is of most concern, is the suppression of harmonic content. It is stated in the literature, [1] [19] [35] [36], that if the planar angles are not chosen precisely, loss of harmonic content is apparent. The arm angles of the measuring instrument are dependent on the size of the component being measured and the distance from the measuring instrument to the component; so there is no way for optimized angles to be consistently used during in-process measurements.

To fully characterize the form error of the components under test, the form error value from the measuring instrument will be compared to the CMM form error value. The scalar values for the form error of each component is determined using the Minimum Radial Separation (MRS) method (*ASME/B89.3.4* [18]). The form error peak-to-valley results from the measuring instrument and CMM are presented for comparison. TABLE 11 shows the peak-to-valley values of the measuring instrument and CMM for the aluminum plate, for each measurement.

TABLE 11: Peak-to-valley form error values for CMM and measuring instrument, aluminum plate, a.) measurement one and b.) measurement two

a.

UNCC	Max Value	Min Value	Out-of-Roundness
MP (INST)	0.00026"	-0.00029"	0.00055"
	0.0066mm	-0.0074mm	0.0140mm
CMM	0.00033"	-0.00030"	0.00063"
	0.0083mm	-0.0075mm	0.0160mm

b.

UNCC	Max Value	Min Value	Out-of-Roundness
MP (INST)	0.00023"	-0.00024"	0.00047"
	0.0058mm	-0.0060mm	0.0120mm
CMM	0.00033"	-0.00030"	0.00063"
	0.0083mm	-0.0075mm	0.0160mm

TABLE 12 shows the peak-to-valley values of the measuring instrument and CMM for

the aluminum ring, for each measurement.

TABLE 12: Peak-to-valley form error values for CMM and measuring instrument, aluminum ring, a.) measurement one and b.) measurement two

a.

UNCC	Max Value	Min Value	Out-of-Roundness
MP (INST)	0.00005"	-0.00004"	0.00009"
	0.0013mm	-0.0010mm	0.0023mm
CMM	0.00007"	-0.00012"	0.00019"
	0.0018mm	-0.0030mm	0.0048mm

b.

UNCC	Max Value	Min Value	Out-of-Roundness
MP (INST)	0.0009"	-0.00009"	0.00018"
	0.0023mm	-0.0023mm	0.0046mm
CMM	0.00007"	-0.00012"	0.00019"
	0.0018mm	-0.0030mm	0.0048mm

TABLE 13 shows the peak-to-valley values of the measuring instrument and CMM for the aluminum stock, for each measurement.

TABLE 13: Peak-to-valley form error values for CMM and measuring instrument, aluminum stock, a.) measurement one and b.) measurement two

a.

UNCC	Max Value	Min Value	Out-of-Roundness
MP (INST)	0.00011"	-0.00010"	0.00021"
	0.0028mm	-0.0025mm	0.0053mm
CMM	0.00011"	-0.00011"	0.00022"
	0.0028mm	-0.0028mm	0.0056mm

b.

UNCC	Max Value	Min Value	Out-of-Roundness
MP (INST)	0.00011"	-0.00007"	0.00018"
	0.0028mm	-0.0018mm	0.0046mm
CMM	0.00011"	-0.00011"	0.00022"
	0.0028mm	-0.0028mm	0.0056mm

These results show that the measuring instrument is capable of measuring the surface profile form errors of a large-scale component with reasonable accuracy. The multi-probe method, proven in a laboratory environment, has shown its capabilities, with good precision, to measure large-scale components, in a non-controlled environment.

5.4.2. Diameter Results

The diameter of each component under test is calculated from the averaged angular data. This average data has thousands of points, thus there are thousands of diameters calculated; so the best way to represent the data of each component when it is rotated, is the averaged diameter. Using the algorithms from section 3.2, and the averaged angular data, the diameter can now be calculated for each component. As mentioned earlier, each component is measured twice, incremented about $50.8\ mm$ ($2''$) in the negative x direction of the measuring instrument coordinate system, which can be referred to FIGURE 61. The diameter measurements from the measuring instrument are compared to the same component measured on the CMM. TABLE 14 and TABLE 15 show the diameter results in inches and millimeter, respectively.

TABLE 14: Diameter results from measuring instrument compared to CMM measurements (unit = inch.)

Diameter	Meas. Instr.	CMM	Difference	Measurement
Aluminum Plate	19.49784	19.49740	0.00044	1
	19.49652	19.49740	-0.00088	2
Aluminum Ring	10.05141	10.05122	0.00019	1
	10.05089	10.05122	-0.00033	2
Aluminum Stock	3.98827	3.98774	0.00053	1
	3.98687	3.98774	-0.00087	2

TABLE 15: Diameter results from measuring instrument compared to CMM measurements (unit = mm.)

Diameter	Meas. Instr.	CMM	Difference	Measurement
Aluminum Plate	495.2451	495.2340	0.0111	1
	495.2117	495.2340	-0.0223	2
Aluminum Ring	255.3058	255.3011	0.0047	1
	255.2927	255.3011	-0.0084	2
Aluminum Stock	101.3020	101.2886	0.0134	1
	101.2665	101.2886	-0.0221	2

From TABLE 14 and TABLE 15, it can be seen that the diameter results from the components under test are comparably close to the CMM measured values. The largest diameter difference, for the three components, from the measuring instrument measured diameter to the CMM measured diameter is approximately $-0.0223\ mm\ (-0.00088")$, from the aluminum plate, and the smallest diameter difference is approximately $0.0048\ mm\ (0.00019")$ from the aluminum ring.

It is noticed that there is a difference between each of the two measurements of each of the components measured. For the aluminum plate, the difference in diameter measured from measurements one to two is $0.0334\ mm\ (0.0013")$, the aluminum ring from measurement one to two is $0.0131\ mm\ (0.00052")$ and the aluminum stock from measurement one to two is $0.0355\ mm\ (0.0014")$. One issue may be a misalignment of the measuring instrument arms along the same plane on the component. Another difference in the measured values can potentially be attributed to the environment in which the measurements are made. The measuring instrument's kinematic parameters were measured in an environmentally-controlled room of $20 \pm 0.5\text{℃}\ (68 \pm 0.5\text{°F})$. The measurements were taken outside of the environmentally controlled room at approximately $20.61\text{℃}\ (69.1\text{°F})$. These differences in temperature will result in changes in the kinematic parameters and contribute to the measurement error. The coefficients of thermal expansion (CTE) differ by a factor of two, from steel to aluminum for the measuring instrument and components, respectively. The uncertainty in these environmental factors will be quantified in a later section, but the current results verify, though with a lower accuracy than anticipated, that the measuring instrument is capable of measuring the diameter of a component.

The measuring instrument is also tested to see how well it can measure larger diameters than $508\ mm$ $(20″)$, which is a more common occurrence in large industrial manufacturing plants. No large diameter artifacts were available for testing so the next option was to create "virtual" disk components. The virtual disk components will be able to simulate larger diameters without the need to purchase a large component and can be assembled with available items in the shop setting. Refer back to FIGURE 59 for setup of the virtual disk tests and FIGURE 60 for the measuring instrument setup.

From FIGURE 59 and FIGURE 60, the rotary table rotates the bar and bearing ring to different positions, where the arm from the measuring instrument contacts the bearing ring. This max angle the arm reads during contact is recorded. After the max angle is recorded, the bar stock and bearing ring are locked in position with a lock on the rotary table and the CMM is used to measure the position of the bearing ring. The max angle measurement and CMM position measurement are done for arms two and three also. FIGURE 83 shows a schematic of the arm angles and incrementing of the measuring instrument.
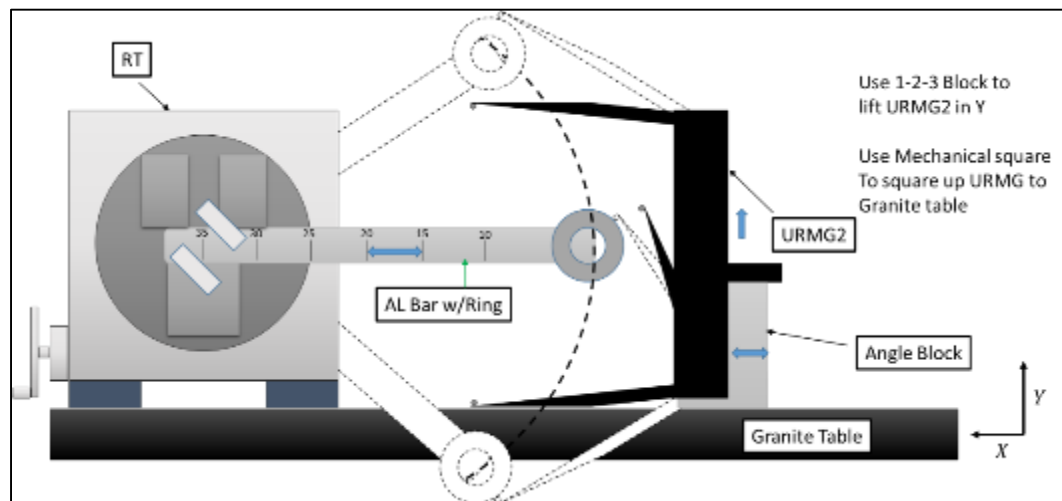
FIGURE 83: Large-scale virtual disk arm angles positions

When all angles are collected, the algorithms in section 3.2 are used to calculate the diameter of the virtual disk. The diameter of the bar stock/bearing ring is computed with a least square fit, with the radius of the bearing ring added to the least square result, to represent the radius of the bar stock/bearing ring at the surface and not the center of the bearing ring. The max arm angles and position of the bar stock/bearing ring are measured for the diameter ranges of $508\ mm - 1778\ mm\ (20" - 70")$. For the diameters of $508\ mm, 1016\ mm, 1270\ mm, 1778\ mm\ (20", 40", 50", 70")$ the measuring instrument body is approximately positioned $50.8\ mm\ (2")$ from the bar stock/bearing ring, in the x direction of the measuring instrument coordinate system. For diameters of $762\ mm, 1524\ mm\ (30", 60")$, the measuring instrument is incremented by $76.2\ mm, 50.8\ mm, 25.4\ mm\ (3", 2", 1")$, from the measuring instrument body, in the x direction of the measuring instrument coordinates system. The measuring instrument is also placed on a $1 - 2 - 3$ block, to change the y position, for the $762\ mm, 1524\ mm\ (30", 60")$, range of diameter. FIGURE 83, shows the schematic of the measuring instrument incremented in both the x and y directions. The results from the virtual disk measurements are as follows:

TABLE 16: Virtual disk results from measuring instrument and CMM (unit = in.)

Diameter	70"	60" (3")	60" (2")	60" (1")	50"
Meas. Instr.	69.5925	59.8537	59.8534	59.8532	49.8912
CMM (LS)	69.5988	59.8589	59.8587	59.8587	49.8970
Difference	-0.0064	-0.0052	-0.0052	-0.0055	-0.0058
Diameter	40"	30" (3")	30" (2")	30" (1")	20"
Meas. Instr.	40.1826	30.0114	30.0113	30.0112	20.0243
CMM (LS)	40.1872	30.0148	30.0148	30.0147	20.0267
Difference	-0.0045	-0.0035	-0.0035	-0.0036	-0.0024

TABLE 17: Virtual disk results from measuring instrument and CMM (unit = mm.)

Diameter	1778mm	1524mm (76.2mm)	1524mm (50.8mm)	1524mm (25.4mm)	1270mm
Meas. Instr.	1767.6483	1520.2850	1520.2767	1520.2720	1267.2363
CMM (LS)	1767.8097	1520.4159	1520.4100	1520.4118	1267.3841
Difference	**-0.1614**	**-0.1309**	**-0.1333**	**-0.1398**	**-0.1478**
Diameter	1016mm	762mm (76.2mm)	762mm (50.8mm)	762mm (25.4mm)	508mm
Meas. Instr.	1020.6388	762.2883	762.2872	762.2833	508.6173
CMM (LS)	1020.7537	762.3765	762.3765	762.3743	508.6776
Difference	**-0.1149**	**-0.0882**	**-0.0893**	**-0.0910**	**-0.0603**

The results show that the measuring instrument is consistently measuring the virtual disks small compared to the CMM measured data. There can be several reasons for the measuring instrument to be deviating from the CMM value.

It was noticed that when determining the max arm angles, once it was reached, the angle tended to fluctuate. The rotary table has a locking latch, but even with the table locked in place, the arm angle could still change. Also when the spring was engaged on the arm, the angle would change. Finding the max arm angle proved to be more of an approximation.

A test was done to see how well the rotary table returns back to its original position. The rotary table was rotated in 45^0 increments, starting at 0^0 and returning back to 0^0, and the centerbore of the rotary table and bearing ring were measured at each position. Back at its original position, the centerbore moved about $0.004 \, mm$ (0.00016″) in x and $0.007 \, mm$ (0.00028″) in y. FIGURE 84 shows the centerbore data.
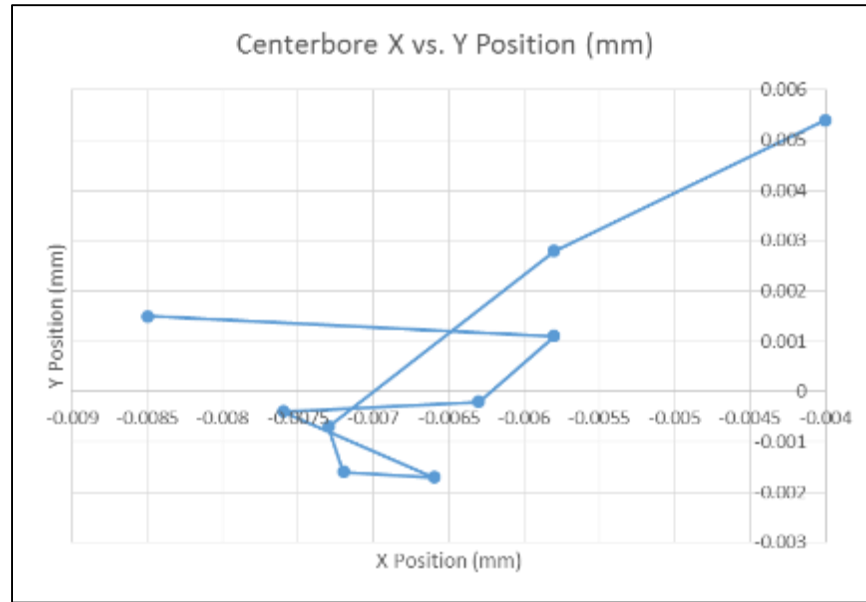
FIGURE 84: X and Y centerbore position

FIGURE 84 shows that the centerbore does not return to its original position after a full rotation and is more than likely due to insufficient stiffness in the setup and the force required to actuate the table. The centerbore to bearing ring distance varies by about $0.003\ mm$ ($0.00012''$), which is consistent with the CMM capabilities. The arms not moving in the same plane can have an effect on the diameter.

Overall, the measuring instrument showed it has the capabilities to measure diameters and from error simultaneous, however, with a lower accuracy than anticipated.

CHAPTER 6: UNCERTAINTY ANALYSIS

6.1. Measurand of Measuring Instrument

The measurands of the measuring instrument will consist of both the form error and diameter measurements. The definition of the form error measurand is the form error value at discrete angular points around the circumference of the component. The definition of the diameter measurand is the average diameter value of the component. The diameter can be calculated by any three points on the component, but since the component is rotated on the rotary table, diameter values are produced as the same length of the number of points collected around the circumference of the component. For example, if there are 1000 points collected around the circumference of the component, there will be 1000 diameter measurements, so an average value is used to determine the diameter of the component. However, for the large virtual diameters, the measurand will be the three-point diameter value and not an average.

With the measurands defined, the uncertainty sources, distributions, types, divisors (factors) and standard uncertainties can be determined. When all standard uncertainties are determined, for both form error and diameter, they will all be combined in the root-sum-squared (RSS) method and multiplied by a coverage factor, $k = 2$ for a 95% confidence interval, for each measurand. Each measurands uncertainty analysis will be compiled into an uncertainty budget, using methods from *Guide to the Expression of Uncertainty in Measurement* [14].

Most of the uncertainty sources for the measuring instrument will affect both the form error measurand and diameter measurand. Section 6.2 covers sources affecting the form error measurand, section 6.3 covers sources affecting the diameter and section 6.4 covers sources for both measurands.

6.2. Form Error Uncertainty Sources

The measuring instrument measures the form error of the component with the multi-probe method described in section 2.1. Recently published work on the uncertainty sources of the multi-probe error separation method [5], covers the uncertainty in the determination of the planar angles needed for the method to work correctly and how incorrect choices of planar angles affects the separation methods results. Further research [15] finds that with large error in the planar angle location, Eq. (27) can become ill-conditioned and harmonic content can become suppressed, the determinant of the matrix will be near zero and reconstruction of the surface profile will be incorrect.

6.2.1. Planar Angle Location

The planar angles are normally pre-determined through simulation and chosen to produce the lowest harmonic suppression and variation. The measuring instrument's planar angles cannot be determined before-hand, because they change with different diameter sizes and different x direction positions as the measuring instrument is incremented into or out of the component. However, the multi-probe method can work reasonably well, as long as the planar angles are asymmetric to one another, as previously shown in section 5.4.1.

To look at what effect the planar angle location has on the form error measurement, the variation in the point-to-point difference between each component's two form error measurements (with different arm angles) is used to determine the uncertainty associated with variation in probe angular positions. These values can be seen in section 5.4.1, FIGURE 76. To quantify the uncertainty, the standard deviation of the point-to-point difference is determined for each component's measurements. The average of the standard deviation of the three component point-to-point differences is determined and is used to determine the uncertainty in the planar angle location.

TABLE 18: Point-to-point standard deviation of each component profile form errors

Component	P-to-P Standard Devaition
Aluminum Plate	0.0011 mm (0.000043")
Aluminum Ring	0.0008 mm (0.000030")
Aluminum Stock	0.0015 mm (0.000060")

The type is A, the distribution is assumed normal, with a divisor of 1. The standard uncertainty in the planar angle locations from the average standard deviation of the point-to-point difference is $0.001\ mm$ (0.00004").

6.2.2. Form Error Repeatability

The repeatability of the form error measurement is evaluated by measuring the aluminum plate five times. The aluminum plate is chosen because it has the worst form error. The component is rotated, measured, the arms are released and then the measuring instrument is moved away from the component, then the measuring instrument is placed back again in the original setup and measured again. This is done until five total measurements are collected. The arm angles from the first measurement are noted and the physical position of the measuring instrument is marked on the granite, so that the following four measurements are taken in approximately the same position. The same measurements are used to determine the diameter uncertainty in section 6.3. FIGURE 85 shows an example of the setup.
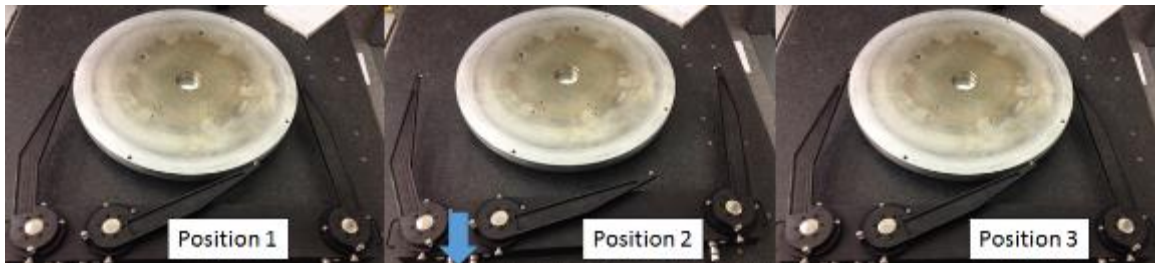
FIGURE 85: Repeatability setup for determining form error and diameter uncertainties

FIGURE 86 shows the form error measurement repeatability and point-to-point difference.
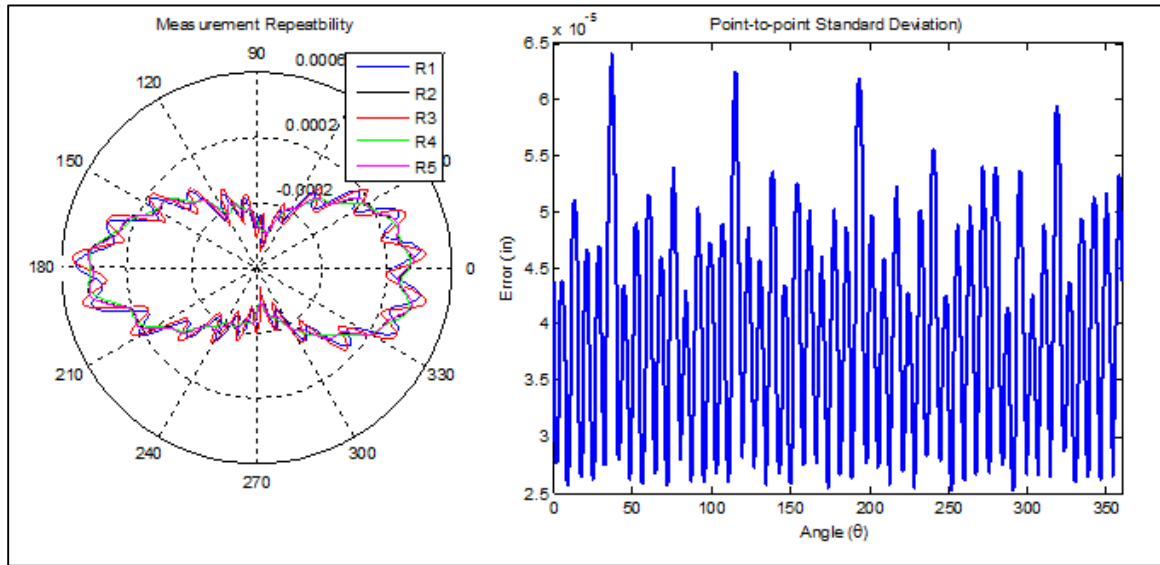
FIGURE 86: Form error repeatability and point-to-point difference

The form error repeatability measurement results are determined from statistical methods, so a type A, normal distribution is assumed for the standard uncertainty, with a divisor of 1. From the five form error measurements, the range of the point-to-point standard deviation between the five measurements is used as the uncertainty in the repeatability of the form error. The standard uncertainty of the repeatability is 0.00091 mm (0.000036").

6.3. Diameter Uncertainty Sources

Sources such as the kinematic parameters of the measuring instrument or the contact sphere radius can affect the uncertainty in the measured average diameter values. These sources of uncertainty as well as the diameter measurement repeatability will be discussed in the following sections. The uncertainty sources affecting the diameter are determined, then used to test the sensitivity of the measured results to these sources. The error sources are varied by the uncertainty value and the resulting diameter is compared to the non-varied measured diameter. The diameter difference divided by the amount of variation of the error source is used to establish the sensitivity of the measurand to the error source.

6.3.1. Kinematic Parameter

As shown in chapter 4, the measuring instrument kinematic parameters are needed to reconstruct the diameter from the raw arm angle data. The kinematic parameters for the measuring system are measured on a high-precision CMM, and the method for measuring on the CMM is explained in section 5.2. The CMM measured kinematic parameters have uncertainty which can be determined through the maximum permissible error (MPE) of the CMM [63]. If the assumption that all values are equally probable, a type B uniform distribution is assumed, and the uncertainty of the CMM measurements is the MPE divided by $\sqrt{3}$, thus $u_{CMM} = \frac{MPE}{\sqrt{3}}$ [63]. The MPE for the CMM is equal to $2.3 + 0.0025L$, where L is in millimeters (mm), but the MPE is in units of micrometers (μm). This MPE is from manufacture specifications. This uncertainty can be used directly for the kinematic parameters that are unit of length.

For the unit length kinematic parameter uncertainty, the measured values needed for the CMM uncertainty are expressed in section 5.2. TABLE 19 shows the standard uncertainty values for the length kinematic parameters, using the u_{CMM}, approximation. $X_C \equiv 0$, so the uncertainty in it will not be considered.

TABLE 19: Standard uncertainty values for length kinematic parameters

KP's	in	mm
L_1	0.0001	0.0019
L_2	0.0001	0.0018
L_3	0.0001	0.0019
X_B	0.0001	0.0013
Y_B	0.0001	0.0015
Y_C	0.0001	0.0021

To determine the uncertainty of the angle offsets relative to the diameter measurements, from section 5.2, the angle offsets were determined by finding the difference between the CMM measured angle and encoder module angles. Each arm is measured in five different arcs, so this produces five different angle offset values for each parameter. Since the angle offsets kinematic parameters are averaged, the standard uncertainty of the mean, $\frac{s}{\sqrt{n}}$, can be used for the uncertainty in the angle offset kinematic parameters. TABLE 20 shows the standard uncertainty values for the angle offset.

TABLE 20: Standard uncertainty values for angle offset kinematic parameters

KP's	$\theta_{1,off}$	$\theta_{2,off}$	$\theta_{3,off}$
deg	0.00029	0.00200	0.00090
rad	0.00001	0.00003	0.00002

Now that the uncertainty in the kinematic parameters are expressed, they will be used to see how sensitive the diameter measurements are to these uncertainties. Each measured CMM kinematic parameter is varied by its standard uncertainty, one at a time; and the resulting diameter is computed. The diameter difference is divided by the amount of variation of the parameter and is the estimate of the sensitivity of the measurand to the error source. TABLE 21 shows the resulting sensitivity of the diameter to each of the kinematic parameters for both the $508\ mm$ (20″) and$1778\ mm$ (70″) diameters.

TABLE 21: Sensitivity coefficients of each kinematic parameter to the diameter measurement, a.) $508\ mm$ (20″) , b.) $1778\ mm$ (70″)

a.

KP's	Sen. Coeff.
L_1	0.0436
L_2	0.0157
L_3	0.3091
X_B	0.1201
Y_B	0.1961
Y_C	1.1706
$\theta_{1,off}$	0.2668
$\theta_{2,off}$	0.0471
$\theta_{3,off}$	0.2873

b.

KP's	Sen. Coeff.
L_1	0.9576
L_2	2.2400
L_3	1.3082
X_B	1.1811
Y_B	8.8688
Y_C	3.7989
$\theta_{1,off}$	0.0000
$\theta_{2,off}$	0.0000
$\theta_{3,off}$	0.0000

Now with sensitivities and the variations determined, TABLE 19 and TABLE 20, the uncertainty in the diameter, due to the kinematic parameters, can be estimated by using the law of propagation of uncertainty. The model is as follows:

$$u^2(D) = \left(\frac{\delta D}{\delta L_1}\right)^2 u^2(L_1) + \left(\frac{\delta D}{\delta L_2}\right)^2 u^2(L_2) + \left(\frac{\delta D}{\delta L_3}\right)^2 u^2(L_3)$$

$$+ \left(\frac{\delta D}{\delta X_B}\right)^2 u^2(X_B) + \left(\frac{\delta D}{\delta Y_B}\right)^2 u^2(Y_B) + \left(\frac{\delta D}{\delta Y_C}\right)^2 u^2(Y_C)$$

$$+ \left(\frac{\delta D}{\delta \theta_{1,off}}\right)^2 u^2(\theta_{1,off}) + \left(\frac{\delta D}{\delta \theta_{2,off}}\right)^2 u^2(\theta_{2,off})$$

$$+ \left(\frac{\delta D}{\delta \theta_{3,off}}\right)^2 u^2(\theta_{3,off})$$

(66)

Taking the square-root of Eq. (66) gives a standard uncertainty in the diameter result from the kinematic parameters as $0.0076\ mm$ ($0.0003''$) for the $508\ mm$ ($20''$) and $0.0165\ mm$ ($0.00065''$) for the $1778\ mm$ ($70''$).

6.3.2. Diameter Repeatability

To test the repeatability of the diameter measurement, the aluminum plate is measured five times. The setup is the same as that for the form error, the plate is rotated, measured, the arms are released and then the measuring instrument is moved away from the component, then the measuring instrument is placed back again in the original setup and measured again. This is done until five total measurements are collected. The arm angles from the first measurement are noted and the physical position of the measuring instrument is marked on the granite, so that following four measurements are taken in approximately the same position. FIGURE 85 shows an example of the setup.

The measured values for the diameter measurements from the five measurements are seen in TABLE 22.

TABLE 22: Measurement values for diameter repeatability

in	mm
19.49789	495.24649
19.49752	495.23706
19.49755	495.23782
19.49747	495.23578
19.49761	495.23929

The diameter repeatability measurement results are determined from statistical methods, so a type A, normal distribution is assumed for the standard uncertainty and the divisor is 1. From the five diameter measurements, standard deviation between the five average diameter measurements is used as the standard uncertainty in the repeatability of the diameter. However, since the diameter value is an average, then the more appropriate standard uncertainty would be that of the mean. The standard uncertainty of the mean can be determined by $u_{\bar{D}} = \frac{s}{\sqrt{n}}$, where s is the standard deviation and n is the number of measurements. For n equal to five and s equal to $0.0048\ mm$ $(0.00019")$, so the standard uncertainty of the mean diameter is $0.002\ mm$ $(0.00008")$. This uncertainty is also used for the $1778\ mm$ $(70")$ diameter because that measurement was not repeated due to lack of available resources.

6.3.3.   Contact Sphere

The three-point diameter calculation finds the diameter of a circle passing through the centers of the three contact spheres. To obtain the component diameter, the contact sphere radius is subtracted from the three-point diameter result to obtain the actual measured component diameter. The contact spheres are made of stainless steel and the error of the surface profile of the sphere is assumed negligible to the diameter error of the sphere. The manufacture of the contact sphere, Bal-tec, states an uncertainty of $\pm 0.001\ mm$ ($\pm 0.00004"$) in the diameter of the ball. It is assumed the distribution is uniform with a divisor of $\sqrt{3}$. Thus the uncertainty in the contact sphere, from manufacture specification is $\pm 0.00058\ mm$ ($\pm 0.000023"$). The uncertainty the contact sphere has on the diameter measurements is found by determining the sensitivity of the measured result by varying the contact sphere radius by the stated uncertainty and comparing the two results and using the difference as the uncertainty. The average diameter is $495.2116\ mm$ ($19.49652"$) and contact sphere radius uncertainty induced averaged diameter is $495.2103\ mm$ ($19.49647"$). The difference is $0.00127\ mm$ ($0.00005"$), this value is the standard uncertainty for the $508\ mm$ ($20"$). The large diameter is $1767.648\ mm$ ($69.59245"$) and contact sphere large radius uncertainty induced diameter is $1767.647\ mm$ ($69.59241"$). The difference is $0.00127\ mm$ ($0.00005"$), this value is the standard uncertainty for the $1778\ mm$ ($70"$).

6.4. Sources Affecting Form Error and Size

There are several uncertainty sources that affect both the form error and diameter measurements from the measuring instrument. Likely sources of uncertainty for both measurands are:

- Hysteresis

- Encoder noise

- Encoder module eccentricity due to bearings

- Encoder sensitivity (including resolution and accuracy)

- Measurement plane misalignment

- Arm bending due to contact load

- Operator influence

- Environmental factors

The uncertainty in these sources are determined and then used to check how sensitive the measured result is to these uncertainties for both form error and diameter measurement results. The uncertainty will be evaluated for both diameter sizes and only form error for the smaller diameter.

6.4.1. Hysteresis

The hysteresis error from the measuring instrument can be seen in section 5.1.2, however, the uncertainty in the measurement needs to be determined. To determine the hysteresis uncertainty in the measuring instrument, the values from TABLE 4 are converted to represent the hysteresis at the end of the arm motion. This can be done using Eq. (63). TABLE 23 shows the arm end hysteresis.

TABLE 23: Hysteresis values at arm end

Hysteresis	
Arm 1	0.0018 mm (0.00007")
Arm 2	0.0001 mm (0.000005")
Arm 3	0.0013 mm (0.00005")

To see how the hysteresis uncertainty affect both the form error and diameter, these uncertainty values will be used to vary the measured results from the aluminum plate, since it has the worst diameter and form error. The virtual disk is used for the large diameter. The difference between the varied and non-varied results will be used for the uncertainty in the diameter and form error.

The average diameter is $495.2116\ mm\ (19.49652")$ and the hysteresis uncertainty induced averaged diameter is $495.5086\ mm\ (19.4964")$. The difference is $0.003\ mm\ (0.00012")$, this value is the standard uncertainty for diameter. The large diameter is $1767.6482\ mm\ (69.59245")$ and the hysteresis uncertainty induced large diameter is $1767.7651\ mm\ (69.59257")$. The difference is $0.003\ mm\ (0.00012")$, this value is the standard uncertainty for diameter.

The peak-to-valley form error of the aluminum plate is $0.01397\ mm\ (0.00055")$ and the hysteresis uncertainty induced peak-to-valley form error is $0.01410\ mm\ (0.000557")$. The difference is $0.00018\ mm\ (7x10^{-6}")$, this value is the standard uncertainty in the form error. The form error is almost negligible from the hysteresis, while the diameter is affected slightly.

6.4.2. Encoder Noise

The noise from the measuring instrument is determined from the encoder noise and the noise from the encoders are determined from the manufacturer's specifications [64]. The manufacture specifies a root-mean-square (RMS) noise of $0.037\ arc-\sec\ (0.00001^{\circ})$. It is assumed the distribution is normal, but that there is a 95% confidence in the stated noise, so the value in the specification is divided by two. The uncertainty from noise of the encoder from manufacture specification is $0.0185\ arc-\sec\ (0.000005^{\circ})$. These values are converted by Eq. (63), to get the noise of the end motion of the arm. TABLE 24 shows the encoder noise from the arm end.

TABLE 24: Encoder noise from arm end motion

Encoder Noise	
Arm 1	0.000032 mm (0.0000013")
Arm 2	0.000025 mm (0.000001")
Arm 3	0.000032 mm (0.0000013")

The uncertainty from the encoder noise is used to see the effects they have on the diameter and form error of the measured results. The aluminum plate is used for both the form error and diameter. The virtual disk is used for the large diameter.

The average diameter is $495.2116\ mm\ (19.49652'')$ and the encoder noise uncertainty induced averaged diameter is $495.21165\ mm\ (19.496522'')$. The difference is $0.00005\ mm\ (0.000002'')$, this value is the standard uncertainty of the diameter. The large diameter is$1767.648\ mm\ (69.59245'')$and the encoder noise uncertainty induced large diameter is $1767.647\ mm\ (69.59244'')$. The difference is $0.00025\ mm\ (0.00001'')$, this value is the standard uncertainty of the diameter.

The peak-to-valley form error of the aluminum plate is $0.01397\ mm$ $(0.00055'')$ and the encoder noise uncertainty induced peak-to-valley form error is $0.013977\ mm$ $(0.0005503'')$. The difference is $0.000007\ mm$ ($3x10^{-7}''$), this value is the standard uncertainty of the form error. The form error is almost negligible from the encoder noise, while the diameter is affected slightly.

<div align="center">6.4.3. Encoder Eccentricity</div>

The encoder modules are a combination of an absolute encoder and a high-precision bearing [64]. From the literature, this integration eliminates the critical mounting of the encoder and all necessary adjustments are made. This solution leads to a smaller deviation of the actual rotational axis of the bearing from the nominal axis (encoder scale) or eccentricity of the module setup. Manufactures specification's states an eccentricity of the bearing as $0.7\ arc-sec''$ $(0.000194°)$. It is assumed the distribution is normal, but that there is a 95% confidence in the stated eccentricity, so the value in the specification is divided by two. The standard uncertainty from manufacture specification is $0.35\ arc-sec(\pm0.000097°)$. This value can be converted to a linear value using Eq. (63), for arm end motion. Conversion of the uncertainty to arm end motion is shown in TABLE 25.

TABLE 25: Arm end encoder eccentricity

Encoder Eccentrcity	
Arm 1	0.00006 mm (0.000025")
Arm 2	0.00005 mm (0.000019")
Arm 3	0.00006 mm (0.000025")

The uncertainty from the encoder eccentricity is used to see the effects they have on the diameter and form error of the measured results. The aluminum plate is used for both the form error and diameter. The virtual disk is used for the large diameter.

The average diameter is $495.2116\ mm$ (19.49652″) and the encoder eccentricity uncertainty induced averaged diameter is $495.2117\ mm$ (19.496525″). The difference is $0.00013\ mm$ (0.000005″), this value is the standard uncertainty for the diameter. The large diameter is $1767.648\ mm$ (69.59245″) and the encoder eccentricity uncertainty induced large diameter is $1767.645\ mm$ (69.59233″). The difference is $0.003\ mm$ (0.00012″), this value is the standard uncertainty for the diameter.

The peak-to-valley form error of the aluminum plate is $0.01397\ mm$ (0.00055″) and the encoder eccentricity uncertainty induced peak-to-valley form error is $0.01399\ mm$ (0.000551″). The difference is $0.000025\ mm$ (0.000001"), this value is the standard uncertainty for the form error. The form error is almost negligible from the encoder eccentricity, while the diameter is affected slightly.

6.4.4. Encoder Sensitivity

The encoder sensitivity is determined through manufacture specifications, which includes the resolution error. The resolution is 28 bits, approximately 268,435,456 counts per revolution. This equates to approximately $0.0000013°$ theoretical resolution. The resolution is small enough that the error in it is negligible to the system accuracy of the encoder module. The system accuracy of the encoder module is measured by a combination of the radial guideway accuracy and the axial guideway accuracy [64]. The radial guideway accuracy is the radial deviation, measured in the x and y directions, from the nominal axis of the bearing when it is rotated. The axial guideway accuracy is axial deviation, measured in the z direction, from the nominal axis of the bearing when it is rotated. The system accuracy is stated as $2.5 \; arc - \sec (0.00069°)$. It is assumed the distribution is normal but that there is a 95% confidence in the stated accuracy, so the system accuracy in the specification is divided by two. The standard uncertainty from manufacture specification is $1.25 \; arc - \sec(0.00035°)$. This value can be converted to a linear value using Eq. (63), for arm end motion. Conversion of the uncertainty to arm end motion is shown in TABLE 26.

TABLE 26: Arm end system accuracy

System Accuracy	
Arm 1	0.0022 mm (0.000087")
Arm 2	0.0017 mm (0.000071")
Arm 3	0.0022 mm (0.000087")

The uncertainty from the system accuracy is used to see the effects they have on the diameter and form error of the measured results. The aluminum plate is used for both the form error and diameter. The virtual disk is used for the large diameter.

The average diameter is $495.2116 \, mm$ $(19.49652'')$ and the encoder eccentricity uncertainty induced averaged diameter is $495.2114 \, m$ $(19.496512'')$. The difference is $0.0002 \, mm$ $(0.000008'')$, this value is the standard uncertainty for diameter. The large diameter is $1767.648 \, mm$ $(69.59245'')$ and the encoder eccentricity uncertainty induced large diameter is $1767.657 \, mm$ $(69.59281'')$. The difference is $0.009 \, mm$ $(0.00036'')$, this value is the standard uncertainty for diameter.

The peak-to-valley form error of the aluminum plate is $0.01397 \, mm$ $(0.00055'')$ and the encoder eccentricity uncertainty induced peak-to-valley form error is $0.0142 \, mm$ $(0.00056'')$. The difference is $0.00025 \, mm$ $(0.00001'')$, this value is the standard uncertainty form error. The system accuracy uncertainty affects the form error peak-to-valley and average diameter measurements about the same for the average diameter.

6.4.5. Measuring Instrument Misalignment

The misalignment of the measuring instrument to the component can add an error into the measurement results. The possible misalignments are the tilt and yaw alignment errors. Also included in the yaw is non-parallelism of the measuring instruments arms, relative to arm one pivot location. A schematic of misalignment can be seen in FIGURE 87.
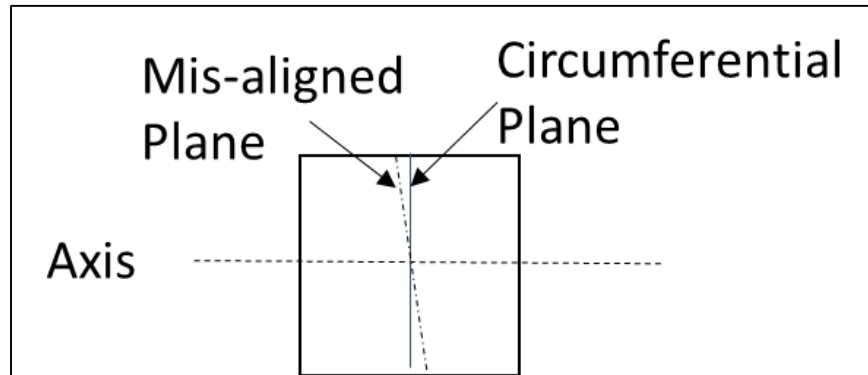
FIGURE 87: Measuring instrument misalignment to components

Normally, the accuracy of alignment for the measuring instrument is controlled by the tool-post mounting. In the testing in this research, the measuring instrument was not mounted in a tool-post, because it could not fit in an available lathe. The assumption is that the tilt and yaw each have a worst-case misalignment error of $\pm 1°$ ($0.017 rad$).

This worst case misalignment causes a $0.0127\ mm$ ($0.0005''$) diameter error for yaw and $0.0508\ mm$ ($0.002''$) diameter error for tilt of a $508\ mm$ ($20''$) diameter measurement, approximately the same size for the aluminum plate. Since the misalignment is plus/minus, a uniform distribution is assumed with a divisor of $\sqrt{3}$. The uncertainty from these errors are $0.007\ mm$ ($0.00029''$) for tilt and $0.029\ mm$ ($0.0012''$) for yaw.

This worst case misalignment causes a $0.062\ mm$ ($0.0024''$) diameter error for yaw and $0.132\ mm$ ($0.0052''$) diameter error for tilt of a $1778\ mm$ ($70''$) diameter measurement. Since the misalignment is plus/minus, a uniform distribution is assumed

with a divisor of $\sqrt{3}$. The uncertainty from these errors are $0.036\ mm$ ($0.0014''$) for tilt and $0.076\ mm$ ($0.003''$) for yaw.

The uncertainty from the misalignments are used to see the effects they have on the diameter and form error of the measured results. The aluminum plate is used for both the form error and diameter. The virtual disk is used for the large diameter.

The average diameter is $495.2116\ mm$ ($19.49652''$) and the tilt and yaw uncertainty induced averaged diameter is $495.2070\ mm$ ($19.49634''$). The difference is $0.0045\ mm$ ($0.000018''$), this value is the standard uncertainty for diameter. The large diameter is $1767.6482\ mm$ ($69.59245''$) and the tilt and yaw uncertainty induced large diameter is $1767.6962\ mm$ ($69.59434''$). The difference is $0.0483\ mm$ ($0.0019''$), this value is the standard uncertainty for diameter.

The peak-to-valley form error of the aluminum plate is $0.01397\ mm$ ($0.00055''$) and the tilt and yaw uncertainty induced peak-to-valley form error is $0.015\ 2mm$ ($0.0006''$). The difference is $0.00127\ mm$ ($0.00005"$), this value is the standard uncertainty if for form error. The misalignment uncertainty affects the average diameter measurements significantly more than the peak-to-valley form error.

6.4.6.   Arm Bending

The measured results from the measuring instrument can be affected by bending of the arms from excess contact force. In section 4.2.4.2, FEA was conducted on the measuring arms to see how much stress and max displacement error would occur when an approximate $\pm 4.44\ N$ ($\pm 1\ lb_f$) was applied to the arm. The results showed an error of $\pm 0.0089\ mm$ ($\pm 0.00035"$) in arm displacement error. The distribution of the error is uniform, type B, with a divisor of $\sqrt{3}$. The standard uncertainty from the arm bend is $0.0051\ mm$ ($0.0002''$). The uncertainty from the arm bend is used to see the effects they have on the diameter and form error of the measured results. The aluminum plate is used for both the form error and diameter. The virtual disk is used for the large diameter.

The average diameter is $495.2116\ mm$ ($19.49652''$) and the arm bend uncertainty induced averaged diameter is $495.2108\ mm$ ($19.49649''$). The difference is $0.0007\ mm$ ($0.00003''$), this value is the standard uncertainty of the diameter. The large diameter is $1767.6482\ mm$ ($69.59245''$) and the arm bend uncertainty induced large diameter is $1767.6815\ mm$ ($69.59376''$). The difference is $0.033\ mm$ ($0.0013''$), this value is the standard uncertainty of the diameter.

The peak-to-valley form error of the aluminum plate is $0.01397\ mm$ ($0.00055''$) and the arm bend uncertainty induced peak-to-valley form error is $0.01432\ mm$ ($0.000564''$). The difference is $0.00036\ mm$ ($0.000014"$), this value is the standard uncertainty for the form error. The arm bend uncertainty affects the form error peak-to-valley slightly less than the average diameter measurements.

6.4.7. Operator Influence

Errors can be introduced by the operator when taking measurements with the measuring instrument. There is a potential that an operator can produce a systematic influence during the measuring of the components [63]. Operator influence has a somewhat random characteristic due to inconsistencies in human behavior and response. The random characteristics of operator influence can be determined from the measurement repeatability. Since there is only one operator of the measuring instrument, the uncertainty from this operator influence should be included in the uncertainty budget. The assumption is that the operator influence works on a type A, normal distribution with a divisor of 1. To estimate the uncertainty in the operator influence, half of the standard uncertainty in the repeatability of both measurands are used as an estimate of the standard uncertainty of the operator influence [63]. The standard uncertainty in the averaged diameter repeatability is $0.002\ mm$ (0.00008"), so the standard uncertainty in the operator influences in is $0.001\ mm$ (0.00004"). This uncertainty is the same for the large diameter since there is not repeatable measurements of the large diameter.

The standard uncertainty in the form error repeatability is $0.00093\ mm$ (0.000036"), so the standard uncertainty in the operator influences in is $0.0005\ mm$ (0.000018").

6.4.8. Environmental Factors

Errors can result from variations in the environmental conditions, such as temperature. Additional errors are introduced when measurement results are corrected for environmental conditions [62] [66] [67]. An example is correcting a diameter for thermal expansion or a form error for thermal expansion. The uncertainty in the correction error is a function of the uncertainty in the error in the thermal expansion. Error models for both diameter and form error are expressed and the uncertainties from the thermal expansion of the measuring instrument, thermal expansion of the component and the temperature, are of main interest.

The effect of temperature deviation from 20°C on the diameter measurement is:

$$\Delta D = D(\alpha_{COM} - \alpha_{INST})\Delta T \qquad (67)$$

Where D is the component diameter, α_{COM} is the coefficient of thermal expansion (CTE) for aluminum components, $\frac{22.2\ ppm}{\cdot°C}$, α_{INST} is the coefficient of thermal expansion (CTE) for steel, $\frac{12.0\ ppm}{°C}$ and ΔT is the ambient temperature (shop-floor) minus the reference temperature, $20.61°C - 20°C = 0.61°C$.

The effect of temperature deviation from 20°C on the form error measurement is:

$$\Delta P_{PtoV} = P_{PtoV}(\alpha_{COM} - \alpha_{INST})\Delta T \qquad (68)$$

Where P_{PtoV} is the peak-to-valley form error value and all other variables are the same as diameter. The error models presented can be used to correct the measured values from sections 5.4.1 and 5.4.2, for temperature effects [63] [66] [67].

With the error model expressed, the uncertainty model can be determined by determining the sensitivity coefficients of the sources and the uncertainty for each source [14] [63]. The models of the sensitivity coefficients are expressed. The sensitivity coefficients for diameter are:

$$c_{1D} = \frac{\partial(\Delta D)}{\partial \alpha_{COM}} = (D)\Delta T$$

$$c_{2D} = \frac{\partial(\Delta D)}{\partial \alpha_{INST}} = -(D)\Delta T, \tag{69}$$

$$c_{3D} = \frac{\partial(\Delta D)}{\partial \Delta T} = (D)(\alpha_{COM} - \alpha_{INST})$$

The sensitivity coefficients for form error are similar:

$$c_{1P} = \frac{\partial(\Delta P_{PtoV})}{\partial \alpha_{COM}} = (P_{PtoV})\Delta T$$

$$c_{2P} = \frac{\partial(\Delta P_{PtoV})}{\partial \alpha_{INST}} = -(P_{PtoV})\Delta T, \tag{70}$$

$$c_{3P} = \frac{\partial(\Delta P_{PtoV})}{\partial \Delta T} = (P_{PtoV})(\alpha_{COM} - \alpha_{INST})$$

No correlation exist between the expansion coefficients and or the temperature difference, so correlation terms are assumed zero. The uncertainty in the dimension changes are expressed as:

$$u_{\Delta D} = \sqrt{c_{1D}^2 u_{\alpha_{COM}}^2 + c_{2D}^2 u_{\alpha_{INST}}^2 + c_{3D}^2 u_{\Delta T}^2} \tag{71}$$

$$u_{\Delta P_{ptov}} = \sqrt{c_{1P}^2 u_{\alpha_{COM}}^2 + c_{2P}^2 u_{\alpha_{INST}}^2 + c_{3P}^2 u_{\Delta T}^2} \tag{72}$$

The uncertainty values in the CTE's are expressed as $u_\alpha = \frac{0.1\alpha}{\sqrt{3}}$, where a type B,

uniform distribution is assumed [66] [67]. The uncertainty in the component's CTE is

$u_{\alpha_{COM}} = \frac{0.1(\frac{22.2\,ppm}{°C})}{\sqrt{3}} = \frac{1.2\,ppm}{°C}$ and uncertainty from the measuring instrument CTE is

$u_{\alpha_{INST}} = \frac{0.1(\frac{12\,ppm}{°C})}{\sqrt{3}} = \frac{0.69\,ppm}{°C}$. The uncertainty in the temperature difference is expressed

as $u_{\Delta T} = \frac{T_{max} - T_{min}}{\sqrt{2}}$, where a type B, U-shaped distribution is assumed, because the

temperature is cyclic in nature [66] [67]. Using the estimate of $T_{max} - T_{min}$ as the range

of temperature values is used for uncertainty because the measuring instrument and

component have been in the same environment for a long duration of time, giving adequate

time for reaching thermal equilibrium with the surroundings. The range is assumed $\pm 2°C$,

so the uncertainty in the temperature difference is $u_{\Delta T} = \frac{2°C}{\sqrt{2}} = 1.41°C$.

Now that all terms are defined, Eq. (71) and Eq. (72) can be expressed with the

available terms. Uncertainty of the diameter due to thermal effects, simplified:

$$u_{\Delta D} = Dx14.394\,ppm \tag{73}$$

Uncertainty of the form error due to thermal effects, simplified:

$$u_{\Delta P} = P_{PtoV}x14.394\,ppm \tag{74}$$

Eq. (73) and Eq. (74) are expressed in part per million (PPM). With PPM stated, now the uncertainty due to thermal effects, can be quantified in units of length. Eq. (73) and Eq. (74) are expressed as a measurement-by-measurement case, so to incorporate this uncertainty in the testing of this research, the worst measured value, compared to the CMM, for average diameter and peak-to-valley form error value will be used in the uncertainty budget. The virtual disk testing from section 5.4.2, are also to be considered for the diameter measurements. From section 5.4.1, the worst peak-to-valley form error value of the components is seen in TABLE 11, which is measurement one of the aluminum plate, $0.014 \, mm$ (0.00055"). From section 5.4.2, the worst average diameter value of the components is seen in TABLE 14, which is measurement two of the aluminum plate, $495.217 \, 7mm$ (19.49652"). From section 5.4.2, the worst large diameter value of the virtual disk is seen in TABLE 16, which is the $1778 \, mm$ (70") diameter, at $1767.6482 \, mm$ (69.59245").

The standard uncertainty in the peak-to-valley form error due to thermal effects, for the worst measured value is $2x10^{-7} \, mm$ ($8x10^{-9}$").

The standard uncertainty in the average diameter due to thermal effects, for worst measured value is $0.0071 \, mm$ (0.00028") for the $508 \, mm$ (20") diameter and the standard uncertainty in the $1778 \, mm$ (70") diameter due to thermal effects is $0.025 \, mm$ (0.00098").

6.5. Measuring Instrument Overall Uncertainty

Now that the uncertainty sources, distributions, type, divisors (factors) and standard uncertainties have been determined, the combined standard uncertainty, as well as the expanded uncertainty, 95% confidence interval, can be expressed individually for the form error and diameter measurements. Methods from the *Guide to the Expression of Uncertainty in Measurement* [14], will be used for calualting the combined and expanded uncertainties.

The best way to express the uncertainty in the measuring process for each measurand is via an uncertainty budget. TABLE 27 shows the uncertainty budget for the measuring instrument's ($508\ mm/20"$) diameter measurement process.

TABLE 27: Uncertainty budget for ($508\ mm/20"$) diameter measurement process (unit = mm)

Uncertainty Component	Dia. Unc.(mm)	Type	Distribution	Factor	Standard Uncertainty (mm)
Kinematic Parameters	0.008	A	Normal	1	**0.008**
Measurement Repeatability	0.002	A	Normal	1	**0.002**
Contact Sphere	0.002	B	Uniform	0.577	**0.001**
Hysteresis	0.003	A	Normal	1	**0.003**
Encoder Noise	0.000	B	Normal	1	**0.000**
Encoder Eccentricity	0.000	B	Normal	1	**0.000**
Encoder Sensitivity	0.000	B	Normal	1	**0.000**
Misalignment	0.008	B	Uniform	0.577	**0.005**
Arm Bend	0.001	B	Uniform	0.577	**0.001**
Operator Influence	0.001	A	Normal	1	**0.001**
Environmental Factors	0.007	B	Normal	1	**0.007**
Combined Standard Uncertainty (RSS) : $u_c(y)$					**0.012**
Expanded Unceraınty (k = 2, 95% Confidence): $U(y)$					**0.024**

From the uncertainty budget, the measuring instrument produces an expanded measurement uncertainty of $0.024\ mm$ (0.00094"), with a 95% confidence level for the $508\ mm$ (20") diameter measurements.

FIGURE 88: Uncertainty source percent contribution for diameter $(508\ mm/20")$ measurements

FIGURE 88 shows the percent contribution of each uncertainty source, relative to the 95% expanded uncertainty, for the $508\ mm$ $(20")$ diameter measurement process. It can be seen that the largest contributions are the environmental factors, misalignment of the measuring instrument and the kinematic parameters. The plot gives a good indication of places to correct errors at in the measuring process.

TABLE 28 shows the uncertainty budget for the measuring instrument's $(1778\ mm/70")$ diameter measurement process.

TABLE 28: Uncertainty budget for diameter ($1778mm/70''$) measurement process (unit = mm)

Uncertainty Component	Dia. Unc.(mm)	Type	Distribution	Factor	Standard Uncertainty (mm)
Kinematic Parameters	0.017	A	Normal	1	**0.017**
Measurement Repeatability	0.002	A	Normal	1	**0.002**
Contact Sphere	0.002	B	Uniform	0.577	**0.001**
Hysteresis	0.003	A	Normal	1	**0.003**
Encoder Noise	0.000	B	Normal	1	**0.000**
Encoder Eccentricity	0.003	B	Normal	1	**0.003**
Encoder Sensitivity	0.009	B	Normal	1	**0.009**
Misalignment	0.083	B	Uniform	0.577	**0.048**
Arm Bend	0.033	B	Uniform	0.577	**0.019**
Operator Influence	0.001	A	Normal	1	**0.001**
Environmental Factors	0.025	B	Normal	1	**0.025**
Combined Standard Uncertainty (RSS) : $u_c(y)$					**0.061**
Expanded Unceraity (k = 2, 95% Confidence): **U(y)**					**0.122**

From the uncertainty budget, the measuring instrument produces an expanded measurement uncertainty of $0.122\ mm$ ($0.0048''$), with a 95% confidence level for the $1778\ mm$ ($70''$) diameter measurements.
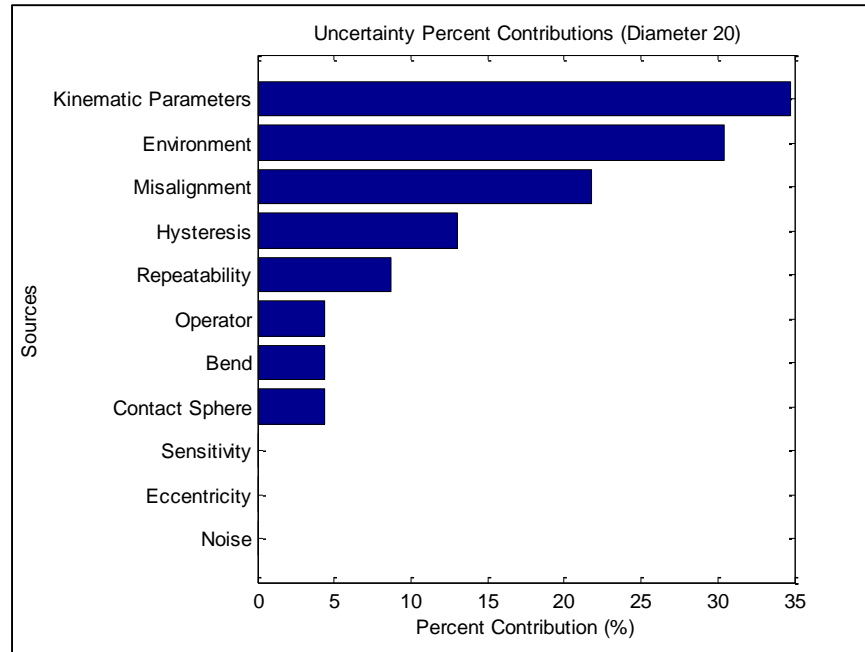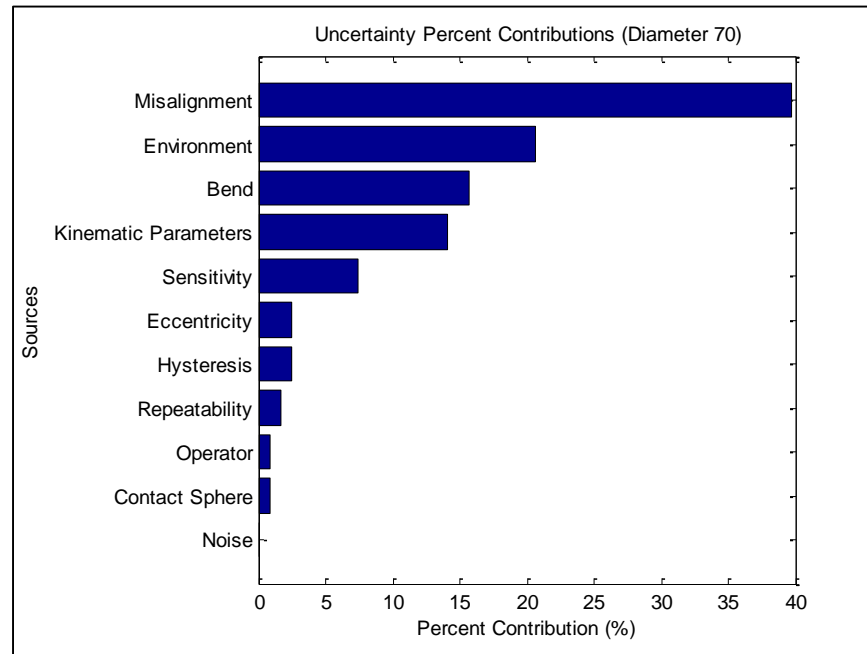

FIGURE 89: Uncertainty source percent contribution for diameter ($1778\ mm/\ 70''$) measurements

FIGURE 89 shows the percent contribution of each uncertainty source, relative to the 95% expanded uncertainty, for the 1778 mm (70″) diameter measurement process. It can be seen that the largest contributions are the misalignment of the measuring instrument, environmental factors, arm bend and the kinematic parameters. This plot give a good indication of places to correct errors at in the measuring process.

TABLE 29 shows the uncertainty budget for the measuring instrument's form error measurement process.

TABLE 29: Uncertainty budget for form error measurement process (unit = mm)

Uncertainty Component	Form Unc. (mm)	Type	Distribution	Factor	Standard Uncertainty (mm)
Planar Angle Location	0.001	A	Normal	1	**0.001**
Measurement Repeatbility	0.001	A	Normal	1	**0.001**
Hysteresis	0.000	A	Normal	1	**0.000**
Encoder Noise	0.000	B	Normal	1	**0.000**
Encoder Eccentricity	0.000	B	Normal	1	**0.000**
Encoder Sensitivity	0.000	B	Normal	1	**0.000**
Misalignment	0.002	B	Uniform	0.577	**0.001**
Arm Bend	0.001	B	Uniform	0.577	**0.000**
Operator Influence	0.000	A	Normal	1	**0.000**
Environmental Factors	0.000	B	Normal	1	**0.000**
Combined Standard Uncertainty (RSS) : $u_c(y)$					**0.002**
Expanded Uncerainty (k = 2, 95% Confidence): $U(y)$					**0.004**

From the uncertainty budget, the measuring instrument produces an expanded measurement uncertainty of 0.004 mm (0.00016″), with a 95% confidence level for the form error measurements.
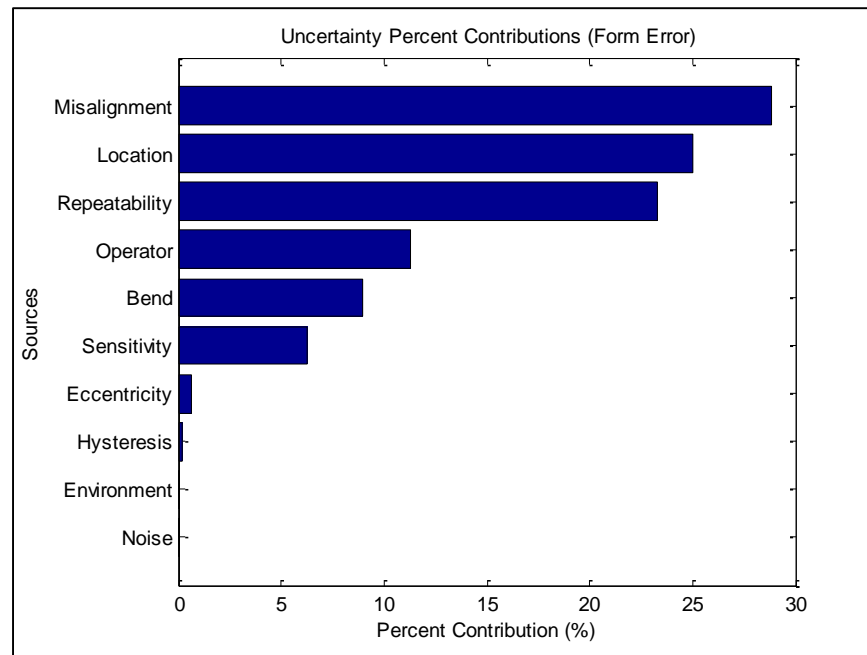
FIGURE 90: Uncertainty source percent contribution for form error measurements

FIGURE 90 shows the percent contribution of each uncertainty source, relative to the 95% expanded uncertainty, for the form error measurement process. It can be seen that the largest contributions are the misalignment of the measuring instrument, planar angle locations and measurement repeatability. The plot give a good indication of places to correct errors at in the measuring process.

CHAPTER 7: CONCLUSIONS AND FUTURE WORK

7.1. Conclusions

This research documents an improved approach to measuring circular component's form errors and diameters, simultaneously, through a novel measurement instrument. Firstly, the form error uses a known error separation method to measure the surface profile form more accurately and precisely then conventional digital indicators, which include spindle error motions in their data. The error separation method also produces a more complete shape of the estimated surface profile. Secondly, the diameter measurements are determined through a geometrical model, using three unique non-collinear points, which are fit to a circle produce a components diameter. Lastly, these more mathematically sound algorithms are implemented through a novel measuring instrument which contacts the surface of a circular component at three points, which can be used for both the form error separation method and geometrical model for the diameter.

The form error results from the measuring instrument produced a max deviation in the form error value, compared to a CMM measurement of the same component, of $0.004\ mm$ (0.00016″). It also produced a max point-to-point error band, compared to the CMM, of $+0.0063\ mm/-0.0051\ mm$ (+0.00025"/-0.00020"). Overall the measuring instrument measured a similar shape to that of the CMM and thus proving it capability for form error measurements in a shop-floor environment.

The diameter results from the measuring instrument produced a max deviation in the diameter value, compared to a CMM measurement of the same component, of $0.022\ mm$ (0.00087″). The large-scale diameter test proved a max deviation, compared to the CMM, of $0.1524\ mm$ (0.006″), for a $1778\ mm$ (70″) virtual disk. The results for the diameter measurements are quite a bit different in magnitude compared to the form error results. There are several factors that can contribute to the diameter measurements errors. One error noticed, it that the measuring instrument body, when laid on top of a surface plate, measured with a height measuring instrument, produced an approximate bow shape, of $1.02\ mm$ (0.040″). This is likely due to the residual stresses in the raw material. The bow in the body causes the arm axes of rotation to not be parallel and the arms to move out of plane, which contributes error to the diameter and form measurements.

The uncertainty budget in the form error and diameter measuring process shows the typical error sources, with accompanying results. An expanded uncertainty of $0.024\ mm$ ($0.00094''$) is determined for the $508\ mm$ ($20''$) diameter measurement process of the measuring instrument and an expanded uncertainty of $0.004\ mm$ ($0.000016''$) is determined for the form error measurement process of the measuring instrument. There is an expanded uncertainty of $0.122\ mm$ ($0.0048''$) is determined for the $1778\ mm$ ($70''$) diameter measurement process of the measuring instrument. There is no form error uncertainty analysis for a $1778\ mm$ ($70''$) because of lack of setup for data collection. The percent contributions, relative to the expanded uncertainty, for each measuring process is also shown with the biggest contributions of error and thus can be considered for investigating corrective measures.

Though lacking the intended accuracy in the results, the measuring instrument is still able to measure relatively good, thus proving the concept of measuring both form error and diameter simultaneously.

7.2. Future Work

With the measuring instrument body having a bow in it, a new body is needed to get better accuracy out of the measured results. The bow compounds the error in the misalignment by affecting the out of plane motion if the arms, which can lead to errors in related to the z direction of the measuring instrument coordinate system.

The results can also be helped by implementing an adjustable mount, for alignment purposes. This mount can adjust the measuring instrument to be more true to the component axis, thus minimizing the alignment errors in mounting.

The springs in the arms can be replaced with a magnetic base principle. The spring force works for the current design, but can be inconvenient to use in a factory setting. To adapt a magnetic base, the measuring instrument would need to be made of aluminum and special containment, with a steel sphere on the end to contact the surface of the component, where a magnet can be "switched" on, to make magnetic contact with the component under-test via the contact sphere. A drawback is it can only be used on magnetic material, so aluminum is not an option to measure, but the intended purpose of this measuring instrument is for a manufacturing plant to use it on steel generator rotors, so the magnetic base principle would be applicable.

The last change would be to implement an "identification" routine for the kinematic parameter identification. Since the kinematic parameters are measured on a CMM, the kinematic parameters are effected by the controlled environment of the laboratory. Since the measurements in this research are taken in an environment close to that where the kinematic parameters were measured, the results were not affected significantly. If the measuring instrument is out in a higher temperature environment, the measuring instrument would expand and the kinematic parameters would have to be corrected for the difference. With the identification process, the measuring instrument could be tuned to the current environment and produce a more accurate results to that environment.

REFERENCES

[1]   E. R. Marsh, Precision spindle metrology, DEStech Publications, 2010.

[2]   G. Y. Zhang, X. P. Xu, X. H. Fu, L. Yang and C. Z. Li, "The measurement and control of diameter and in large-scale part processing," Journal of Material Processing Technology, vol. 129, pp. 653-657, 2002.

[3]   W. T. Estler, C. J. Evans and L. Z. Shao, "Uncertainty estimation for multiposition form error metrology," Precision Engineering, vol. 21, pp. 72-82, 1997.

[4]   S. Cappa, D. Reynaerts and F. Al-Bender, "A sub-nanometre spindle error motion separartion technique," Precision Engineering, vol. 38, no. 3, pp. 458-471, 2014.

[5]   E. Marsh, B. Knapp and D. Arneson, "Uncertainty sources in Multi-probe error separation," in ASPE, Boston, 2014.

[6]   D. J. Whitehouse, Handbook on Surface Metrology, London: Institute of Physics, 1994.

[7]   D. Whitehouse, "Some theoretical aspects of error separation techniques in surface metrology," Journal of Physics E: Scientific Instruments, vol. 9, p. 531, 1976.

[8]   M. J. Jansen, P. J. Schellekens and B. De Veer, Advanced spindle runout-roundness separation method.

[9]   D. Moore, "Design considerations in multiprobe roundness measurement," Journal of Physics E: Scientific Instruments, vol. 22, pp. 339-343, 1989.

[10]   K. Fujimaki, H. Sase and K. Mitsui, "Effects of sensor noise in digital signal processing of the three-point method," Measurement Science Technology, vol. 19, 2008.

[11]   E. Okuyama, N. Nosaki and J. Aoki, "Radial motion measurements of high-revolution spindle motor," Measurement, vol. 40, pp. 64-74, 2007.

[12]   C. H. Raifaizen, "A simpler proof of Heron's formula," Mathematics Magazine, 1971.

[13]   J. S. Beggs, Kinematics, Taylor & Francis, 1983.

[14]   A. Z540.2-1997, *Guide to the Expression of Uncertainty in Measurement*, 1997.

[15]   S. M. Yang, E. H. Fung and W. M. Chiu, "Uncertainty analysis of on-machince motion and profile measurement with sensor reading errors," Measurement Science and Technology, vol. 13, pp. 1937-1945, 2002.

[16]   M. Cox and A. Lazzari, "Modeling and uncertainty for high-accuracy roundness measurement," in 10th IMEKO TC7 International Symposium, Saint-Petersburg, Russia, 2004.

[17]   J. F. Tu, B. Bossmanns and S. C. Hung, "Modeling and error analysis for assesing spindle radial error motions," Precision Engineering, vol. 21, pp. 90-101, 1997.

[18]   B89.3.4M, Axes of Rotation: Method for Specifying and Testing, ANSI/ASME, 2010.

[19]   R. D. Grejda, "Use and calibration of ultraprecision axes of rotation with nanometer level metrology," 2002.

[20]   C. J. Evans, R. J. Hocken and W. T. Estler, "Self-calibration: reversal, redundancy, error separation, and 'absolute testing'," CIRP Annals-Manufacturing Technology, vol. 45, pp. 617-634, 1996.

[21]   R. Donaldson, "Simple method for separating spindle error from test ball roundness error," 1972.

[22]   G. X. Zhang, Y. H. Zhang, S. M. Yang and Z. Li, A multipoint method for spindle error motion measurement, 1997.

[23]   A. Visssiere, H. Nouira, M. Damak, O. Gibaru and J.-M. David, "A newly conceived cylinder measuring machine and methods that eliminate the spindel errors," Measurement Science and Technology, vol. 23, 2012.

[24]   J. F. Tu, M. Corless, M. J. Gehrich and A. J. Shih, "Experimental study of a precision, hydrodynamic wheel spindle for submicron cylindrical grinding," Precision Engineering, vol. 22, pp. 43-57, 1998.

[25]   J. Tlusty, Manufacturing processes and equipment, Upper Saddle River, NJ: Prentice Hall, 2000.

[26]   R. Thalmann, "Basics of highest accuracy roundness measurements," in Metrology Symposium, Spain, 2006.
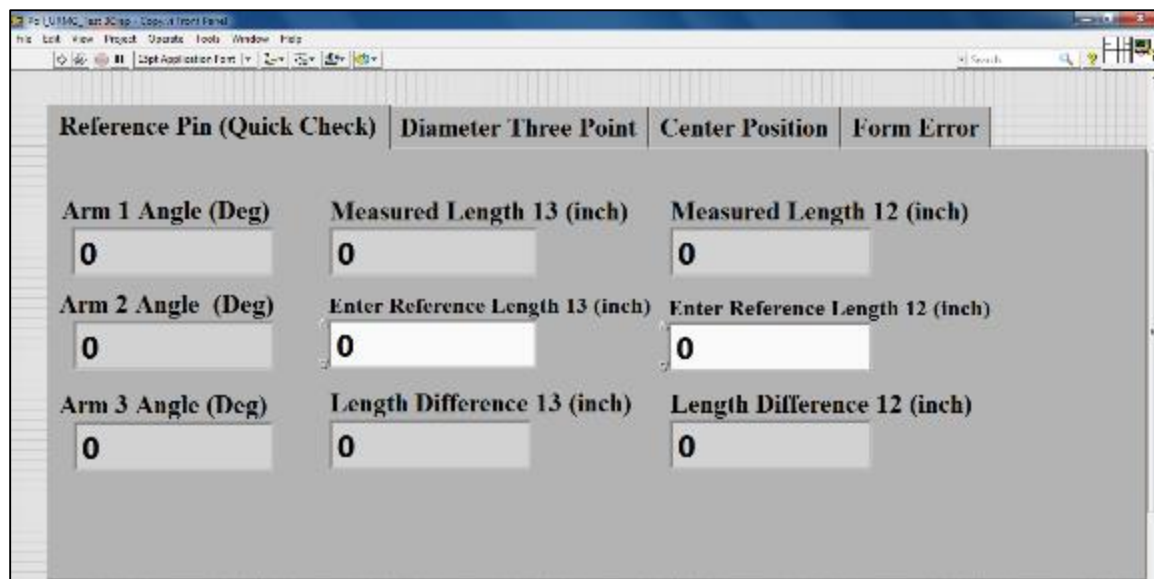
[27]   M. Solaguren-Besacoa Fernandez, J. M. Alegre Calderon and P. M. Bravo Diez, "Implementation in MATLAB of the adaptive Monte Carlo method for the evaluation of measurment uncertainties," Accred Qual Assur, no. 14, pp. 95-106, 2009.

[28]   M. Shiraishi, "Scope of in-process measurement, monitoring and control techniques in machining processes Part 2: In-process techniques for workpieces," Precision Engineering, vol. 11, no. 1, pp. 27-37, 1989.

[29]   T. Sheridan, "Know your machine tool," Lion Precision, 1991.

[30]   M. Neugebauer, "Uncertainty analysis for roundness measurements by the example of measurements on a glass hemisphere," Measurement Science and Technology, vol. 12, pp. 68-76, 2001.

[31]   B. Muralikrishnan and J. Raja, Computational surface and roundness metrology, Springer, 2009.

[32]   B. Muralikrishnan, S. Venkatachalam, J. Raja and M. Malburg, "A note on the three-point method for roundness measurement," Precision Engineering , vol. 29, pp. 257-260, 2005.

[33]   E. Marsh, R. Grejda, " Experiences with master axis method for measuring spindle error mtoions", Precision Engineering, vol. 24, iss. 1, pp. 50-57, 2000.

[34]   E. Marsh, R. Vallance, K. Hii and R. Grejda "Error motion of a kinematic spindle", Precision Engineering, vol. 28, iss. 1, pp. 204-217, 2004.

[35]   E. Marsh, J. Couey and R. Vallance, "Nanometer-Level Comparison of Three Spindle Error Motion Separation Techniques", Journal of Manufacturing Science and Engineering, vol. 128, iss. 1, 2005

[36]   E. R. Marsh, D. A. Arneson and D. L. Martin, A comparison of reversal and multiprobe error separation, 2008.

[37]   X. Lu and A. Jamalian, "A new method for charaterizing axis of rotation radial error motion: Part 1. Two-dimensional radial error motion theory," Precision Engineering, vol. 35, pp. 73-94, 2011.

[38]   X. Lu, A. Jamalian and R. Graetz, "A new method for characterizing axis of rotation radial error motion: Part 2. Experimental results," Precision Engineering, vol. 35, pp. 95-107, 2011.

[39]   K. Lau, R. Hocken and W. Haight, "Automatic laser tracking system for robot metrology," Precision Engineering, vol. 8, pp. 3-8, 1986.

[40]   K. Lau and R. Hocken, "A survey of current robot metrology methods," CIRP Annuals, vol. 32, no. 2, pp. 485-488, 1984.

[41]   L. Kirkup, Calculating and Expressing Uncertainty in Measurement, Sydney, 2007.

[42]   C. W. Kennedy, E. G. Hoffman and S. D. Bond, Inspection and Gaging, New York: Industrial Press Inc., 1987.

[43]   H. Jie, C. Huaiyan and C. Yun, "Uncertainty Evaluation Using Monte Carlo Method with MATLAB," Tenth Internation Conference on Electronic Measurement & Instruments, 2011.

[44]   JCGM, Evaluation of Measurment Data Supplement 1 to the " *Guide to the expression of uncertainty in measurements*" - Propogation of distributions using a Monte Carlo Method, JCGM, 2008.

[45]   JCGM, Evaluation of Measurement data Supplement 2 to the " Guide to the expression of uncertainty in measurements" - Extension to any number of quantities, JCGM, 2011.

[46]   P. R. Guimaraes Couto, J. Carreteiro Damasceno and S. Pinheiro de Oliveira, "Monte Carlo Simulations Applied to Uncertainty in Measurement," Brazil, INTECH, 2013, pp. 27-51.

[47]   R. D. Grejda, E. Marsh and R. Vallance, "Techniques for calibrating spindles with nanometer error motion", Precision Engineering, vol. 29, pp. 113-123, 2005.

[48]   W. Gao and S. Kiyono, "On-machine roundness measurement of cylindrical workpiece by the combined three-point method," Measurement, vol. 21, no. 4, pp. 147-156, 1997.

[49]   W. Gao, S. Kiyono and T. Sugawara, "High-accuracy roundness measurement by a new error separation method," Precision Engieering, vol. 21, pp. 123-133, 1997.

[50]   W. Gao, S. Kiyono and T. Nomura, "A new multiprobe method of roundness measurements," Precision Engineering , vol. 19, pp. 37-45, 1996.

[51]   K. C. Fan and Y. H. Chao, "In-process dimensional control of the workpiece during turning," Precision Engineering, vol. 13, no. 1, pp. 27-32, 1991.

[52]   W. T. Estler, K. L. Edmundson, G. N. Peggs and D. H. Parker, "Large-Scale Metrology - An Update," 2002.

[53]   R. R. Donaldson and S. R. Patterson, Design and construction of a Large, Vertical Axis Diamond Turning Machnine, LLNL Preprint - UCRL 89738, 1983.

[54]   D. Devit, "Axis of metrology," 2009.

[55]   D. G. Chetwynd and G. J. Siddall, "Improving the accuracy of roundness measurement," Journal of Physics E: Scientific Instruments, vol. 9, pp. 537-544, 1976.

[56]   H. Castrup, "Error Distribution Variances and Other Statistics," Integrated Science Group, 2009.

[57]   J. Bryan, R. Clouser and E. Holland, "Spindle accuracy," American Machinist, vol. 111, no. 25, pp. 149-164, 1964.

[58]   A. B89.3.4M, Axes of Rotation: Method for Specifying and Testing, ANSI/ASME, 1985.

[59]   A. B89.3.1 [1], Measurement of Out-of-Roundness, ANSI, 1972.

[60]   T. M. Adams, G104 - A2LA Guide for Estimation of Measurement Uncertainty in Testing, 2002.

[61]   International Vocabulary of Metrology - Basic and general concepts and associated terms, 3rd ed., 2012.

[62]   Measurement Uncertainty Analysis Principles and Methods – NASA Measurement Quality Assurance Handbook – ANNEX 3, NASA, 2010

[63]   A. Weckenmann, M. Knauer, T. Killmaier, " Uncertainty of coordinate measurements on sheet-metal parts in the automotive industry", Journal of Material Processing Technology, vol. 115, pp. 9-13, 2001

[64]   www.heidenhain.com

[65]   L. Valdez, J. Ziegert, P. Schmidt, "Uncertainty of In-process Roundness Measurement using the Multi-probe Error Separation Method", American Society for Precision Engineering, Austin, TX, 2015

[66]   R. Hocken, P. Pereira, Coordinate Measuring Machines and Systems, CRC Press, Taylor & Francis Group, 2012

[67]   B89.6.2, Temperature and Humidity Environment for Dimensional Measurement, ANSI/ASME, 1973.

APPENDIX A: LABVIEW PROGRAM

FIGURE 91: LabVIEW program for measuring instrument

APPENDIX B: SPINDLE ERROR MOTIONS

The spindle error motions of each measurement, from each component, is shown in the following figures. FIGURE 92 shows the spindle error motions for measurements one and two, from the aluminum plate component.
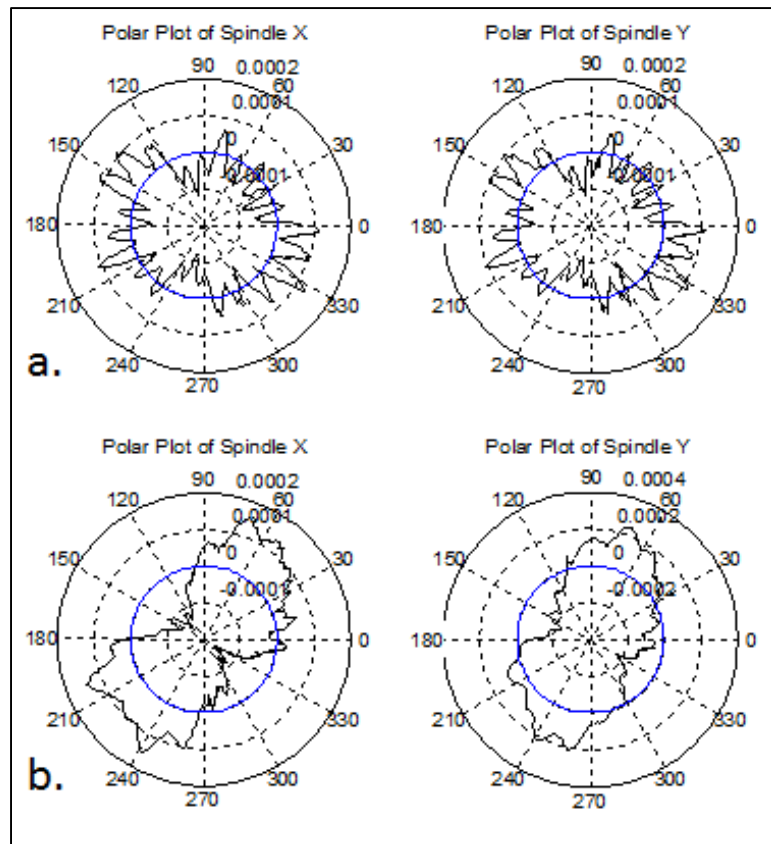

FIGURE 92: Spindle error motions for aluminum plate, a.) measurement one and b.) measurement two

FIGURE 93 shows the spindle error motions for measurements one and two, from the aluminum ring component.
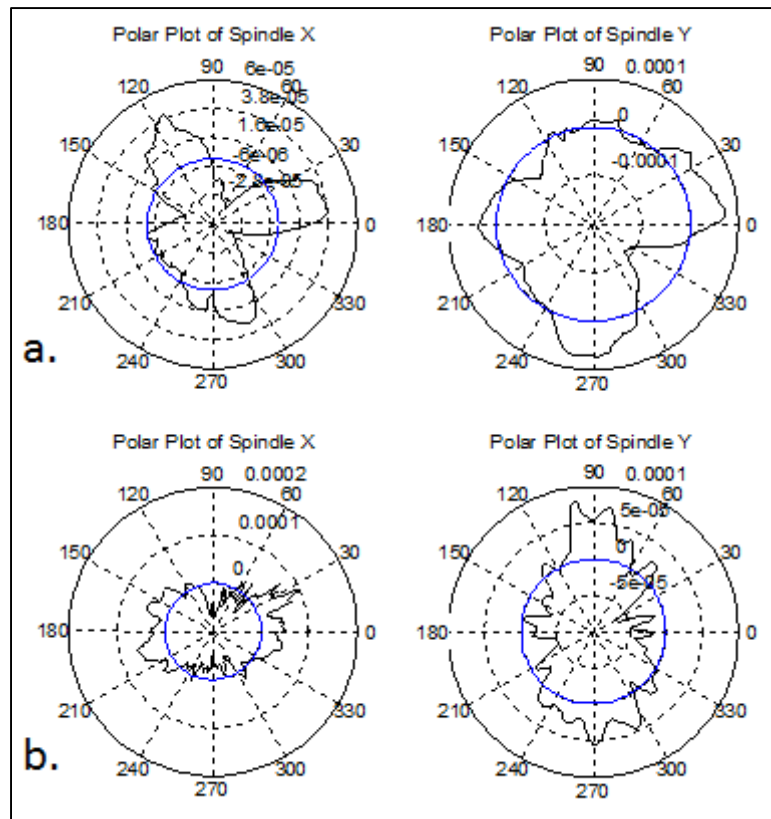

FIGURE 93: Spindle error motions for aluminum ring, a.) measurement one and b.) measurement two

FIGURE 94 shows the spindle error motions for measurements one and two, from the aluminum stock component.
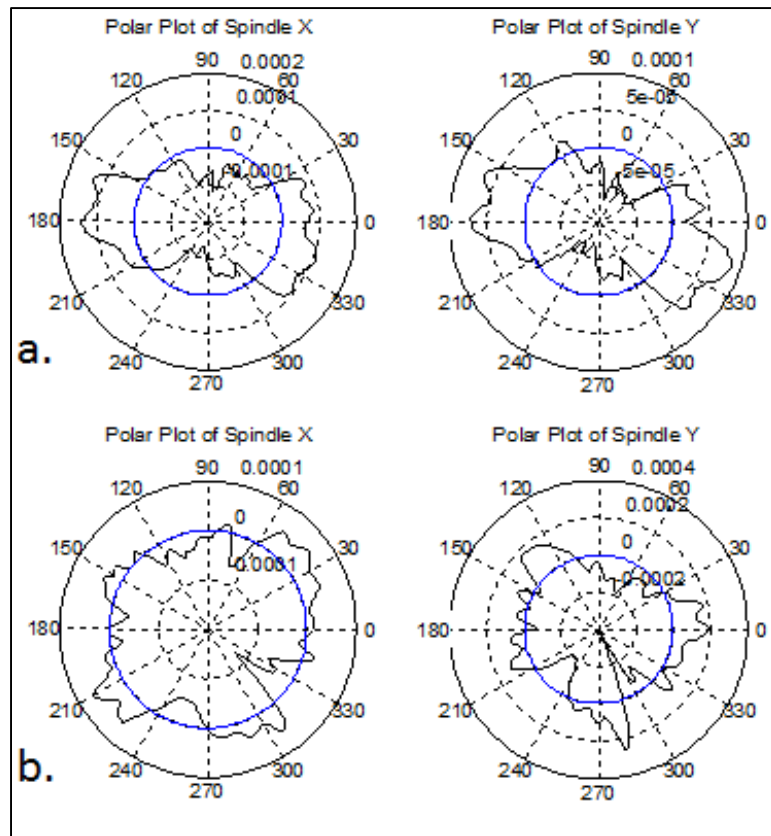

FIGURE 94: Spindle error motions for aluminum stock, a.) measurement one and b.) measurement two

The spindle used in testing is a synchronous, two RPM, motorized spindle. This spindle is not a high-precision spindle, thus the error motion are not very repeatable. It was used for the sole purpose of rotating the components under test, to measure the form error of the components. These spindle error motions are presented for completion of the axis of rotation testing, via the multi-probe error separation method.

Scalar values for the spindle error motions were determined using the Minimum Radial Separation (MRS) method (*ASME/B89.3.4* [18]). The spindle error motion peak-to-valley scalar values are presented for each component. TABLE 30 shows the spindle error motions for the aluminum plate, for each measurement.

TABLE 30: Peak-to-valley spindle error motions, aluminum plate a.) measurement one, and b.) measurement two

a.

UNCC	Max Value	Min Value	Peak-to-Valley
Y Comp (INST)	0.00013"	-0.00012"	0.00025"
	0.0033mm	-0.0030mm	0.0063mm
X Comp (INST)	0.00012"	-0.00012"	0.00024"
	0.0030mm	-0.0030mm	0.0060mm

b.

UNCC	Max Value	Min Value	Peak-to-Valley
Y Comp (INST)	0.00024"	-0.00024"	0.00048"
	0.0058mm	-0.0058mm	0.0120mm
X Comp (INST)	0.00016"	-0.00017"	0.00033"
	0.0041mm	-0.0043mm	0.0084mm

TABLE 31 shows the spindle error motions for the aluminum ring, for each measurement.

TABLE 31: Peak-to-valley spindle error motions, aluminum ring a.) measurement one, and b.) measurement two

a.

UNCC	Max Value	Min Value	Peak-to-Valley
Y Comp (INST)	0.00019"	-0.00012"	0.00031"
	0.0048mm	-0.0030mm	0.0078mm
X Comp (INST)	0.00005"	-0.00004"	0.00009"
	0.00013mm	-0.0010mm	0.0023mm

b.

UNCC	Max Value	Min Value	Peak-to-Valley
Y Comp (INST)	0.00009"	-0.00007"	0.00016"
	0.0023mm	-0.0018mm	0.0041mm
X Comp (INST)	0.00011"	-0.00007"	0.00018"
	0.0028mm	-0.0018mm	0.0046mm

TABLE 32 shows the spindle error motions for the aluminum stock, for each measurement.

TABLE 32: Peak-to-valley spindle error motions, aluminum stock a.) measurement one, and b.) measurement two

a.

UNCC	Max Value	Min Value	Peak-to-Valley
Y Comp (INST)	0.00009"	-0.00007"	0.00016"
	0.0023mm	-0.0018mm	0.0041mm
X Comp (INST)	0.00014"	-0.00013"	0.00027"
	0.0036mm	-0.0033mm	0.0069mm

b.

UNCC	Max Value	Min Value	Peak-to-Valley
Y Comp (INST)	0.00027"	-0.00039"	0.00066"
	0.0069mm	-0.0099mm	0.0168mm
X Comp (INST)	0.00007"	-0.00013"	0.00020"
	0.0018mm	-0.0033mm	0.0051mm